



The University of
Nottingham

University of Nottingham

Faculty of Engineering

Power Electronics, Machines and Control Group

**Novel Sizing and Modeling Techniques for
Synchronous Reluctance Machines.**

Mukhammed Murataliyev, B. Sc, M. Sc.

Thesis submitted to the University of Nottingham Ningbo Campus for the
degree of Doctor of Philosophy

December 2020

Acknowledgments:

Undertaking this PhD has been a challenging life-changing experience for me and it would not have been possible to do without the support and guidance that I received from many people.

I would like to thank my supervisors Prof. Michele Degano and Prof. Michael Galea for their consistent support and guidance during the running of this PhD project. I'm also very grateful to my PhD committee, Prof. Chris Gerada, Prof. Giampaolo Buticchi, Prof. He Zhang for their helpful research advices and suggestions.

I would also like to acknowledge my colleagues and friends in Ningbo and Nottingham for their wonderful collaboration. They supported me greatly and were always willing to help me.

In addition, I would like to thank my family for their support and wise counsel. They were always there for me.

Preface:

In recent years, there is a growing interest for high efficiency electric motors without, or with reduce content of, permanent magnets (PMs) for industrial applications. The Synchronous Reluctance (SynRel) machine is one of the most promising candidates that can meet the requirements of efficient and low cost drive [1]. The key benefits of this technology are a rotor structure made of flux barriers and iron parts, without excitation coils or PMs, like in induction motors (IM) and PM machines, respectively [2]. This leads to a cost effective structure that is using the reluctance principle to generate torque.

The reluctance machine topology was introduced in 1920s, however has not been utilised at high industrial volumes yet due to superiority of the alternative technologies. IMs are considered as an industry “work horse”, which dominates the electrical machines market in applications such as industrial fans, pumps and mill type loads, as it is known to be the cheapest and the most reliable machine topology. On the other hand, PMs are mostly used in high performance applications, where the power-density is of the priority. Whereas, the interest in SynRel is mainly driven by lack of magnets or any other field excitation, as well as high efficiency [3], [4], [5].

The rare-earth permanent magnets began to commercialize for electrical motors in early 1980s. Various types of applications such as electric vehicles, wind turbines, actuators, started utilization of the PM synchronous machines [6], [7], [8]. Neodymium-iron-boron (NdFeB) permanent magnets are the common type for the high-performance applications due to their superior magnetic properties. In comparison the remanent flux density B_r and coercivity H_c values of NdFeB are higher than any other type of magnets i.e. samarium-cobalt (SM_2Co_{17}), which was the major breakthrough in 1970s [9], and it is still extensively used when operating temperatures are very high.

The main downfall of the NdFeB is the cost. The prices of the Neodymium had a huge spike in the mid-2011, as it was increased by factor of 25 compared to the beginning of 2010 [10], [11]. After hitting its peak, the price dropped rapidly and settled at its pre-bubble price [12]. Such price instability had a huge financial effect on PM machine manufacturers. Hence, as of 2019, there is a high research

emphasis on electrical machines with low volume of rare earth permanent magnet material [13], [14].

There is also a growing interest in very high efficiency, or *super-premium efficiency* electrical machines for the industrial sector [2], [15], [16]. This is driven by new requirements of the local governments for the industrial sector, as well as the world trend towards the reduction of the energy consumption and greenhouse gas emissions [17], [18].

Currently world leading manufacturers and R&D institutions are constantly investigating the possibility of increasing the efficiency using inexpensive solutions. SynRel is a promising technology, which has features that are aligned with both research streams – high efficiency as well as lack of magnets [10], [12]. Leading manufacturing companies such as ABB (“Asea Brown Boveri”), KSB (“Klein, Schanzlin & Becker”) and Siemens already started the serial production of the high efficiency SynRel.

However, despite its advantages, there are still number of problems that are being investigated. From the machine design perspective, the main challenges of the topology come from the complex anisotropic structure of the rotor. Torque ripple, power factor and other secondary effects such as rotor iron losses, vibration and noise, are the main issues in SynRel [19], [20]. These issues mainly addressed using comprehensive analysis and optimization using FE.

The proposed ideas and innovative techniques that are described in this thesis could significantly reduce time and effort required to design the SynRel machines. In some cases, it was shown that the time-consuming design optimization by means of FE can be bypassed. This is achieved by applying new dimensioning techniques, hence leading to a quick and effective design tools that is applicable for the wide power range machines.

Thesis contains 8 chapters that summarize the research activities that were carried out during 3-year Ph.D. period.

Chapter 1 is the introduction covering the efficiency trend as well as the problems with the permanent magnet materials supply. The potential of the SynRel as a modern industrial drive is discussed.

Chapter 2 describes the common preliminary sizing technique that provides the fundamental basic equations that are used in the common machine design process.

Chapter 3 presents a simple analytical model that later can be used for the sizing of the Synchronous Reluctance (SynRel) machines. The accuracy of the method is

achieved by modelling a simple rotor geometry that presents all the characteristics of a real machine. The analytical equations proposed are able to guarantee accurate and fast results during the preliminary design of the machine.

Chapter 4 presents a SynRel sizing method based on the derived analytical model. The accuracy of the proposed model is validated, for a range of operating conditions, comparing the results with both finite element simulations and experimental measurement carried out from an existing four poles SynRel 15kW prototype.

Chapter 5 This chapter focuses on the detailed analytical evaluation of the magnetic behaviour of the scaled SynRel machines. The analytical model defined previously has been applied to a wide range of machines and validated through finite element analysis. Three reference machine geometries are defined, labelled as M1, M2 and M3, based on existing designs. These have different combinations of stator and rotor geometrical parameters.

Chapter 6 In this chapter the analytically calculated data, the rated torque as function of size and volume are derived using the regression analysis, which is a set of statistical processes for estimating the relationship between variables.

Chapter 7 Following up on the scaling principle for SynRel that was introduced in previous chapters. This chapter presents a novel design concept for Synchronous Reluctance (SynRel) machines aimed at reducing the torque ripple. Two general sizing approaches based on the homothetic scaling principle are defined and compared. An in depth analysis on the torque ripple, for a wide range of scaled geometries, evaluated by finite element, has been carried out at different operating conditions.

Chapter 8 The theory that was proposed in the previous chapter is validated experimentally. The torque ripple of the scaled machines, computed by means of FE simulations is compared against the experimental measurements on the reference machine prototype for different operating conditions.

Scientific Contribution:

Several parts of this thesis have been presented in journals by the author during his Ph.D. program. Hereafter the publications are listed:

1. M. Murataliyev, M. Degano, and M. Galea, "A Novel Sizing Approach for Synchronous Reluctance Machines," *IEEE Trans. Ind. Electron.*, vol. 0046, no. 2, 2020.
2. M. Murataliyev, M. Degano, M. Di Nardo, D. Prystupa, S. Wang, G. Buticchi, H. Zhang, C. Gerada and M. Galea, "A Homothetic Scaling Criteria for Synchronous Reluctance Machines Design". *IEEE Transactions on Energy Conversion*. 2020.
3. M. Murataliyev, M. Degano, M. Di Nardo, N. Bianchi, A. Tassarolo, W. Jara, M. Galea and C. Gerada, "Design in Synchronous Reluctance Machines and Effects on Torque Ripple". *IEEE Transactions on Energy Conversion*. 2020.
4. M. Degano, M. Murataliyev, S. Wang, D. Barater, G. Buticchi, W. Jara, N. Bianchi, M. Galea, C. Gerada, "Optimised Design of Permanent Magnet Assisted Synchronous Reluctance Machines for Household Appliances". *IEEE Transactions on Energy Conversion*. 2020. (In press)

Contents

Acknowledgments:.....	2
Preface:	3
Scientific Contribution:	6
List of Figures:.....	10
List of Tables:.....	14
Nomenclature:.....	15
List of Abbreviations:.....	18
1. Chapter 1: Introduction.....	20
1.1 Legislations towards high efficiency:	20
1.2 Problem with Permanent Magnet Materials:.....	24
1.3 SynRel’s potential as a Modern Industrial EM:.....	26
1.4 SynRel’s complex design problem:	29
2. Chapter 2: Theory of the Synchronous Machines	32
2.1 Synchronous machines classification:.....	32
2.2 Torque performance comparison:	36
2.3 Classical sizing approach:	38
3. Chapter 3: Analytical model for SynRel sizing.....	43
3.1 Introduction:.....	43
3.2 Analytical Derivation:	43
3.2.1 d - q parameters approximation:	45
3.2.2 Linear sizing:.....	46
3.3 Air Gap Function Approach for Saliency Derivation:.....	48
3.3.1 Anisotropic rotor geometry considerations:	49
3.3.2 Air gap function for d-axis excitation:.....	51
3.3.3 Air gap function for q-axis excitation:.....	52
3.3.4 Stator slotting considerations:	55

3.3.1	Magnetizing coefficients and saliency ratio:	56
3.4	Saliency ratio considering saturation:.....	60
3.4.1	Simplified magnetic circuit:	60
3.4.2	The principle of saturation modelling:.....	64
3.4.1	Saturation factors:.....	66
3.5	Preliminary model validation by means of FE:.....	69
3.6	Conclusion:	71
4.	Chapter 4: SynRel Sizing Method.....	72
4.1	SynRel sizing approach:.....	72
4.2	FE Case Study:.....	74
4.2.1	Inductance validation with respect to FEA results:	75
4.2.2	Torque validation with respect to FEA results:	76
4.2.3	Sizing method validation with respect to FEA results:	77
4.3	Experimental validation of the Sizing approach:.....	78
4.4	Conclusion:	80
5.	Chapter 5: A Homothetic Scaling Criteria for Synchronous Reluctance Machines Design	81
5.1	Introduction:.....	81
5.2	Reference machines:	82
5.3	Radial scaling assumptions:.....	84
5.4	Effect of scaling on magnetizing coefficients:.....	84
5.5	Effect of scaling on saturation:.....	85
5.6	Effect of MTPA for the M2 scaled geometries:	88
5.7	FE evaluation:.....	90
5.8	Conclusion:	91
6.	Chapter 6: A Generalized scaling derivation.....	92
6.1	Introduction:.....	92
6.2	Radial scaling function:.....	92

6.3	Main sizing function:.....	94
6.4	General Torque as function of α^e :.....	95
6.5	ISO torque curves:	97
6.6	Case studies and experimental validation:	97
6.7	Conclusion:	100
7.	Chapter 7: Homothetic Design in Synchronous Reluctance Machines and Effects on Torque Ripple.....	101
7.1	Introduction:.....	101
7.2	Scaling principle and reference machine design:.....	102
7.3	Rotor design of the reference machine:	104
7.4	Scaling principle:.....	104
7.5	Evaluation of the Scaled machines torque performance:.....	105
7.5.1	FE evaluation of M1, M2 and M3 geometries:	106
7.5.1	FE evaluation of wide range of scaled geometries:	109
7.6	Torque ripple optimization:	109
7.7	Mechanical considerations:	112
8.	Chapter 8: Experimental validation of the torque ripple:.....	117
8.1	Introduction:.....	117
8.2	FE torque ripple analysis for scaled machines:	117
8.3	Experimental results and validation:.....	119
8.4	Conclusion:	122
9.	Chapter 9: Conclusion and Future Works.....	124
10.	References.....	125

List of Figures:

Figure 1.1. EM Efficiency movement timeline, standard 15kW motor example. [24].	21
Figure 1.2. REE Oxides price trend. The data was retrieved from the USGS Mineral Commodities Summaries [37].	24
Figure 1.3. IM and SynRel efficiency based on ABB's data, 2014	27
Figure 1.4. Number of Publications on SynRel topic over the past decade	30
Figure 1.5. Rotor geometry and related microscopic and macroscopic parameters [67].	31
Figure 2.1. All possible combinations of reluctance and excitation torque components.	33
Figure 2.2. PM to reluctance machine topologies.	34
Figure 2.3. Iso torque curves with highlighted MTPA.	36
Figure 2.4. FE and common analytical sizing approach comparison.	41
Figure 2.5. SynRel geometries under test.	42
Figure 3.1. ALA and TLA SynRel topologies. [50], [53].	43
Figure 3.2. Salient pole rotor's field distribution.	44
Figure 3.3. Rotor slotting, magnetic flux using infinite slot approach.	48
Figure 3.4. Quarter of geometry for anisotropic type rotor (3 – barriers in this case), 4-pole configuration. Based on $\Delta\alpha_k$ (per unit value of α) and hc_k (per unit value of barrier thickness).	50
Figure 3.5. Sketch of d-axis (on the left) and q-axis (on the right) flux paths. The rotor barrier slotting effect is highlighted.	51
Figure 3.6. Idealized flux paths for q-axis excitation (tangentially flattened rotor), flux path through air barriers is highlighted with red.	53
Figure 3.7. Magnetic circuit for a 3 - barriers SynRel rotor, including barrier slotting effect. a) d-axis excitation b) q-axis excitation.	54
Figure 3.8. Stator slotting, magnetic flux using infinite slot approach, where slotted region is highlighted in blue.	55
Figure 3.9. Magnetic circuit considering stator slotting.	56

Figure 3.10. Magnetizing coefficient K_{dm} as a function of geometrical parameters: g is an air gap length, and R_{si} is the stator inner radius, both expressed in m	58
Figure 3.11. Magnetizing coefficient K_{qm} as a function of geometrical parameters: g is an air gap length, and R_{si} is the stator inner radius, both expressed in m	58
Figure 3.12. Unsaturated saliency ratio and neglected leakage ξ for various R_{si}/g combination	59
Figure 3.13. Magnetic circuit with the highlighted segments subject to saturation for d-axis.....	60
Figure 3.14. Simplified magnetic circuit of one pole.	61
Figure 3.15. Flow Chart of saturation modelling.	63
Figure 3.16. M530-65A iron B-H curve with highlighted points.	64
Figure 3.17. SynRel air gap flux density and MMF levels.	65
Figure 3.18. Stator back iron flux density and magnetic field strength levels... ..	65
Figure 3.19. Stator tooth flux density and magnetic field strength levels.	66
Figure 3.20. Inverse saturation coefficients as functions of I_s and α^e . $K_{dm}=0.8$, $K_{qm}=0.03$	67
Figure 3.21. d - q inductances as functions of I_s and α^e , and k_{air}	68
Figure 3.22. SynRel pu Torque profiles on Id-Iq plane.	68
Figure 3.23. Average torque comparison, for a range of different rotor diameter: T_{re} – refined torque values using air gap function.	71
Figure 4.1 Flow chart of the analytical sizing method	73
Figure 4.2. Variation of inductance with the change of I_d . With 4 highlighted data points.	75
Figure 4.3. Variation of inductance with the change of I_q . With 4 highlighted data points.	76
Figure 4.4. FEA vs analytical torque current profiles.....	77
Figure 4.5. Test rig: 15kW SynRel motor (left hand side) and 40kW induction machine used as a load (right hand side).	78
Figure 4.6. Comparison of Torque values on Id-Iq plane.....	79
Figure 5.1. Homothety example	81
Figure 5.2. Sketch of stator geometrical parameters.....	82

Figure 5.3. Quarter of geometry for anisotropic type rotor with 3 – barriers and 4-pole configuration. Based on $\Delta\alpha k$ (per unit value of α) and h_{ck} (per unit value of barrier thickness).	83
Figure 5.4. Magnetizing coefficient K_{dm} and K_{qm} as a function of stator inner radius for M1, M2 and M3 geometries.	85
Figure 5.5. Analytical model outputs: air gap flux densities and fundamental magneto motive forces for M1, M2 and M3 based on the scaled magnetizing coefficients.....	87
Figure 5.6. M2 geometries p.u. values of torque on mmfd-mmfd plane. a) radially scaled, b) axially scaled.	89
Figure 5.7 Reference geometries FE simulated and analytically calculated p.u. torque on current excitation angle α^e and scaling factor S_{si} plane, a) M1 b) M2 c) M3.....	90
Figure 5.8. FE simulated M2 geometries. On the left $S_{si}=1.765$, and $S_{si}=2.36$ on the right with highlighted flux densities.....	91
Figure 6.1. M1, M2 and M3 sizing curves.	94
Figure 6.2. $T(R_{si}, \gamma)$ M2 example.	95
Figure 6.3. p.u Torque as a function of α^e at three different saturation levels..	96
Figure 6.4. Test rig: M21 SynRel motor (left hand side) and 40kW induction machine used as a load (right hand side).	98
Figure 6.5. Test rig: M22 SynRel motor (left hand side) and 160kW induction machine used as a load (right hand side).	98
Figure 6.6. General sizing at given rated current (MTPA $\alpha^e=60^\circ$).	99
Figure 6.7. Comparison of iso-torque values.....	100
Figure 7.1. A simplified sizing algorithm.	103
Figure 7.2. Sketch of optimized benchmark machine M1.....	104
Figure 7.3. Average torque and peak to peak torque on I_d and I_q planes for M1, M2 and M3 machines.	106
Figure 7.4. M1, M2 and M3 MTPA.....	107
Figure 7.5. Torque ripple vs peak phase current at MTPA.	107
Figure 7.6. $T_{\Delta}(I_s, S_{si})$. Torque ripple vs Peak phase current at MTPA.....	108
Figure 7.7. Optimization workflow.....	110

Figure 7.8. Optimization variables trend of M2*, M3*, M4*, M5*	111
Figure 7.9. FE stress maps of scaled rotor geometries at n=18000 rpm.....	114
Figure 7.10. Mechanical analysis of scaled geometries for AGS and AGF scaled geometries a) Maximum stress b) Maximum displacement c) Safety factor as functions of scaling factor S _{si} and rotational speed n in rpm	115
Figure 8.1. FE evaluation of the torque ripple at different current angles and different current loading: a) and b) scaled machines S _s = 0.75, (M4 vs M5); c) and d) scaled machines S _s = 1.5, (M2 vs M3).....	118
Figure 8.2. M1 SynRel prototype front view.....	119
Figure 8.3. Experimental test setup.....	120
Figure 8.4. Experimental and FE evaluation of the torque ripple on the reference machine M1: a) at 45° current angle for different current loading; b) at 50° current angle for different current loading.....	121

List of Tables:

Table 1.1. Comparison of PM prices and their properties [35].	25
Table 2.1. Sizing evaluation test.	41
Table 3.1. Slot opening parameters	57
Table 3.2. Rotor geometry considerations.....	58
Table 3.3. Highlighted B-H curve points of M530-65A iron.....	63
Table 3.4. Details of FEA validation.....	70
Table 4.1 Final parameters of tested 15kW SynRel.....	74
Table 4.2. Summary of FEA vs Analytical modelling.	77
Table 4.3. Rated Saliency ratio	78
Table 4.4. Highlighted data points, for different rated current angles.	79
Table 5.1. Reference machines' main dimensions	82
Table 5.2. Reference rotors dimensions	83
Table 5.3. Details of FE evaluation	89
Table 6.1. PWR coefficients for radial scaling.....	93
Table 6.2. PLR coefficients for $T(R_{si}, \gamma)$	95
Table 6.3. Curve fitting coefficients for general function of $T_{pu}(mmf_{pu}, \alpha^e)$	96
Table 6.4. Summary of two machines scaled from M2 geometry.....	97
Table 7.1. Design specifications, constrains and machine parameters.	103
Table 7.2. Scaled geometries.....	105
Table 7.3. Optimization input variables' boundaries.	109
Table 7.4. Summary of the optimal flux barrier angles.....	112
Table 7.5. Details of validation.....	113
Table 7.6. Details of FE mechanical simulations.	113
Table 8.1. Summary of the torque ripple evaluation.....	122

Nomenclature:

A	Linear current density
B_1	Fundamental component of the air gap flux density
B_{1d}	Fundamental component of the direct axis air gap flux density
B_{1q}	Fundamental component of the quadrature axis air gap flux density
B_d	Direct axis air gap flux density
B_q	Quadrature axis air gap flux density
B_{max}	Peak air gap flux density
C_u	Utilization Coefficient
D_{ro}	Rotor outer diameter
D_{si}	Stator inner diameter
E	Back EMF
F_d	Direct axis magneto motive force
F_q	Quadrature axis magneto motive force
g	Air gap
g^d	Direct axis effective air gap
g^q	Quadrature axis effective air gap
I_d	Direct axis current

I_q	Quadrature axis current
I_s	Peak phase current
k_{air}	Insulation ratio
K_{dm}	Direct axis magnetizing coefficient
K_{qm}	Quadrature axis magnetizing coefficient
K_s	Saturation coefficient
K_{w1}	Winding factor
K_{sd}	Direct axis saturation coefficient
K_{sq}	Quadrature axis saturation coefficient
L	Stack length
L_d	Direct axis inductance
L_q	Quadrature axis inductance
L_{dm}	Direct axis magnetizing inductance
L_{qm}	Quadrature axis magnetizing inductance
L_m	Magnetizing Inductance
m	Number of phases
n	Rotational speed
N_s	Number turns per phase
p	Number of pole pairs

P	Apparent power
Q	Number of stator slots
S_{si}	Stator scaling coefficient
S_{ro}	Rotor scaling coefficient
T_{em}	Electromagnetic torque
V_{br}	Bore volume
Z_Q	Number of conductors per slot
ξ	Saliency ratio
λ_s	Single phase flux linkage
γ	Aspect ratio
ϕ	Flux per pole
τ_s	Slot pitch
ω	Rotation speed in rad/s

List of Abbreviations:

Dy	Dysprosium
EM	Electrical machine
EMF	Electromotive force
IE4	Super-Premium efficiency
IE5	Ultra-Premium efficiency
IM	Induction machine
IPM	Interior permanent magnet machine
IPMSM	Interior permanent magnet synchronous machine
LV	Low voltage
MMF	Magnetomotive force
MV	Medium voltage
Nd	Neodymium
NdFeB	Neodymium magnet
Non-Re	Non-rare earth
PF	Power factor
PMaSynRel	Permanent magnet assisted synchronous reluctance machine
PMSM	Permanent magnet synchronous machine
PO	Policies options
REE	Rare earth element

SPM	Surface permanent magnet machine
SynRel	Synchronous reluctance machine
VSD	Variable speed drives

Chapter 1: Introduction

For the past few decades, replacement of the mechanical and hydraulic systems was one of the main motivations associated with the systems' electrification. A lot of effort was also put towards the replacement of the fixed speed and outdated electric drives with higher-performance variable drives. These are mainly driven by supremacy in reliability, efficiency and robustness of the modern electrical systems. A so called trend of "more electric" systems has affected a wide range of applications, including: aerospace, traction, actuation, mining, oil & gas. However, the growing interest in these application has raised a number of challenges for researches in the field, since the developed electrical systems should meet the strict demands and requirements of the application i.e. harsh working environment, high-power density, efficiency and fault tolerance. The development of the advanced electrical machines has a principal importance in any drive system's modern electrification.

The advancement in power electronics was the main impulse that enabled the fundamental change towards the Variable-Speed Drives (VSD). The classical conventional system has a generated/motor that is connected directly to the grid, hence operating at the grid frequency. Systems' prime-mover/load were usually designed to operate at certain operating speed. Mismatch in speed was traditionally solved by the gearbox. Key problem of such system is that gearbox bring reliability and maintenance challenges. Whereas VSD allows to bypass the gearbox by acting as "electronic gearbox". Therefore, modern VSD poses a number of advantages such as: improved power train solution in general, better control, reduced maintenance, reliability. These attracts a lot of attention in several engineering application fields.

1.1 Legislations towards high efficiency:

High efficiency electrical machines became integral part of future roadmaps in EU, US and in general worldwide. Two efficiency classes IE4 (Super-Premium Efficiency) and IE5 (Ultra-Premium Efficiency) are covering more and more application fields. The efficiency classes IE1 – IE4 are now recognised globally and are described in the international standard IEC 60034-30.

As it is reported in [21], [22] electrical machines consume approximately 40% of the total worldwide energy generated, whereas in EU this number reaches 70% of the total consumed energy. It is well known that the IM is the most common type of the electrical machine that has the largest market share, improvements in its energy efficiency could lead in a significant reduction in power consumption. To achieve the energy saving policies, biggest EM manufacturers tend to shift towards the VSD, i.e. in EU it is adopted by 30% of the newly installed machines [23].

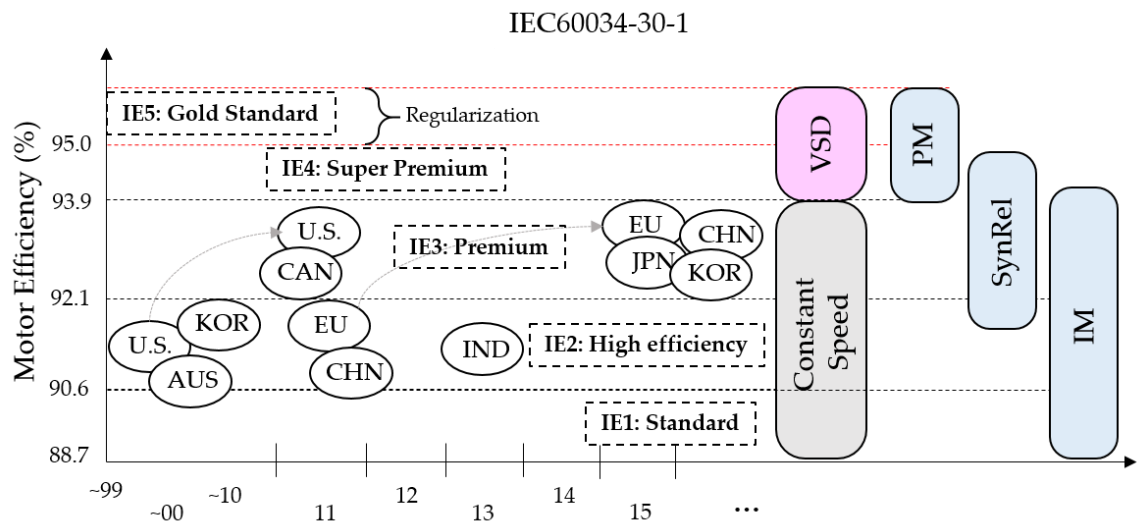


Figure 1.1. EM Efficiency movement timeline, standard 15kW motor example. [24].

The main EU energy and climate goal of the 2020 is to achieve the reduction in the greenhouse gas emission by 20% compared to the 1990 level [23], [25], by raising the share of the power generation from renewable resources. New regulations according to the 2030 Framework on Climate and Energy were set in 2014 by the European Commission on January 22nd and by European Council on October 24th. The next milestone was set for a mandatory 40% reduction in greenhouse gas emission from the 1990 level and 27% of the total generated power should come from the renewable sources, whereas the energy saving target of 27% has been achieved.

It was highlighted in [26], that the acceptance of the higher efficiency standards EMs is affected by the existence of the common standards of the motor performance tests, efficiency classification and labelling. The IE4 Standard was introduced in the 1st edition of the IEC 60034-30 standard, whereas the Gold Standard IE5 was introduced in the 2nd edition.

Figure 1.1 presents the motor efficiency classes timeline and the biggest manufacturers by countries that has accepted new legislations according to IEC 60034-30 Standard (15kW drive example). Figure 1.1 was retrieved from [24], however it was modified by adding SynRel efficiency capability based on [27], [28]. The main electrical machine topologies that are considered as the appropriate candidates for the particular efficiency standards are PM, IMs and SynRel as an alternative topology. The standards that are highlighted in Figure 1.1 are applicable for EMs that lies in the power range between 0.12kW and 800kW with the voltage up to 6kV, number of poles of considered machines are 2 – 8, whereas the thermal operating conditions are between -20°C up to 60°C at 4000m altitude [29]. Based on the efficiency trends and the capability of IMs and PM machine topologies, SynRel is able to find its niche with its Premium Efficiency.

The strong push towards high efficiency is dictated by the recent EU environmental policies. These are reported in [26], [30], [31]. The Eco-Design directive lifecycle summary - policies options (PO) are:

- PO-1 was accepted on 1st January 2018 and includes:
 - PO-1A - all Single Phase Motors that are rated above 0.12kW should meet the IE2 standard or greater
 - PO-1B - three phase motor that are rated power greater than 0.12kW and less than 0.75kW should meet the IE2 standard or greater
 - PO-1C – three phase Low Voltage (LV) and Medium Voltage (MV) motors that are rated above 375kW and below 1000kW should meet IE3 standard or greater
- PO-2 should be accepted by 1st January 2022 the VSD application motors rated above 0.75kW should meet IE3 standard
- PO-3 was accepted on 1st January and included the explosion proof and brake motors
- PO-4 was accepted on 1st January 2018 included mandatory requirements for motors and VSD (discussed later)
- PO-5 was accepted on 1st January 2018 – all VSDs to meet the IE1 performance at minimum energy performance standards (MEPS)
- PO-6 should be accepted by 1st January 2022 includes:
 - PO-6A- raising MEPS should be raised for medium IMs that are rated greater than 0.75kW and less than 375kW from IE3 to IE4
 - PO-6B – raising MEPS for larger IMs that are rated greater than 375kW and less than 1000kW from IE3 to IE4.

The PO1 was accepted due to the current global trend towards efficiency improvements of the medium and large size motors. The MV motors that operate at nominal voltage of 1kV – 6.6kV. These are produced for an individual site, and should comply with the IE3 standard. Speaking of the lower rated small motors, the regulations only apply for IMs (single phase or three phase). These machines are usually mechanically commuted and have a lower number of working hours in order to justify the regulation. Acceptance of PO2 all VSD are pushed to the usage of the IE3 standards motors. IE3 machines also usually have cheaper price compared to IE2 motors with the VSD circuits. Inclusion of the brake motors under efficiency regulations is justified as the frequent starts and stops will cause less losses. PO4 states that all machine's product information requirements as well as the comprehensive detailed technical information should be included on the rating plate for all motors that are rated 0.12kW – 1MW. The PO5 was introduced to eliminate the usage of the VSD motors that are below IE1 standard. PO-6 mainly focuses on the transition to IE4, that should be available at the competitive prices compared to IE3 machines.

According to [32], approximately 56% of all motors' that are in use worldwide are exceeding their duty cycle. 68% of the utilized motors are oversized having the load that is less by 60% or sometimes 80% of their rated capability. The old machines (fans, pumps, compressors) are inefficient and usually fall under IE0/IE1 standards. Moreover, they are less reliable and less performant and require constant maintenance and repair. One of the biggest worldwide industrial problems is the lack of the machine renewal culture [32].

Three phase Squirrel Cage IMs take a major sector of the EM market [12], [10]. Currently major manufacturers already have the capability to produce the SCIMs that meet the IE4 standard, having the standard frames with the aluminium rotor cages [33], [34]. Line start PM machine (LSPM) is an another IE4 class motor, usually it has the interior REE PMs (NdFeB) and auxiliary cage for starting. Reluctance motors that can be divided into two different types are the VSD controlled reluctance motors (VRSM) and Switched Reluctance motors (SRM) also present on the EM market. Both reluctance drive types are capable to meet the IE4 standard.

1.2 Problem with Permanent Magnet Materials:

PMs are an essential component of the electric motors and generators. Key properties of PMs are coercivity and the remanent magnetization. These are strongly dependant on the microstructure. One of the most widely used PMs for traction motors and power generators contain Neodymium (Nd) and Dysprosium (Dy). Dy is used to sustain the NdFeB PMs coercivity at higher temperatures [35]. Both Dy and Nd are considered as the rare earth elements (REE) and listed as the critical materials by US Department of Energy as well as the other international institutes due to the high risk in supply [36]. Other alternatives are the non-rare earth (non-RE) PMs have lower magnetic performance, however still attracts a lot of attention given the small risk in supply and cheap price.

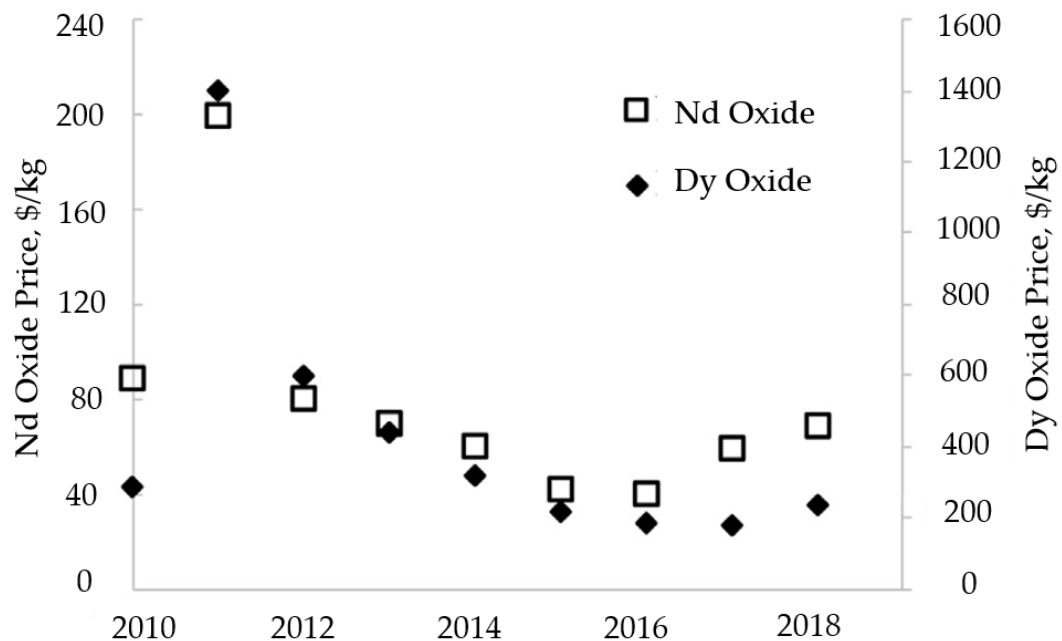


Figure 1.2. REE Oxides price trend. The data was retrieved from the USGS Mineral Commodities Summaries [37].

The demand for NdFeB PMs are dramatically increased as the world pursues the energy efficiency, renewable energy and electrification trend. Figure 1.2 presents the average price of Dy_2O_3 and Nd_2O_3 according to USGS Mineral Commodities Summaries. The average price of the Dy Oxide has spiked from 245\$/kg in 2010 to 1410\$/kg in 2011, then gradually went down to 185\$/kg in next 5 years. The prices of the Nd Oxyde also has raised from 88\$/kg in 2010 to 195\$/kg in 2011, and then went down to 39\$/kg in 5 years [37]. The increase in Nd Oxyde average price was mainly caused by huge increase in demand in REE as well as

the monopoly of the critical REE mines. There is an obvious divergence in the price of two oxides Figure 1.2 after 2016. This happened due to successful reduction of usage of the Dy element. China and biggest European countries are currently forcing the EVs to replace the internal combustion engines which are expected to be phased out in two decades. With the increase in number of EVs the Nd price will continue to grow.

Table 1.1. Comparison of PM prices and their properties [35].

	(BH) _{max} (MGOe)		H _{ci} (kOe)		Br (kG)		Price (\$/kg)	
	2016	2022	2016	2022	2016	2022	2016	2022
NdFeBDy (NH42SH)	40-42	42	20	20	13- 13.3	13	60\$	120\$
Sm-Co (SC- 3215)	31-32	34	15	15	11.2- 11.8	12	128\$	210\$
AlNiCo-9	9	11	1.4	2	10.5	10.5	71\$	80\$
Ferrite (Sr- 8B)	3.8	3.8	3	3	4	4	4\$	4\$

Based on the market report that was presented in [38], in 2015 the sale of NdFeB, SmCo, Ferrite and Alnico are 2927M\$, 722M\$, 4344M\$ and 355M\$ respectively. According to the PM sales report Ferrite is dominant by occupying nearly half of the market. Ferrite PMs are very popular solution for motors that do not require high power density. However, for those application that are limited in size and weight i.e. aerospace application or EVs, REE magnets are the only viable choice. The most pragmatic approach to reduce the usage of REE is development non-RE magnets that can fill the magnetic performance gap between Ferrite and REE magnets. Table 1.1 presents the prices and properties of the various PMs in 2016 as well as the predicted values in 2022. The table presents the cost properties ratios \$/kg/kG/kOe where the magnet cost per kg \$/kg is divided by the remanent magnetization kG and the coercivity kOe. It is desired to develop non-RE magnets that will have higher value of cost property ratio (\$/kg/kG/kOe).

The strategies to address the REE problem are increasing and diversifying the supply sources and reducing the demand. China, Australia, US, Vietnam have started to open new REE mines including the desired Dy. However, none of the newly opened mines can compete with the existing mines that are rich in REE deposits that are mostly in China. To reduce the demand in REE, non-RE or less-

RE PM technology are being investigated. Significant advancement in reducing Dy content in NdFeB, while still keeping required coercivity, was achieved by reduction of the grain size of the PM [39]. The development of the EM technologies that does not require the PMs excitation is one of the key approaches to the described problem. And SynRel is considered as one of the most promising candidates.

1.3 SynRel's potential as a Modern Industrial EM:

Adoption of SynRel technology requires a comprehensive comparison with the IM and PM machines as well as the pros and cons of such adoption.

The SynRel can be derived from the standard IM simply by removing the rotor cage and introducing rotor's magnetic saliency (anisotropy). In [40] it was shown that approximately 80% of torque can be retained whereas the losses were reduced down to 60% of initial design by simply substituting the IM rotor with the SynRel's. Hence the SynRel was named as a *prima facie* - a direct competitor for a typical industrial application [41]. As the IM was serving as the *industry's workhorse* for over century it currently challenged by the high-efficiency SynRel. The following SynRel's advantages over IM can be highlighted as: [40], [41]

- + Synchronous operation – no slip, synchronous drive
- + No conductors in rotor
 - o Robustness
 - o Manufacturing cost
 - o Less rotor losses
 - o Cold rotor
 - o Lower maintenance requirements
- + Higher efficiency
- + Potentially higher power density within the same frame size
- + Lower rotor inertia

Main improvements with respect to IM comes from the fact that SynRel has no conductors in rotor, which brings lots of benefits from design and maintenance stand points. It is estimated that approximately 25% of total losses in IM is coming from the rotor. It is well known that in any EM rotor is the most difficult part to cool. Hence this leads to conclusion that the SynRel is a *cold rotor* machine. Majority of SynRel's losses are generated in the stator (copper losses), where it is generally

easier to remove the heat. Nevertheless, along with the highlighted advantages the disadvantages of SynRel with respect to IM can be highlighted as:

- No-direct online operation (unless caged rotor)
- Lower power factor [42]
- Cross-saturation [43]
- Not as widely accepted by industrial society

Considering the machine design, SynRel can be sized for the exactly same frame as an equivalent IM, however the achieved efficiency will meet the IE4 efficiency or even IE5. ABB is one of the first manufacturers that started commercial production of the SynRel that meet IE4 for power ratings from 1.1kW to 315kW [28]. The same frame size SynRel can reduce the losses while delivering the same or higher power, which was demonstrated by ABB's offering [44]. These machines reduced size and higher rated power and increased efficiency than their IM counterpart.

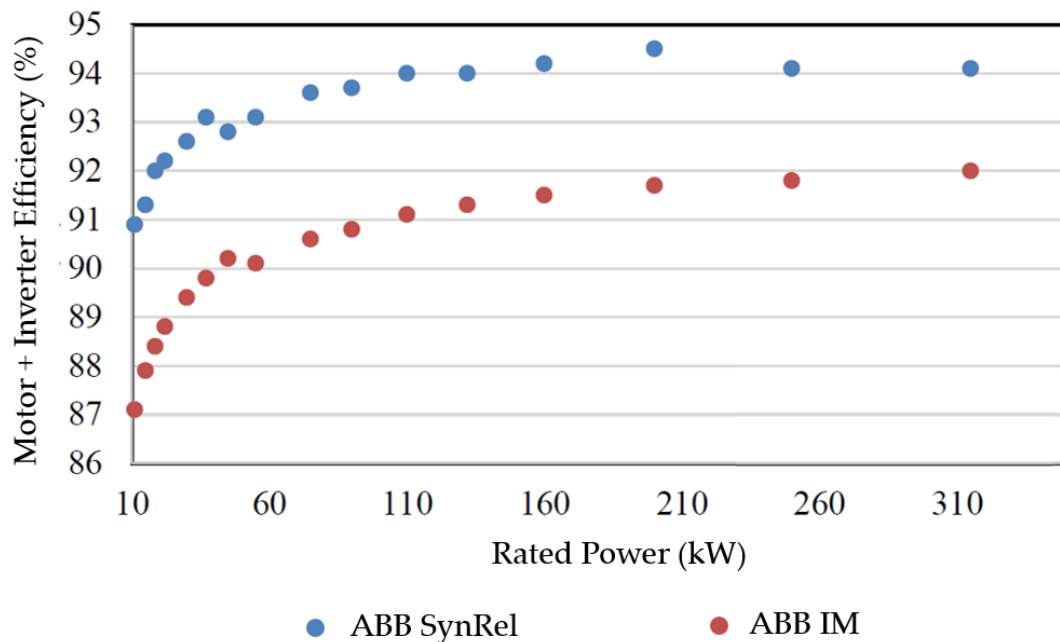


Figure 1.3. IM and SynRel efficiency based on ABB's data, 2014

To illustrate the superiority of the SynRel IE4 that is marketed by ABB, Figure 1.3 is presented. The relative package efficiencies are depicted [28] (motor and inverter losses) over the offered rated power range for both IM and SynRel. The presented efficiencies for rated torque and speed conditions. Both SynRel and IMs considered are self-cooled, 4 pole and were designed to work at 50Hz with the suitable drives.

If considering PM synchronous machine and SynRel both have similar operation principles as both operate at synchronous speed, and contain no rotor conductors. Hence, the rotor losses are reduced compared to IM. However, the rotor's field is delivered by permanent magnets which are lossy in different way (eddy current losses PM surface). There is no doubt that the PM machines have superior torque density. However, there are number of advantages of SynRel over PM machines:

- + No PM
 - o Significantly reduced cost
 - o Easy assembly and manufacturing
 - o Reduced risk in supply chain
- + Robustness (No PM demagnetization risk)
- + Increased starting torque

Lack of PMs are the main advantage of the SynRel which brings a lot of benefits. Nevertheless, the PM machine still have obvious advantages over SynRel. SynRel is expected to have:

- Lower power density
- Lower power factor
- Increased inverter requirements

Considering the example of the ABB's modern process performance motors line up which includes IMs and PM motors as well the SynRels. The IMs are capable to meet the IE2 to IE4 standards up to 1200kW. The PMs mainly aimed for higher torque dense solutions up to 2500kW. Whereas the "award winning" SynRel is aimed to fill the gap in performance and efficiency between conventional IMs and PM machine [28] ,[27]. The main advantages of the SynRel that are listed by ABB are lack of any rotor excitation (no winding or magnets) as well as the service-friendliness of an IMs as there is no magnetic forces in rotor. One of the recent advancement according to [27], is the new IE5 SynRel drives from ABB. These motors meet the requirements of the IEC 60034-30-2 and are in power range of 5.5 to 315kW. They are specified as a Gold Standard efficiency IE5 VSDs.

According to Tero Helpio who is the global product manager, IEC LV motors of ABB motion: *"Climate change and environmental responsibility are driving huge changes across all industries. We have responded to this challenge with our IE5 ultra-premium motors that meet the most stringent energy efficiency standards. These motors offer industrial users a great opportunity to reduce their electricity usage and CO₂ emissions while also benefiting from increased productivity and lower life-cycle costs."*

Several advantages of SynRel over IM and PM machine were discussed by [12], [10], [45]. In summary, SynRel has higher efficiency compared to IM and significantly lower price compared to PM machines thanks to lack of rare earth materials. Considering a rotor with no conductors and permanent magnets translates in robustness and less losses.

High energy efficiency and the simple structure have pushed the SynRel into research field and now manufacturers started producing SynRel for various fan, pump and mill type applications. A clear energy saving and some of the operational benefits of the SynRel are obvious if it is compared to the IM. This was proved by providing some industrial case studies. Robustness and cheaper price are the key SynRel's advantages over the PM machines. Also, it has noticeably wider speed range compare to PM machine [46]. Therefore, SynRel is a promising alternative to IM and PMSM.

Based on the all the above there is the evidence that the SynRel has some superiority over the alternative topologies, especially if considering the industrial sector. Biggest challenges can be highlighted as high torque ripple and lower power factor [47].

1.4 SynRel's complex design problem:

Various reasons of adoption of SynRel technology were listed in previous sections. According to statistics that were acquired, thanks to Google Scholar, since 2009 to late 2020, IEEE, IET, Elsevier have published 1789 conferences and journal papers on SynRel technologies. Figure 1.4 presents the number of publications on SynRel topic over the past decade. As can be observed the scientific interest towards SynRel is constantly growing, and for the past decade it reached its peak in 2018.

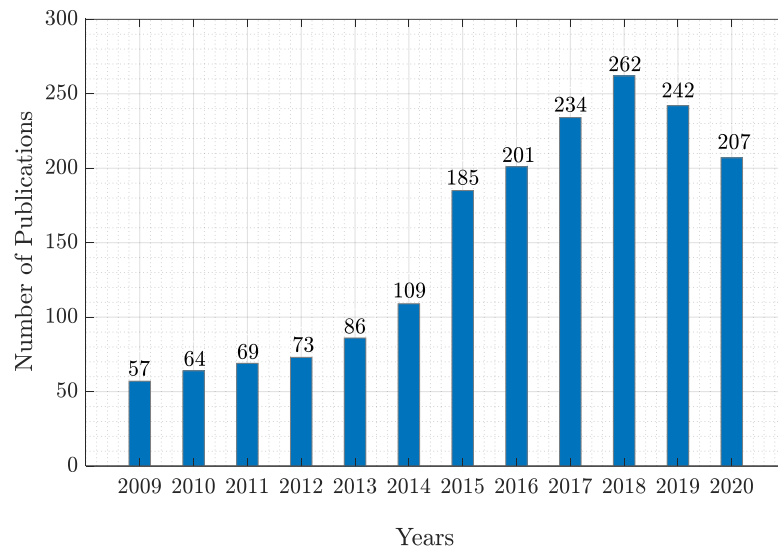


Figure 1.4. Number of Publications on SynRel topic over the past decade

However, SynRel will attract more and more attention due to current trend towards “REE – free” technologies and adoption of IE4-IE5 standards. There are plenty of important works that can be considered for further readings and research purposes, those including: Boldea, [48], [49], [50]; Bianchi [51], [12], [52], [53] etc. This list served as a useful bibliography during the research studies.

At first glance, SynRel topology seems to be very desirable however there are drawbacks associated with the machine design. The main streams of the research works are: maximizing torque [54], [55], [56]; minimizing torque ripple, [52], [57], [19] and performance comparison of SynRel and other topologies, [54], [55], [58], [59],[60], power factor improvements [52], [61], minimizing effect of cross-saturation [43], [62]. The main design challenge comes from the fact that SynRel has a very complex rotor structure and a lot of geometrical parameters are involved in the machine sizing and optimization. There are many attempts to address the rotor’s complexity that are discussed in [55], [63], [64], [65], [66]. However the most widely used rotor design method was introduced in [67]. All rotor’s geometrical parameters according to this method are highlighted in Figure 1.5.

Various analytical methods usually based on the lumped magnetic circuit of the machine are used to identify the optimal distribution of insulation material of the rotor [66], [50]. However, time-consuming optimization step that is performed using Finite Element Analysis (FEA) is still a necessary step to address the main

design parameters (torque ripple reduction, loss reduction etc.). The SynRel rotor complexity naturally increases the time and the steps that are required at optimization stage of the design [68], [69], [65], [19].

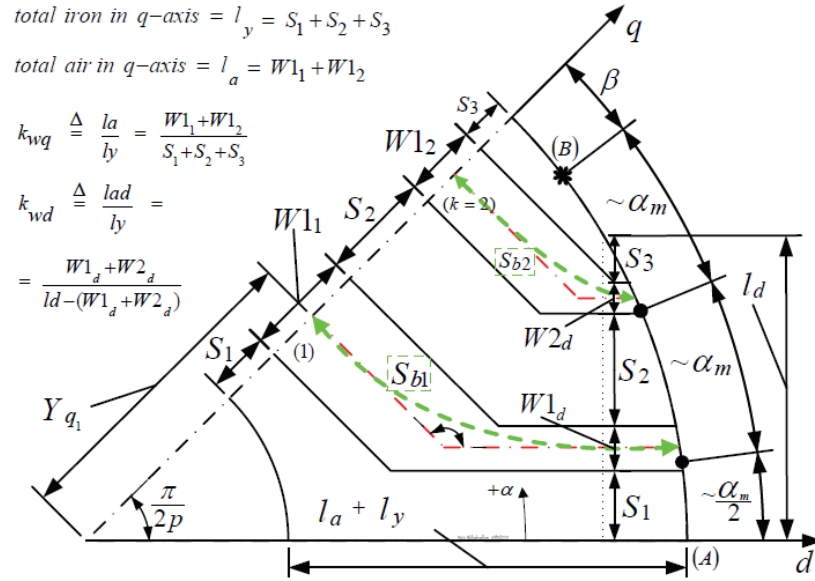


Figure 1.5. Rotor geometry and related microscopic and macroscopic parameters [67].

The computation time varies according to which performance indexes are being optimized (torque, torque ripple, iron losses, etc.) and [19], [20], [70], [71] have been investigated the problem reaching a good trade-off between accuracy and computational burden. On the other hand, the geometrical complexity of the problem can be further reduced acting on how machine geometry under investigation is parametrized. In particular, [71] and [57] present a comparative study among different SynRel rotor flux barrier parametrizations, analysing the compromise between geometrical complexity and achieved performance. It is a general conclusion that adopting a flux barrier profile described by the Joukowski equation [57] and a flux barrier parametrization described by three parameters (barrier thickness, air gap angle and end-barrier parameter) is the best compromise between performance and geometrical complexity [57], [67]. These parameters are also the ones, which most affect the torque performance, and for this reason they usually optimized during the FE refinement. The purpose of this thesis is to show how the FE design stage can be greatly simplified and so computationally relieved by considering a novel dimensioning approaches during the first analytical design.

Chapter 2: Theory of the Synchronous Machines

This chapter presents an analytical model that is generally used for the design and sizing of the Electrical Machines. The main drawback of the method when applied to SynRel is outlined, which is addressed in the novel sizing approach of the SynRel that is presented in Chapter 3.

2.1 Synchronous machines classification:

Synchronous machines can be classified based on the torque production. There are two torque producing phenomena: excitation torque and reluctance torque. Excitation torque is the torque that occurs between two interacting magnetic fields, i.e. PM machine's having rotor field produced by permanent magnets and stator field generated by stator winding and core. Rotating stator field pushing the rotor's permanent magnets, hence rotating the rotor [72]. Reluctance torque also known as alignment torque, is due to unequal magnetic conductivity of the rotor. Reluctance torque is produced once rotor is trying to establish a more magnetically conductive axis with the stator field [12].

Fundamental torque equation for cylindrical machines in d - q frame, actually represents both phenomena:

$$T_{dq} = 1.5p[(L_d - L_q)i_d i_q + \lambda_{pm} i_q] \quad (2.1)$$

Where $(L_d - L_q)i_d i_q$ is the reluctance component, hence $\lambda_{pm} i_q$ is the excitation part of the equation. The relative proportion of the excitation and reluctance torque components will depend on the amount of the PM (or any other rotor field source) and the amount of rotor's magnetic saliency. Hence, there are an infinite possible combinations that can be applied in (2.1) [12]. Saliency ratio is one of the important parameters for reluctance machines and it is written as:

$$\xi = L_d/L_q \quad (2.2)$$

The effective way to visualise the classification of synchronous machines is presented on Figure 2.1.

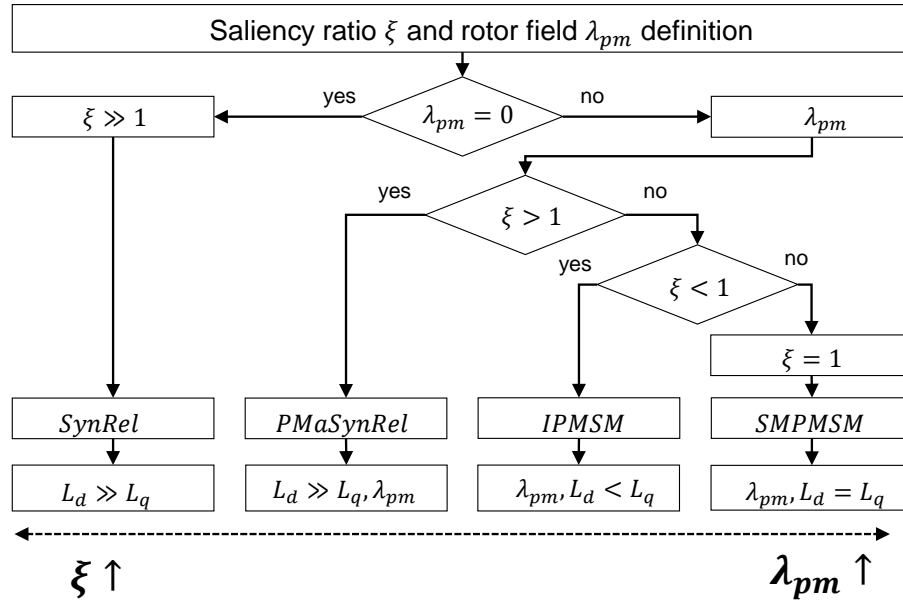


Figure 2.1. All possible combinations of reluctance and excitation torque components.

On Figure 2.1, saliency ratio quantifies the capability of the reluctance torque. Figure 2.1 highlights 4 main synchronous machines topologies. SMPMSM is a surface mount PM machine, which has no saliency ($\xi=1$). This topology contains pure excitation torque (2.1). IPMSM is an interior PM machine, it has saliency, however mainly relies on excitation torque component. PM assisted synchronous reluctance machine (PMaSynRel) that is designed in such way, that machine mainly rely on reluctance. Whereas SynRel is a pure reluctance torque machine. All 4 rotor topologies are presented in Figure 2.2.

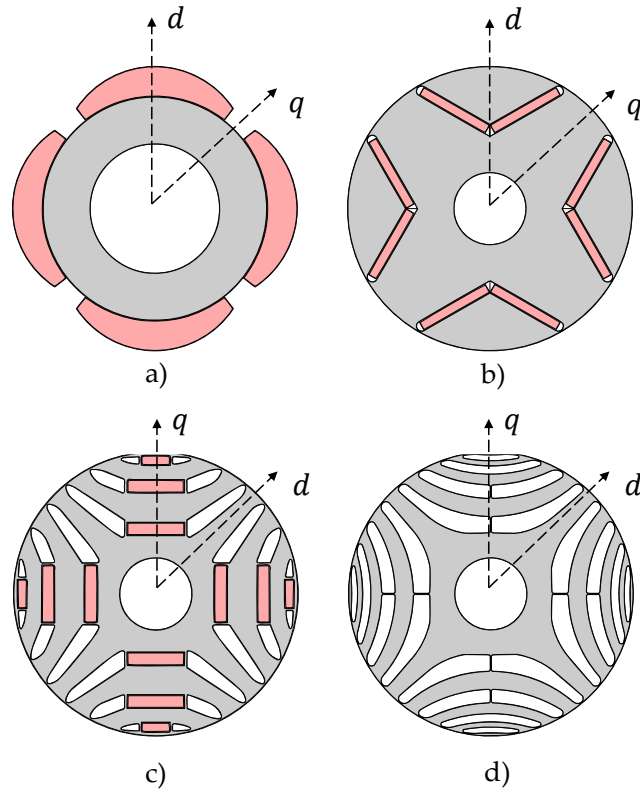


Figure 2.2. PM to reluctance machine topologies.

The common way of representing the d - q axis for PM machines is that the d - axis is aligned with the magnet direction Figure 2.2 a) and b), and for reluctance machines the d - axis is aligned with the more magnetic flux path. This is because as a convention the d - axis is considered the one with higher flux, and in SynRel motors represents the axis with lower reluctance. Figure 2.2 c) and d) [73]. Hence the equation (2.1) can be rewritten for reluctance machines as:

$$T_{dq} = 1.5p[(L_d - L_q)i_d i_q + \lambda_{pm} i_d] \quad (2.3)$$

As can be observed on Figure 2.1 a) surface PM rotor exhibit no saliency, this rotor topology has a uniform iron rotor, whereas the permanent magnets are mounted on top of it. Hence the magnetic conductivity of d and q axes is ideally uniform ($L_d=L_q$), when the machine is not highly saturated. The inductances of the surface mounted PM is very low, since the magnet has very lower relative permeability. Hence the magnets, which are mounted on the rotor iron's surface increase the effective air gap length. The magnets are exposed directly to the armature field, hence are tend to partial irreversible demagnetization [74]. This

topology has the highest amount of the excitation torque. As the two interacting fields of the rotor and stator are exposed directly at the air gap.

The Interior PM rotor has the magnets buried in rotor lamination, hence introducing saliency, as the rotor's iron geometry is non-uniform. The magnetic conductivity of d and q axis is not equal, as the magnets that are placed in q – axis direction has lower magnetic permeability compared to the iron ($L_q > L_d$). Multilayers of magnets can be used to further increase the saliency. One of the advantages of the IPM machines are that the magnets are effectively shielded from the demagnetizing armature field during the flux weakening operation [75]. Due to fractional saliency, these types of machine are usually operated at second quadrant of the $id-iq$ plane. It was discussed in [75], that the d -axis inductance is usually higher compared to an equivalent SPM machine, therefore generally IPM machines are more suitable for the extended speed operation. The constant power in flux-wakening mode of operation is achievable at lower current ratings compared to surface mounted PM machine [76], [77].

PMaSynRel rotor as shown on Figure 2.1 c) usually has weaker magnets or lower magnet volume, hence indicates less excitation torque compared to IPMSM, however it has much higher saliency due to higher number of magnetic insulation paths. The interior flux barriers, are placed in q -axis direction ($L_d > L_q$). In order to increase the reluctance torque component, the rotor anisotropy is maximised by introducing more than one flux barrier [78]. This topology shares similar features with IPMSM, as the constant power is achievable at flux-weakening operation. Insertion of the magnets causes saturation of the iron ribs, therefore reduces the leakage flux for a wider currents and minimizing the L_q . As the PMaSynRel machines mainly rely on the reluctance torque component, it exhibits several drawbacks related to the torque ripple and mechanical constrains related to the flux barriers [19], [79].

Pure Reluctance rotor has no magnets, hence exhibits no excitation torque. This topology has much higher magnetic insulation ratio in q -axis compared to other topologies ($L_d > L_q$) [66]. Similarly, to PMaSynRel, SynRel machine usually have higher number of flux barriers, which leads to the rotor mechanical constrains, as well as the higher torque ripple. Due to the presence of the iron ribs which physically hold the whole rotor structure together, the cross saturation effect occurs [80], [62]. As the d and q rotor axes are not completely magnetically isolated. Hence, an accurate evaluation of the machine's electromagnetic performance is required.

2.2 Torque performance comparison:

One of the important factors of the machine operating principle is the machine excitation - control strategy [81], [82]. The amplitude and angular orientation of the stator current with respect to rotor periphery are two important variables to determine the amount of torque that can be generated. The current excitation angle is defined using i_d and i_q currents (2.1) as:

$$\alpha^e = \tan^{-1} \frac{i_q}{i_d} \quad (2.4)$$

The torque performance can be evaluated on i_d - i_q plane. This common analysis technique is performed to evaluate the control strategy at different current levels. Based on this the maximum torque per ampere or MTPA control strategy can be derived [83].

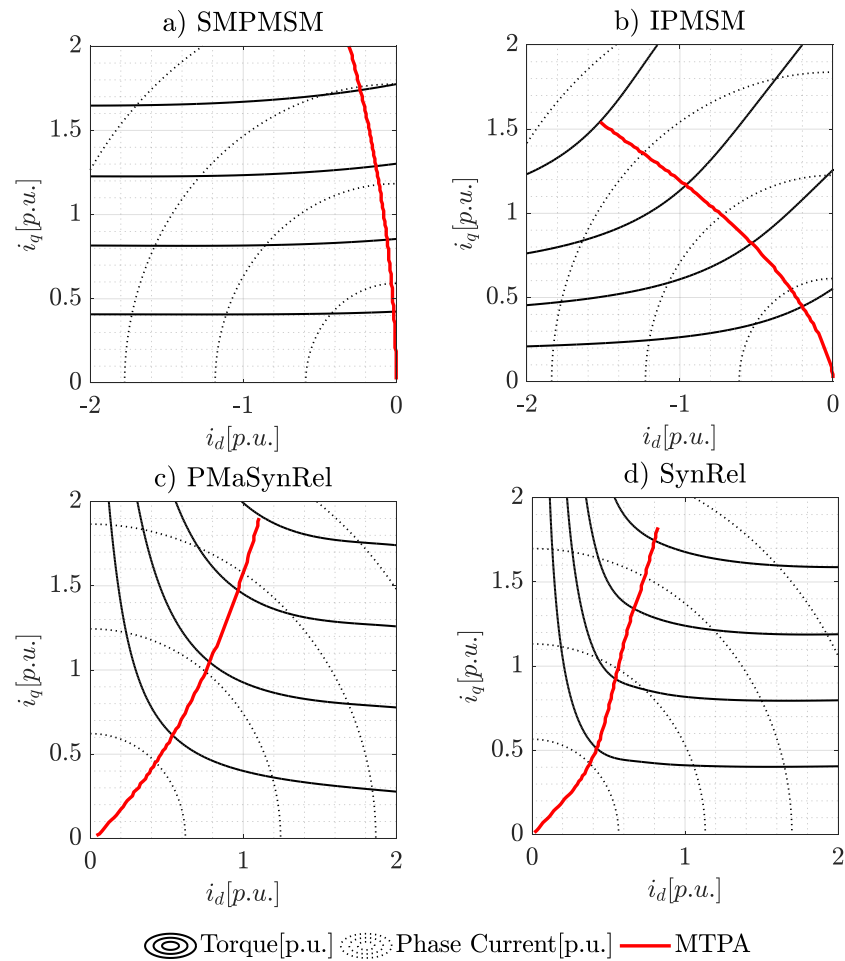


Figure 2.3. Iso torque curves with highlighted MTPA.

To better visualize the torque operation of different synchronous machine topologies, the *iso* torque curves are presented in Figure 2.3. For this example 4 main machine topologies Figure 2.1 and Figure 2.2 are used to reflect the excitation-reluctance torque conditions at different current amplitudes and excitation angles based on equations (2.1), (2.2), (2.4). The following example presents typical torque behaviour for all 4 topologies in p.u.

As can be observed on Figure 2.3 a) the SMPMSM torque performance depends only on i_q , however at higher currents the MTPA requires a negative i_d , this happens as the *d-axis* inductance saturates at lower currents compared to *q-axis*. The torque curves appear to be mainly straight lines. The torque levels dependent primarily on i_q .

Since IPMSM has both reluctance and excitation torque components Figure 2.3 b), it requires both i_d and i_q currents in order to follow MTPA. Since the *d-axis* inductance is smaller than *q-axis* inductance, higher torque is achieved with the negative i_d . The torque curves are proportional to both i_d and i_q , hence the detailed electromagnetic analysis is required to derive the MTPA look up table.

The PMSynRel topology Figure 2.3 c) operates in the first quadrant as the *d-axis* inductance is greater than the *q-axis* inductance. As can be observed the PMSynRel's torque curves are somewhat mirror the IPMSM torque behaviour with respect to the i_q axis, however the MTPA is more inclined towards the i_q axis. It is important to note that for this topology the rotor's *q-axis* is aligned with the magnet, hence the i_d is required for excitation torque (2.2).

As can be observed on Figure 2.3 d) the SynRel topology's MTPA is further inclined towards i_q axis compared to PMSynRel, as there is no excitation torque component. The SynRel's torque curves highly dependent on *d-axis* inductance saturation levels, whereas it is desired to minimize the *q-axis* inductance.

In summary it can be concluded that saliency is an important factor of the torque performance for IPMSM, PMSynRel and SynRel topologies, as it responsible for the reluctance component of torque (2.1), (2.2). Saliency is mainly dependent on the rotor's interior geometry Figure 2.2. Hence the following chapter will focus on justifying the importance of considering the rotor's saliency at the preliminary design stage.

2.3 Classical sizing approach:

To investigate the importance of considering saliency at the preliminary machine design stage let's consider the classical sizing approach. The first step for a machine design is to roughly estimate the size of the main components. It is well known [84], [85] that the main electromagnetic sizing equations for an electrical machine are related to the torque. Therefore, this chapter will focus on the classical electromagnetic sizing of the cylindrical electrical machine, and their effect on the torque.

The generalized torque relation for common, cylindrical machines can be derived from the magnetic field energy in the machines' air-gap. One of the common ways to relate the machine dimensions to the specification is Utilization Coefficient C_u [84]:

$$C_u = \frac{P}{2\pi n V_{ag}} \quad (2.5)$$

Where P stands for apparent power, n is the rotational speed and V_{ag} is the EM's volume at the air gap, which is defined as:

$$V_{ag} = \frac{\pi D_{si}^2}{4} L_{stk} \quad (2.6)$$

Equation (2.6) is derived intuitively, as the geometry considered is a cylinder-type rotor, where D_{si} is the stator inner diameter or air gap diameter and L_{stk} is the stack length. Therefore, equation (2.5) can be reduced to:

$$C_u = \frac{P}{n D_{si}^2 L_{stk}} \quad (2.7)$$

In [86] it was shown that the machine constant C_u is related to magnetic and electric loading values. For synchronous and asynchronous three phase machines the relationship can be derived using the power equation:

$$P = 3EI \quad (2.8)$$

Where E is back EMF value and can be derived as:

$$E = \frac{1}{\sqrt{2}} 2\pi f N_s \phi k_w \quad (2.9)$$

Where k_w is the winding coefficient, N_s is the number of turns per phase and ϕ is the flux per pole. Flux per pole can be written with respect to the peak air gap flux density value B_{max} as:

$$\phi = \frac{B_{max}L_{stk}D_{si}}{p} \quad (2.10)$$

Where p is pole pairs. Using equation (2.10) the back emf equation can be rewritten as:

$$E = \frac{D_{si}}{p\sqrt{2}}(2\pi f)N_s B_{max}L_{stk}k_w \quad (2.11)$$

Electric loading or linear current density A of the machine can be defined according to stator's slot pitch τ_s and the rms value of the stator slot current I_s , whereas the number of slots in stator is defined as Q_s :

$$A = \frac{I_s}{\tau_s} \quad (2.12)$$

$$\tau_s = \frac{\pi D_{si}}{Q_s} \quad (2.13)$$

Number of conductors per slot is defined as:

$$Z_Q = \frac{2N_s m}{Q_s} \quad (2.14)$$

Where m is the number of phases. Hence equation (2.12) can be rewritten as:

$$A = \frac{2I_s N_s m}{\pi D_{si}} \quad (2.15)$$

Considering a 3-phase circuit, current can be written as function of the electric loading as:

$$I = \frac{\pi A D_{si}}{6N_s} \quad (2.16)$$

Using equations (2.16) and (2.11), apparent power of electrical machine can be written as:

$$\begin{aligned} P &= 3 \left[\frac{D_{si}}{p\sqrt{2}}(2\pi f)N_s B_{max}L_{stk}k_w \right] \times \left[\frac{\pi A D_{si}}{6N_s} \right] \\ &= [A \cdot B_{max} \cdot D_{si}^2 L_{stk}] \times \left[\frac{\pi^2 k_w f}{p\sqrt{2}} \right] \end{aligned} \quad (2.17)$$

Hence, utilization coefficient can be rewritten using (2.7) and (2.17):

$$C_u = [A \cdot B_{max}] \times \left[\frac{\pi^2 k_w}{60\sqrt{2}} \right] \quad (2.18)$$

Utilization coefficient C_u expresses the effective utilization of the electrical machine volume. C_u is inversely proportional to machine volume; therefore, bigger

C_u means smaller machine. Therefore, if fixing the electric loading and magnetic loading B_{max} , the machine volume at the air gap will depend on the ratio of P/n . The relationship of torque to volume can be derived using mechanical power equation:

$$P = T\omega \quad (2.19)$$

Where ω is the speed in rad/s. Hence the torque equation is:

$$T = [A \cdot B_{1g} \cdot D^2 L_s] \times \left[\frac{\pi}{2p\sqrt{2}} \right] \times [k_w] \quad (2.20)$$

The generalized torque relation for common, cylindrical machines is derived from the magnetic field energy in the machines' air-gap (2.20). This depends on the machine volume and is expressed as in [86]. Various adaptations of this sizing technique have been discussed in literature [2], [4]. However, the most common approach is traditionally based around the relationship between the volume and the two main constraints of any machine (2.20), namely the magnetic limit and the thermal limit [88], [89].

When used as a preliminary sizing scheme, e.g. for classical analytical sizing tools, then it is well-known that for most common machines this approach can yield excellent preliminary design results [87], [90]. Part of this accuracy comes from the fact that most preliminary sizing operations do not include the machine's saliency ratio at the preliminary design stage. Therefore, for machine topologies where saliency is not so significant, the above approach is quite accurate.

However, when the approach is applied to machines where saliency does play a significant and dominant role, more accurate design methods, such as finite element (FE) analysis, are required [91].

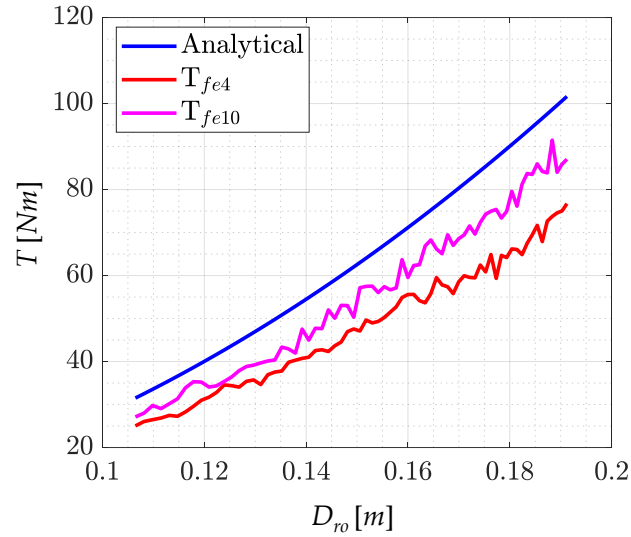


Figure 2.4. FE and common analytical sizing approach comparison.

Figure 2.4 presents the results of the exercise that was performed to evaluate the sizing approach (2.20). This was done for the wide range of the SynRel geometries. Two different rotor topologies were studied by means of FE, 4-barriers configuration and 10-barriers configuration. For both geometries the magnetic insulation ratio (total thickness of air path in q-axis/total thickness of rotor lamination) was kept the same $k_{air}=0.43$. The stator configuration was kept the same for both machines with total number of slots $Q_s=48$. Stack length for all geometries was proportional to the rotor outer diameter, $L_{stk} = D_{ro}$. The rest of the test details are presented in Table 2.1. The SynRel rotor geometries that were under test are presented in Figure 2.5.

Table 2.1. Sizing evaluation test.

Symbol	Parameter	Quantity
J	Current Density	12 A/mm ²
R_{ro}	Rotor radius range	[0.1065m, 0.1912m]
FEA Nodes	Average number of nodes per simulation	12000
α^e	Average current angle	~60°
g	Air gap	0.5 mm

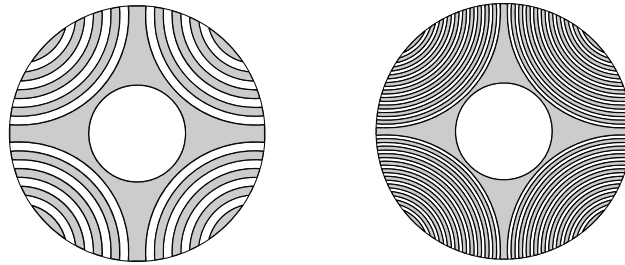


Figure 2.5. SynRel geometries under test.

As can be observed on Figure 2.4, two geometries have different torque performance, as the 10-barrier configuration provides higher saliency compared to 4-barrier configuration. Since the classical sizing approach is unable to consider the rotor's geometry (2.5) - (2.20), two geometries have the same analytical torque profile Figure 2.4. The average error of the 4-barrier configuration is ~24%, whereas the average error of the 10-barrier configuration is ~14%. Hence it can be concluded that the classical analytical sizing approach is inaccurate when applied on the SynRel machines.

This defeats the whole purpose of a preliminary sizing tool and automatically 'forces' the machine designer towards time-consuming FE iterations right from the start of the design process. However, if an analytical method that is able to consider the saliency ratio at all the design stages is used, then the time required for the initial sizing of the machine can be significantly reduced.

A case in point for the above is the Synchronous Reluctance (SynRel) machine, where the rotor geometry has an important effect on the machine's saliency ratio. Therefore, for SynRel machines, the latter is a critical parameter that needs to be included in any analytical sizing method.

Chapter 3: Analytical model for SynRel sizing

This chapter presents a simple analytical model that later will be used for the sizing of Synchronous Reluctance (SynRel) machines. The accuracy of the method is achieved by modelling a simple rotor geometry that presents all the characteristics of a real machine. The analytical equations proposed are able to guarantee accurate and fast results during the preliminary design of the machine.

3.1 Introduction:

An analytical sizing approach for SynRel machines that is able to consider the saliency ratio is proposed in this chapter. The methodology is applied to SynRel machines with Axially Laminated Anisotropic (ALA) rotor types [50] and to SynRel machines with Transversely Laminated Anisotropic (TLA) rotors [53].

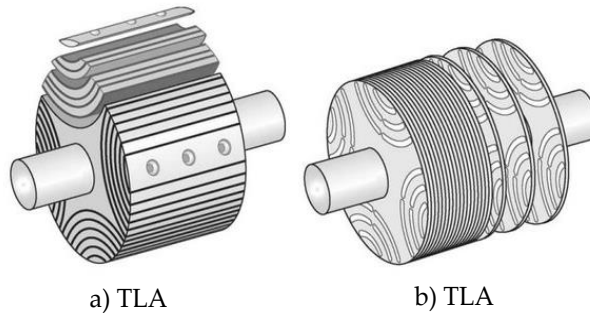


Figure 3.1. ALA and TLA SynRel topologies. [50], [53].

In this chapter, the proposed method is shown to result in very good accuracy, while also comprising an inherent flexible nature that allows for appropriate fine-tuning of the method itself. The approach relies on accurate estimations of the direct and quadrature inductance values, also known as the saliency ratio. The proposed method was successfully validated by a sets of FEA simulations as well as by experimental results, performed on a SynRel machine rated at 15kW.

3.2 Analytical Derivation:

The analytical method described in [50], [48] uses the $d-q$ frame parameters to model an ALA SynRel machine. In these works, the emphasis was on the importance of considering the saliency ratio while adapting the well-known electromagnetic reluctance torque relation in a $d-q$ frame for machine design [6].

The torque equation is given in (3.1), where p represents the number of pole pairs, L_d and L_q are the direct and quadrature inductances, respectively; and I_d, I_q are the direct and quadrature currents flowing in the stator windings.

$$T_{em} = \frac{3}{2} p (L_d - L_q) i_d i_q \quad (3.1)$$

In (3.1), the main electromagnetic variables are the direct and quadrature axis inductances. In a reluctance motor within a d - q – reference frame, the d – axis is the path of least reluctance and the q – axis is the path of greater reluctance; reflecting into unequal inductances, dependent on the rotor position. Hence, when $L_d \neq L_q$ an “alignment” torque, alternatively known as the reluctance torque, is present.

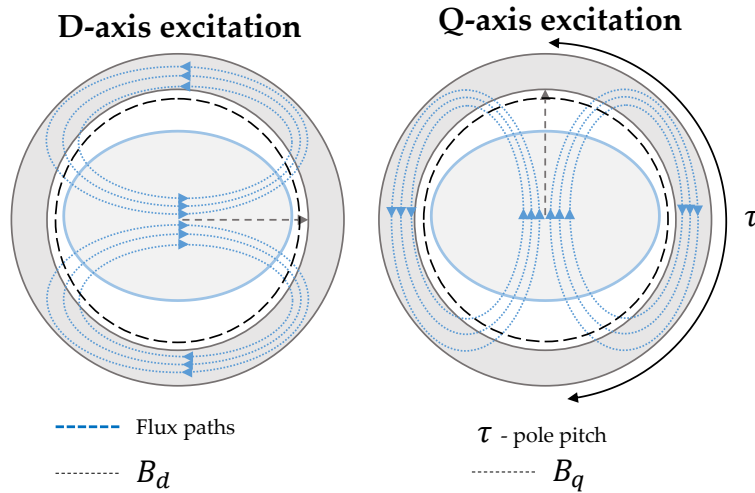


Figure 3.2. Salient pole rotor's field distribution.

For such cases, the magnetic conductivity along the rotor surface is not equal. Therefore, the resulting air-gap flux densities can be defined as shown in (3.2) and (3.3), where B_d and B_q are the flux densities along the d and q axis, respectively as shown in Figure 3.2, where field distribution is sketched for a simple salient pole rotor; $g_d(x)$ and $g_q(x)$ are the air gap functions and $F_d(x)$ and $F_q(x)$ are the magneto motive forces (MMF) produced by the stator, which are position dependent (x):

$$B_d(x) = \frac{\mu_0 F_d(x)}{g_d(x)} \quad (3.2)$$

$$B_q(x) = \frac{\mu_0 F_q(x)}{g_q(x)} \quad (3.3)$$

If B_1 represents the fundamental component of the air-gap flux density for a uniform air-gap machine (no saliency) and B_{1d}, B_{1q} are set to be the fundamental components of B_d and B_q . Their ratios represent the magnetizing inductances L_{dm}/L_m

and L_{qm}/L_m as shown in (3.4) and (3.5), where K_{dm} , K_{qm} are the magnetizing coefficients, L_{dm} , L_{qm} are the direct and quadrature magnetizing inductances and L_m is the magnetizing inductance of a solid cylindrical rotor.

$$K_{dm} = \frac{L_{dm}}{L_m} = \frac{B_{1d}}{B_1} \quad (3.4)$$

$$K_{qm} = \frac{L_{qm}}{L_m} = \frac{B_{1q}}{B_1} \quad (3.5)$$

Consequently, the saliency ratio ξ can then be defined as shown in (3.6), where L_l represents the leakage inductance:

$$\xi = \frac{L_d}{L_q} = \frac{L_{dm} + L_l}{L_{qm} + L_l} = \frac{L_m K_{dm} + L_l}{L_m K_{qm} + L_l} \quad (3.6)$$

Considering that the values of peak MMF ($n_s I_s$), n_s – number of turns, I_s – peak phase current, should be the same for both the d and q axis excitations, then it can be said that the values of K_{dm} and K_{qm} are entirely geometrical parameters and can therefore be analytically derived.

On the other hand, the magnetizing inductance L_m (3.6) has a nonlinear dependence on the machine MMF, due to the magnetic saturation of steel. However, L_m can be determined for the linear region using an analytical inductance model to form an initial design, which can be further improved, later on using FE modelling. [92]

3.2.1 d - q parameters approximation:

The main inductance of a single phase of the stator winding L_{sp} can be calculated using the peak values of a single-phase flux linkage λ_s and the stator phase current I_s [1, 11]. L_m is determined by multiplying L_{sp} by a factor of $m/2$, where m is the number of phases, due to the mutual inductance between phases. For 3-phase machines, the magnetizing inductance is calculated as shown in , where D_{ro} is the rotor diameter, L is the stack length, q is the number of slots per pole per phase, g is the air gap length, μ_0 is the relative permeability of air. K_{w1} and K_s are winding factor and saturation coefficient, respectively.

In (3.7), the parameters D_{ro} and L are the variables of interest as these determine the size of the machine. These will be derived later based on the torque requirements (3.1) and (3.7).

$$L_m = \frac{3}{2} L_{sp} = \frac{3}{2} \frac{\lambda_s}{I_s} = 3\mu_0 D_{ro} L \frac{(qK_{w1}n_s)^2}{g(1 + K_s)} \quad (3.7)$$

The values of the excitation currents in the d - q frame then need to be derived to determine the torque through (3.1). A common way to evaluate the values of I_d and I_q is to consider them as parts of d - q frame MMF values F_d and F_q , which are closely related to the air gap flux density, that can be calculated using (3.2),(3.3).

The general equation for the fundamental component of the direct axis air gap flux density can then be derived from (3.4) - (3.6). This is shown in (3.8):

$$B_{1d} = \frac{B_1}{\sqrt{1 + \left(\frac{K_{qm}}{K_{dm}}\right)^2 \xi}} \quad (3.8)$$

Consequently, the stator MMF in the d - q frame can then be derived as given by (3.9) and (3.10) :

$$n_s I_d = \frac{B_{1d} \pi g (1 + K_s)}{3\sqrt{2} \mu_0 q K_{w1} K_{dm}} \quad (3.9)$$

$$n_s I_q = n_s I_{dm} \sqrt{\xi} \quad (3.10)$$

Considering (3.1) and (3.4) - (3.10), it is clear that the magnetizing coefficients K_{dm} and K_{qm} are solely dependent upon the machine topology. Therefore, for salient pole machines the values change, whereas for a non-salient machine, the value is equal for both direct and quadrature axes.

Utilizing equations (3.4) - (3.10), all the d - q reference frame parameters for any machine topology can be derived, and subsequently used to estimate the torque through (3.1).

3.2.2 Linear sizing:

As can be observed in (3.1), torque is directly proportional to the difference between L_d and L_q . Thus, minimizing L_q results in an increasing torque. This suggests that L_{qm} is mostly a leakage inductance. Therefore, it can be said that the fundamental component of the field is mainly found in the d -axis component.

Therefore, considering $L_d \gg L_q$ as a first approximation, then the saliency ratio can be expressed by (3.11):

$$\xi = \frac{L_d}{L_q} = \frac{L_{dm} + L_l}{L_{qm} + L_l} = \frac{L_m K_{dm} + L_m K_{qm}}{2L_m K_{qm}} \quad (3.11)$$

Therefore, the magnetizing coefficients ratio can be described by (3.12):

$$2\xi - 1 = \frac{K_{dm}}{K_{qm}} \quad (3.12)$$

If the machine presents only a reluctance component, in the case of a SynRel motor, then the rotor outer diameter (D_{ro}) can be written based on (3.1) and (3.7) - (3.12) as :

$$D_{ro} = \sqrt{\frac{T_{em} \gamma \mu_0 q K_{dm} \sqrt{\xi}}{B_{1d}^2 \pi g (1 + K_s) \sqrt{1 + \left(\frac{1}{2\xi - 1}\right)^2 \xi}}} \quad (3.13)$$

From (3.13), the importance of saliency for reluctance machines and the main machine sizing ratio, represented by the aspect ratio, can be observed. The aspect ratio is proportional to the machine stack length and inversely proportional to the outer rotor diameter [86]:

$$\gamma = \frac{L}{D_{ro}} \quad (3.14)$$

Based on (3.13) it is clear that the main geometrical input parameters of the rotor sizing equation are the air-gap g and the aspect ratio γ . The saliency ratio ξ is one of the parameters required to determine D_{ro} . As ξ is directly dependent on the rotor topology, then it needs to be properly defined. The typical saliency ratio value is $\xi \leq 10$ for TLA and $\xi > 10$ for ALA [93].

From all the above, it can be concluded that the main parameters that define the saliency ratio are the magnetizing coefficients given by (3.6). Since, in (3.7), L_m has been determined in the linear region of a magnetic circuit of the machine and referring to (3.6) and (3.11), it can be concluded that the unsaturated saliency ratio is a geometrical parameter.

Based on (3.4) and (3.5), K_{dm} and K_{qm} can be estimated using an air gap flux density distribution of the d and q axis rotor excitation. One of the analytical techniques that can be used to estimate the air gap flux density distribution for (3.2) and (3.3) is the air gap function method [94].

The air gap function method is the most suitable when uneven magnetic conductivity throughout the periphery of the air gap needs to be considered $B_d \neq B_q$. This method is less complex than other approaches that determine the flux density distribution, yet still manages to reflect uneven magnetic conductivity, for both salient pole as well as TLA and ALA rotor topologies [95].

3.3 Air Gap Function Approach for Saliency Derivation:

The air-gap function is an analytical method that is widely used to calculate air-gap flux density, due to its consideration of the rotor and stator slotting effects. In [50], an approach for the computation of the field distribution was presented for the ALA topology of a SynRel, however the stator slotting effects were neglected. In [95], a method for the accurate prediction of the no-load flux distribution of field-excited flux-switching motor (FE-FS) was proposed, including an air gap function in the magnetic circuit. In this case, the rotor topology was that of a salient pole configuration with DC stator excitation. Another variant of a salient pole rotor topology was studied in [94], however AC stator excitation was used and the FEA torque estimation was analyzed in comparison to the values obtained using an air gap magnetic circuit. In summary, the air-gap function approach is used to reflect a stator and rotor slotting effect on the air gap flux density distribution.

The slotting effect can be analyzed and understood using the air gap function method through the generic geometry shown in Figure 3.3.

As can be observed, the machine flux encounters a non-uniform permeability, due to the presence of the slot openings, or if considering a TLA, the saturated iron.

The air-gap function for a salient pole rotor can be derived according to the *infinite slotting* assumption, where the idealized magnetic flux Π_1 and Π_2 are assumed to be equal to quarter circumference of a circle [95], [94].

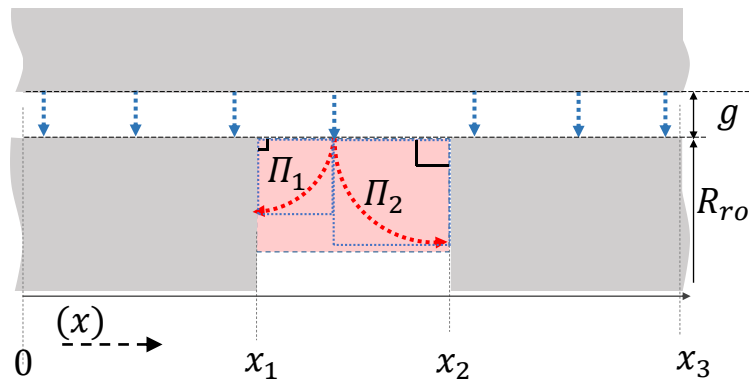


Figure 3.3. Rotor slotting, magnetic flux using infinite slot approach.

The length of the flux lines perpendicular to the rotor can be easily estimated using cylindrical coordinates and the rotor outer radius R_{ro} as presented in equation (3.15), which are position (x) dependent. (x) is an angle expressed in polar coordinates at any position instant, which will be used in further derivations.

$$\begin{aligned}\Pi_1 &= -\pi R_{ro} \sin \frac{x}{2} \\ \Pi_2 &= -\pi R_{ro} \sin \left(\frac{x_1}{2} - \frac{x}{2} \right)\end{aligned}\quad (3.15)$$

Therefore, the total flux path's length can be estimated by using the parallel paths derivation, as described by (3.16).

$$\Pi_1 || \Pi_2 = \frac{\pi R_{ro} \sin \left(\frac{x}{2} \right) \sin \left(\frac{x_1 - x}{2} - \frac{x}{2} \right)}{\sin \left(\frac{x}{2} \right) + \sin \left(\frac{x_1 - x}{2} - \frac{x}{2} \right)} \quad (3.16)$$

As can be observed in Figure 3.3, the total air gap has increased as a result of the additional slot introduced from x_1 to x_2 . The total length of the air flux path for the considered period can therefore be defined as shown in (3.17).

$$g(x) = \begin{cases} g, & 0 < x < x_1 \\ g + \Pi_1 || \Pi_2, & x_1 < x < x_2 \\ g, & x_2 < x < x_3 \end{cases} \quad (3.17)$$

The following method can be used to estimate the air flux paths considering salient pole rotor slotting, as well as the insulation barriers of TLA and ALA SynRel rotor topologies.

3.3.1 Anisotropic rotor geometry considerations:

The SynRel ALA and TLA topologies have a very complex barrier structure comprising a high number of geometrical parameters that must be considered [12]. A typical example is illustrated in Figure 3.4. However, this work is mainly focused on the effects of the saliency and magnetizing ratio on the preliminary sizing of the machine. Thus, to simplify the geometry complexity, only four parameters are considered namely the number of barriers, the insulation ratio, angle span of each barrier and angular thickness of each barrier with respect to rotor surface. This assumption of neglecting the other geometrical parameters is valid because the aim is to derive the magnetic circuit for idealized magnetic condition, i.e. when the iron is magnetically unsaturated hence, the iron reluctance can be assumed to be zero. Therefore, the reluctance is present only due to the air gap and interior rotor barrier insulations, conventionally known to be air.

Considering the generic geometrical parameters, as shown in Figure 3.4, then the comprehensive parametrization of flux barriers can be achieved [7, 13, 14, 15]. The flux barriers are drawn according to a conformal mapping theory and the

Joukowski air-flow potential formulation. The expression for each barrier line is defined by the coefficient C_k , which is described in (3.18).

$$C_k = \sin(p\alpha_k) \frac{\left(\frac{r}{a}\right)^{2p} - 1}{\left(\frac{r}{a}\right)^p} \quad (3.18)$$

The calculated C_k is then used to derive the cylindrical coordinate of each point on the borderline of the barrier. This is done through (3.19).

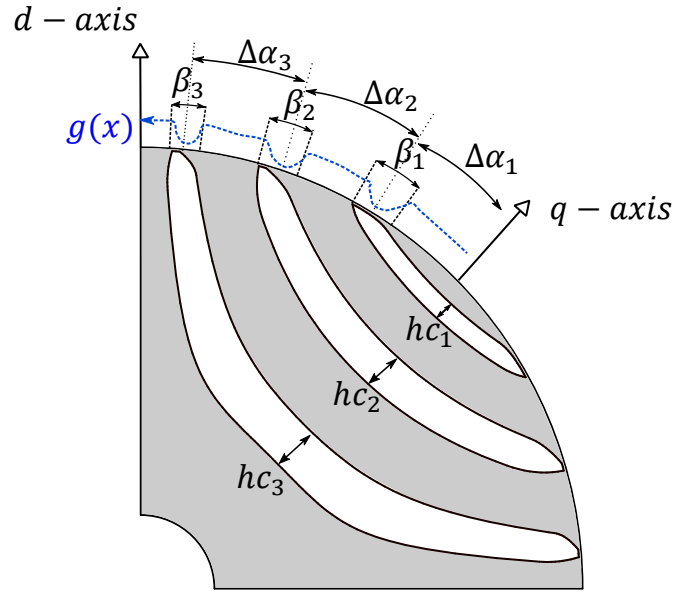


Figure 3.4. Quarter of geometry for anisotropic type rotor (3 – barriers in this case), 4-pole configuration. Based on $\Delta\alpha_k$ (per unit value of α) and hc_k (per unit value of barrier thickness).

$$r(\alpha_k, C_k) = a \sqrt[p]{C_k + \frac{\sqrt{C_k^2 + 4 \sin^2 px}}{2 \sin(px)}} \quad 0 \leq x \leq \frac{\pi}{p} \quad (3.19)$$

All the above shows that having set the geometrical parameters as for example shown in Figure 3.4, then all the parameters of interest can be derived from (3.18) and (3.19). Thus, $\Delta\alpha_k$, i.e. the per unit value of barrier span angle with respect to q -axis, β_k , i.e. the angular thickness of each barrier opening and hc_k i.e. a per unit value that represents the insulation barrier thickness can all be found. The total insulation ratio k_{air} can be derived as an average value of hc_k as described in (3.20).

$$k_{air} = \frac{\sum_k hc_k}{k} \quad (3.20)$$

Using the air gap function approach, the same function with a phase lag of 45° for 4-pole can be derived for the d -axis and q -axis rotor excitation.

However, the q -axis air gap function should include an extra reluctance component due to insulation barriers, in this case air. Therefore, it increases with the air thickness of a flux path.

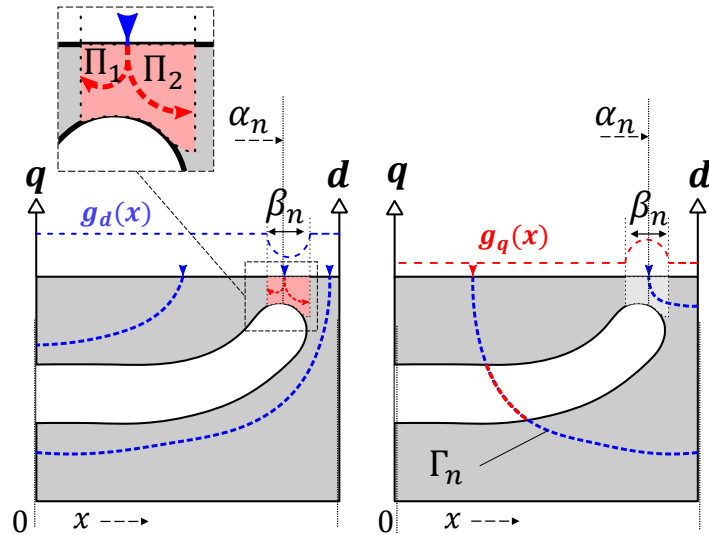


Figure 3.5. Sketch of d -axis (on the left) and q -axis (on the right) flux paths. The rotor barrier slotting effect is highlighted.

Figure 3.5 presents a sketch of d -axis and q -axis excited rotors. Using the air gap function approach, the same function with a phase lag of 45° for 4-pole can be derived for the d -axis and q -axis rotor excitation. Here it is important to define the angular span of the barrier n as α_n and the n th barrier's opening angular thickness β_n . The barrier ribs are highlighted for d -axis rotor excitation. Where the flux paths Π_1 and Π_2 are the flux paths that pass through the saturated ribs.

3.3.2 Air gap function for d-axis excitation:

The thickness of the air-gap for d -axis excitation should only consider the barrier slotting effect as presented in Figure 3.5, by using (3.15) and (3.16). The total rotor air gap function for the n – barriers rotor for the d -axis excitation can be expressed as a position (x) dependent function, which is given in (3.21).

$$g_{rd}(x) = \begin{cases} 0, & 0 < x < x_1 \\ \Pi_1 || \Pi_2, & x_1 < x < x_1 + \beta_1 \\ 0, & x_1 + \beta_1 < x < x_2 \\ \dots & \\ \Pi_1 || \Pi_2, & x_n < x < x_n + \beta_n \\ 0, & x_n + \beta_n < x < x_{n+1} \end{cases} \quad (3.21)$$

The magnetic circuit can be described as shown in Figure 3.7 a), based on the geometrical parameters of the rotor that is shown in Figure 3.4 and Figure 3.5.

3.3.3 Air gap function for q-axis excitation:

For the *q-axis* excitation, the magnetic circuit should be built considering h_{ck} . Therefore, an extra air thickness in this case needs to be considered, such as shown in Figure 3.6.

In case of *q-axis* excitation the barriers openings are considered magnetically conductive due to iron ribs as show in Figure 3.5.

The flux paths can be estimated in a similar method to (3.15) - considering quarter-circular flux paths through a half-pole rotor segment. Therefore, the k_{air} ratio can be used to derive the air barriers thickness with respect to flux paths Γ_1 - Γ_3 depending on position (x) as shown in Figure 3.6.

Using cylindrical coordinates of the flux paths' starting points, the radius of the flux line Γ_n can be derived as (3.22) and the air path thickness as (3.23).

$$R_{\Gamma_n} = \frac{R_{ro} \Delta \alpha_n \pi}{4} \quad (3.22)$$

$$\Gamma_n * k_{air} = \left[\frac{R_{ro} \Delta \alpha_n \pi}{4} \right] \frac{\pi}{2} * k_{air} \quad (3.23)$$

Based on the geometrical parameters from Figure 3.4 and Figure 3.5 and Figure 3.6, the magnetic circuit can be expressed for the *q-axis* excitation as shown in Figure 3.7 b).

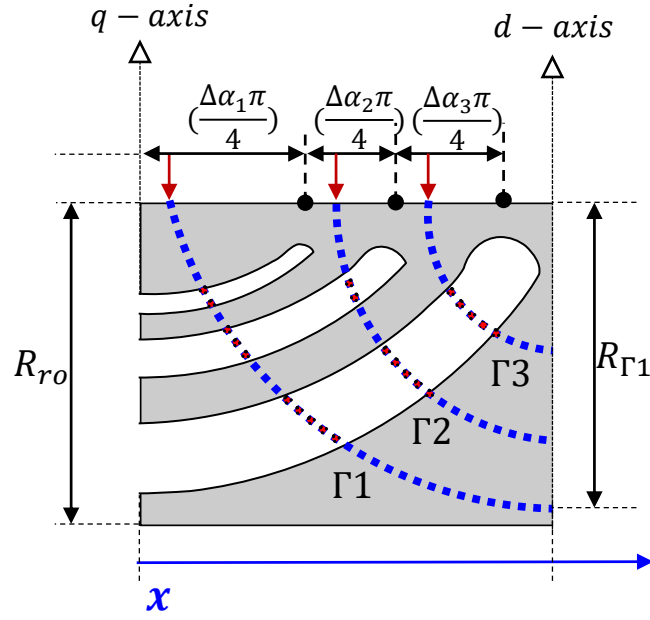


Figure 3.6. Idealized flux paths for q -axis excitation (tangentially flattened rotor), flux path through air barriers is highlighted with red.

Therefore, the rotor air gap function for n – barriers rotor for q -axis excitation can be expressed as a position (x) dependent relationship, as shown in (24).

$$g_{rq}(x) = \begin{cases} k_{air} \cdot \Gamma_1, & 0 < x < x_1 \\ \Pi_1 || \Pi_2 + k_{air} \cdot \Gamma_1, & x_1 < x < x_1 + \beta_1 \\ k_{air} \cdot \Gamma_2, & x_1 + \beta_1 < x < x_2 \\ \dots & \dots \\ \Pi_1 || \Pi_2 + k_{air} \cdot \Gamma_n, & x_n < x < \beta_n \\ k_{air} \cdot \Gamma_n, & \beta_n < x < x_{n+1} \end{cases} \quad (3.24)$$

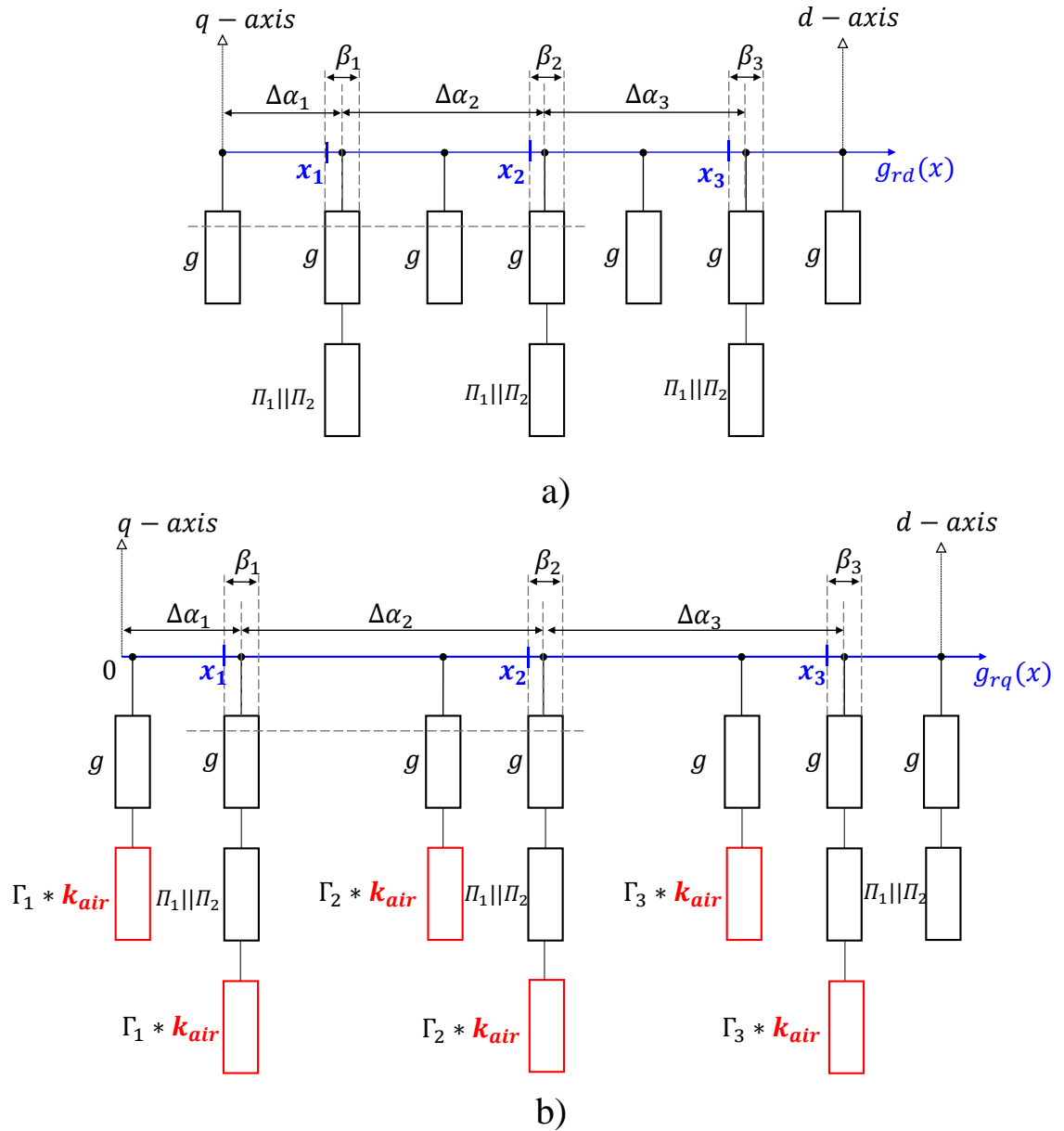


Figure 3.7. Magnetic circuit for a 3 - barriers SynRel rotor, including barrier slotting effect. a) d-axis excitation b) q-axis excitation.

3.3.4 Stator slotting considerations:

When considering the stator slotting effect, the magnetic flux paths can be approximated in a similar manner as (3.15) using an infinite slot assumption. However, the tooth tip can be accounted using the slotting effect with external flux paths, highlighted with red in Figure 3.8.

Thus for a geometry such as shown in Figure 3.8, the angle of an external flux path span can be derived by the relationship described in (3.25), where, w_{sp} is the tooth tip width and h_{s2} is the height of the wedge.

$$\gamma = \sin^{-1} \frac{w_{sp}}{\sqrt{w_{sp}^2 + h_{s2}^2}} \quad (3.25)$$

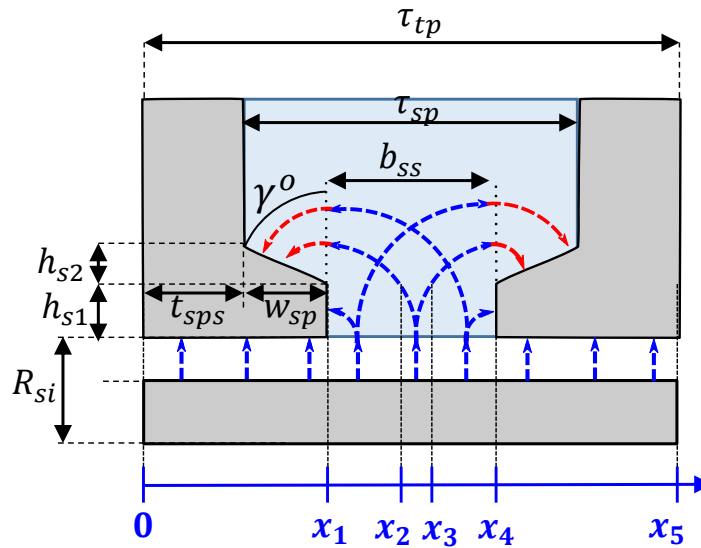


Figure 3.8. Stator slotting, magnetic flux using infinite slot approach, where slotted region is highlighted in blue.

From (3.25), a relationship that describes the flux paths in proximity to the slot opening can be derived and this is shown in (3.26), where Π_{s11} and Π_{s22} are the flux paths extensions due to the tooth tip and Π_{s1} and Π_{s2} are the quarter-circular flux paths.

$$\begin{aligned}
 \Pi_{s1} &= \pi R_{si} \sin\left(\frac{x}{2}\right) \\
 \Pi_{s2} &= \pi R_{si} \sin\left(\frac{b_{ss}}{2} - \frac{x}{2}\right) \\
 \Pi_{s11} &= \left[R_{si} \sin\left(\frac{x}{2}\right) - h_{s1} \right] \gamma \\
 \Pi_{s22} &= \left[R_{si} \sin\left(\frac{x}{2}\right) - h_{s1} \right] \gamma
 \end{aligned} \tag{3.26}$$

Therefore, based on (3.25), (3.26) and Figure 3.8, a magnetic circuit can be derived that emulates the stator slotting as shown in Figure 3.9. In turn, a periodic, position (x) dependent air gap function considering stator slotting only, can be derived and this is given in (3.27).

$$g_s(x) = \begin{cases} 0, & 0 < x < x_1 \\ \Pi_{s1} || (\Pi_{s2} + \Pi_{s22}), & x_1 < x < x_2 \\ \Pi_{s1} || \Pi_{s2}, & x_2 < x < x_3 \\ (\Pi_{s1} + \Pi_{s11}) || \Pi_{s2}, & x_3 < x < x_4 \\ 0, & x_4 < x < x_5 \end{cases} \tag{3.27}$$

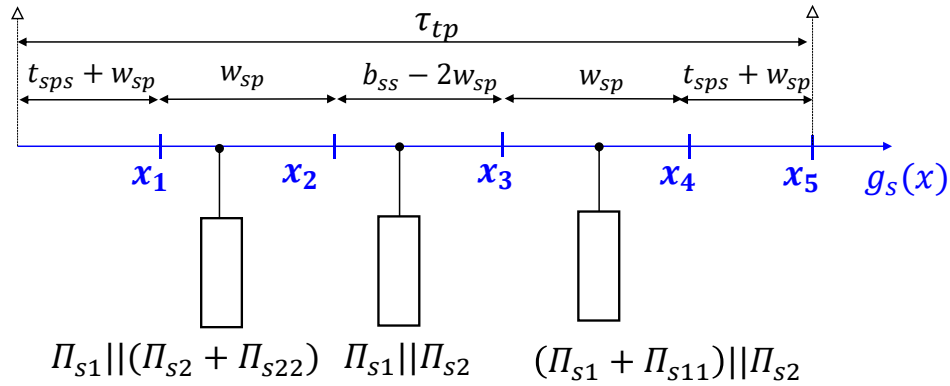


Figure 3.9. Magnetic circuit considering stator slotting.

3.3.1 Magnetizing coefficients and saliency ratio:

The general periodic expression of an air gap function considering both rotor and stator slotting can be derived based on (3.21), (3.24), and (3.27). Hence, the

total air path thickness for a salient pole rotor considering stator slotting can be derived as given in (3.28) and (3.29), where g is the air gap thickness between rotor and stator.

$$g_d(x) = g_{rd}(x) + g_s(x) + g \quad (3.28)$$

$$g_q(x) = g_{rq}(x) + g_s(x) + g \quad (3.29)$$

From (3.2) and (3.3), further expansion can be done with the aid of a Fourier series. The magnitudes of the fundamentals $d - q$ excited flux densities can then be described by (3.30) and (3.31):

$$B_{1d} = \frac{4\mu_0 F_{1d}}{\tau} \int_0^{\tau/2} \frac{1}{g_d(x)} \cos^2 \frac{\pi x}{\tau} dx \quad (3.30)$$

$$B_{1q} = \frac{4\mu_0 F_{1q}}{\tau} \int_0^{\tau/2} \frac{1}{g_q(x)} \sin^2 \frac{\pi x}{\tau} dx \quad (3.31)$$

The magnetizing coefficients of (3.5) and (3.6) can then be simplified. The simplified coefficients K_{dm} and K_{qm} can be described by (3.32) and (3.33), where $g(x)$ is an air gap function for a non-salient rotor with a constant air gap, such as $g(x) = g$ and τ is the pole pitch.

The parameters $g_d(x)$ and $g_q(x)$ are the air gap functions with respect to direct and quadrature axes excitations of the rotor derived in (3.28), (3.29).

$$K_{dm} = \frac{4}{\tau} \int_0^{\tau/2} \frac{g(x)}{g_d(x)} \cos^2 \left(\frac{\pi x}{\tau} \right) dx \quad (3.32)$$

$$K_{qm} = \frac{4}{\tau} \int_0^{\tau/2} \frac{g(x)}{g_q(x)} \cos^2 \left(\frac{\pi x}{\tau} \right) dx \quad (3.33)$$

Table 3.1. Slot opening parameters

Symbol	Parameter	Quantity
b_{ss}	Slot opening	3 mm
h_{s1}	Slot opening height	1 mm
h_{s2}	Wedge height	1 mm

Table 3.2. Rotor geometry considerations

Symbol	Parameter	Quantity
k	Number of barriers	4, 10
k_{air}	Insulation ratio	0.43
$\Delta\alpha_1 = \Delta\alpha_2 \dots = \Delta\alpha_{10}$	Per unit inner span of the barriers	$0.8/k$

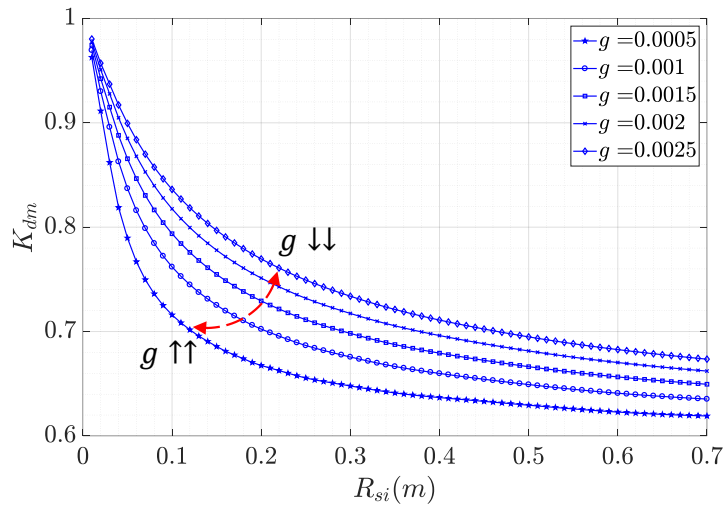


Figure 3.10. Magnetizing coefficient K_{dm} as a function of geometrical parameters: g is an air gap length, and R_{si} is the stator inner radius, both expressed in m .

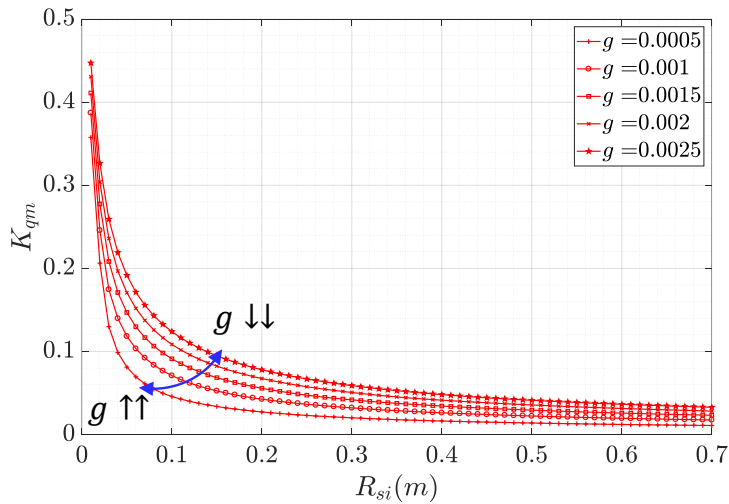


Figure 3.11. Magnetizing coefficient K_{qm} as a function of geometrical parameters: g is an air gap length, and R_{si} is the stator inner radius, both expressed in m .

Using equations (3.32) and (3.33), then various values of rotor diameters and air gap lengths can be investigated. This study is done on a machine geometry that is defined by the values given in Table 3.1 and Table 3.2. Figure 3.10 and Figure 3.11 show the estimated values of K_{dm} and K_{qm} when both stator and rotor slotting are considered.

As can be observed from Figure 3.10 and Figure 3.11, for small values of the ratio R_{si}/g , the behaviour of K_{dm} differs from K_{qm} . The latter increases significantly with the decrease of R_{si}/g , compared to g . In general, the air gap value is limited by mechanical constraints, therefore using (13), the rotor radius has to be sufficiently big relative to the air gap in order to achieve designed values of saliency and torque.

K_{dm}/K_{qm} represents an unsaturated value for magnetizing ratio and in the case when the machine has a minimum of leakage flux the ratio can be approximated to a saliency ratio.

The results based on Figure 3.10 and Figure 3.11 are plotted in Figure 3.12 according to the rotor dimensions from Figure 3.4. It can be concluded that the saliency ratio has a dependency on R_{si}/g . Therefore, it needs to be properly predefined according to the torque requirements (3.13). However, air gap function approach can be used to estimate K_{dm} and K_{qm} , hence the saliency ratio.

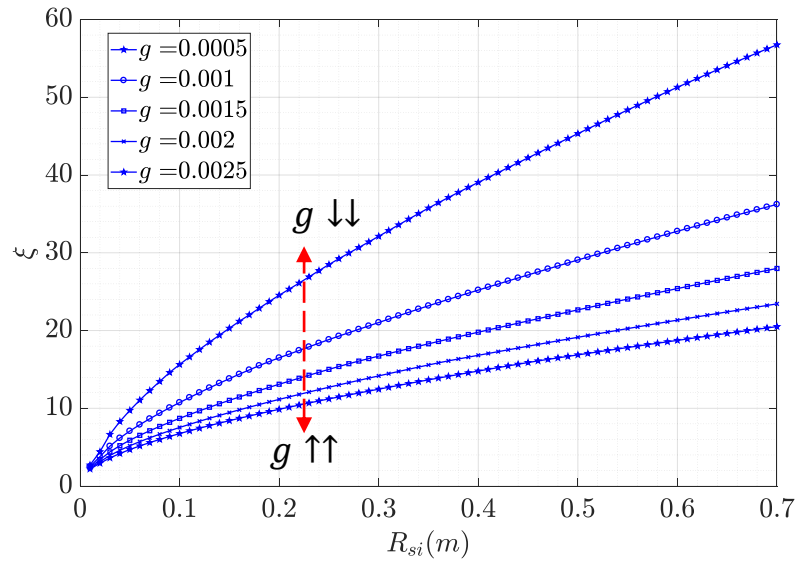


Figure 3.12. Unsaturated saliency ratio and neglected leakage ξ for various R_{si}/g combination

3.4 Saliency ratio considering saturation:

As it was concluded in the previous section, the unsaturated saliency ratio is a pure geometrical parameter. However, d - q axes inductances are not constant for different values of stator current due to the nonlinear magnetic property of the stator and rotor iron, hence the saliency ratio will change as well.

3.4.1 Simplified magnetic circuit:

A common way to express magnetic saturation is to derive a saturation coefficient. Such a saturation coefficient can be defined as a ratio of the fundamental of total mmfs of the magnetic circuit and the fundamental of the air gap mmf [48], [84]. Figure 3.14

Using the flux paths schematic of Figure 3.10, the magnetic circuit can be derived as shown in Figure 3.14. The four main reluctances are R_{t2} and R_{t1} which are tooth iron reluctances and R_{sc} and R_r which are the stator and rotor core iron reluctances respectively. R_g is the air gap reluctance. The stator iron reluctances can be derived based on the stator geometry [48]. The rotor reluctance should consider the current excitation angle, in a similar manner as it was discussed in Figure 3.6. However, the iron reluctance is now considered. As the rotor's saturation level will fully depend on the current vector angle α^e , then R_r is a function of α^e .

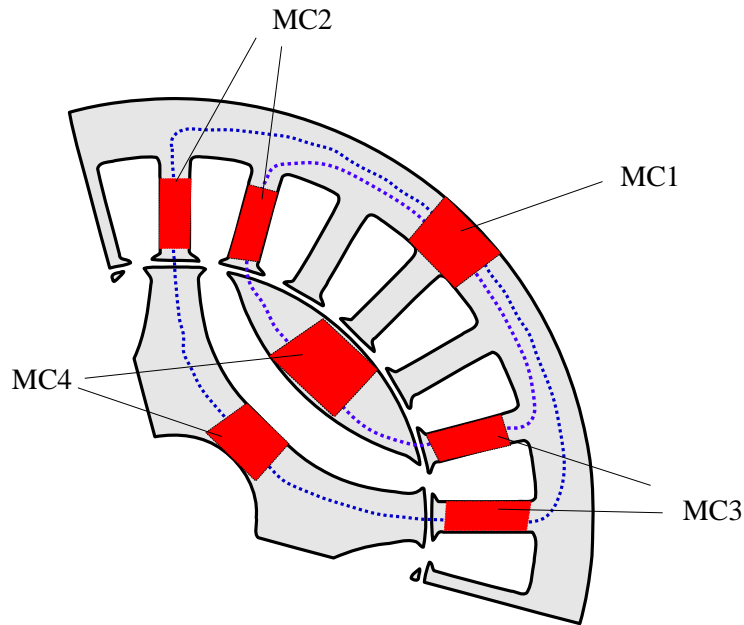


Figure 3.13. Magnetic circuit with the highlighted segments subject to saturation for d -axis.

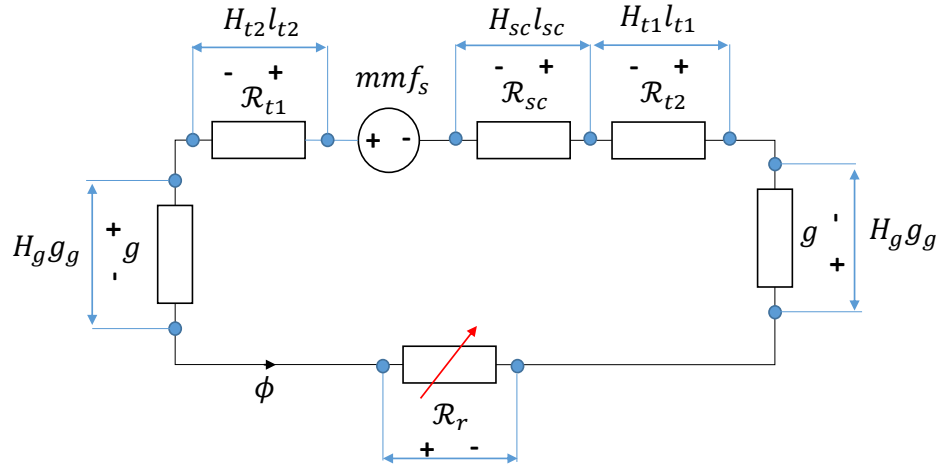


Figure 3.14. Simplified magnetic circuit of one pole.

$$\alpha^e = \tan^{-1} \frac{I_q}{I_d} \quad (3.34)$$

Using equations (3.22) and (3.23) the flux paths of rotor iron and rotor air insulation can be derived as functions of α^e , as shown in (3.35) and (3.36), where R_{ro} and R_{sh} are the rotor and shaft radiuses:

$$\Gamma_{iron} = \frac{(R_{ro} - R_{sh})\pi}{2} (1 - k_{air}) \cos(\alpha^e) \quad (3.35)$$

$$\Gamma_{air} = \frac{(R_{ro} - R_{sh})\pi}{2} k_{air} \sin(\alpha^e) \quad (3.36)$$

Hence, the rotor equivalent reluctance will be derived as given by (3.37), where A_r is the average cross sectional area of a single rotor pole:

$$\mathcal{R}_r = \frac{\Gamma_{iron}}{\mu_r A_r} + \frac{\Gamma_{air}}{\mu_0 A_r} \quad (3.37)$$

Since the insulation barriers have a high reluctance, the flux that is flowing through the circuit, shown in Figure 3.14, will be reduced. This can be approximated as (3.38):

$$\phi = \frac{mmf_s}{\mathcal{R}_{sc} + 2\mathcal{R}_g + \mathcal{R}_{t1} + \mathcal{R}_{t2} + \mathcal{R}_{ra} + \mathcal{R}_{ri}} \quad (3.38)$$

The flux equation can be modified depending on the current vector angle α^e such as described in (3.39):

$$\phi_{\alpha^e=0} \sim \frac{mmf_s}{\mathcal{R}_{sc} + 2\mathcal{R}_g + \mathcal{R}_{t1} + \mathcal{R}_{t2} + \mathcal{R}_{ri}} \quad (3.39)$$

$$\phi_{0 < \alpha^e < 90} \sim \frac{mmf_s}{\mathcal{R}_{sc} + 2\mathcal{R}_g + \mathcal{R}_{t1} + \mathcal{R}_{t2} + \mathcal{R}_{ra} + \mathcal{R}_{ri}}$$

$$\phi_{\alpha^e = 90} \sim \frac{mmf_s}{\mathcal{R}_{ra}} \sim 0$$

When $\alpha^e=0$, the flux will not pass through the insulation barriers. If $0 < \alpha^e < 90$, the circuit will present an extra reluctance component, since flux will now pass through the insulation barriers. Hence, the flux will decrease, as it is inversely proportional to Γ_{air} (3.36). When $\alpha^e=90$, it can be said that $\phi=0$, due to high reluctance of the barriers.

$$\phi \propto \mathcal{R}_r(\alpha^e, k_{air}) \quad (3.40)$$

Based on the circuit presented the Figure 3.14, the total mmf can be derived by the relationship (3.41), where l_{t1} , l_{t2} and A_{t1} , A_{t2} are teeth flux path lengths and average tooth cross sectional areas; l_{cs} is the flux path length through the stator core and A_c is the average cross sectional area of the stator core, g – air gap length and A_g is the average cross sectional area at the air gap. \mathcal{R}_r can be derived as presented in equations (3.35) - (3.37):

$$mmf_s = \phi \left(\frac{l_{t1}}{A_{t1}\mu_r} + \frac{l_{t2}}{A_{t2}\mu_r} + \frac{l_{cs}}{A_c\mu_r} + \frac{2g}{A_g\mu_0} + \mathcal{R}_r \right) \quad (3.41)$$

Based on all the above the saturation levels will depend on the insulation ratio and current vector angle.

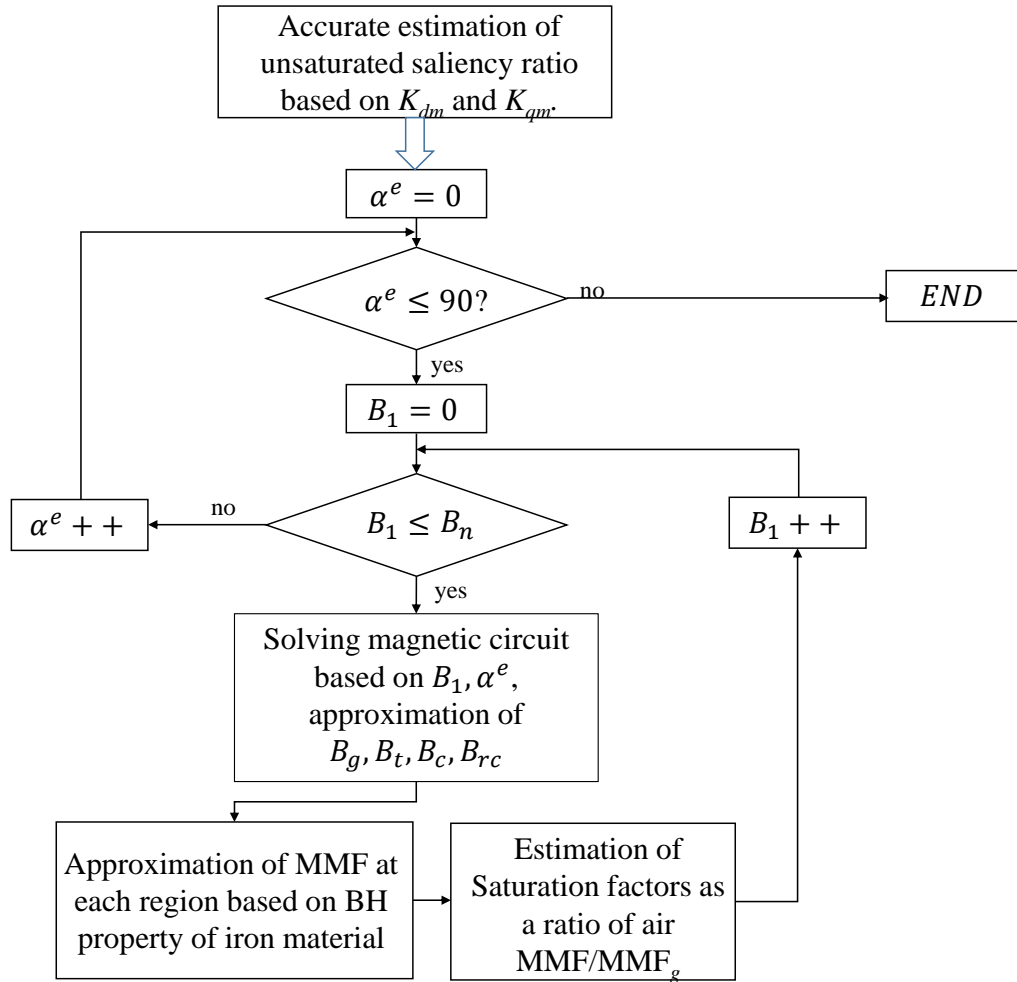


Figure 3.15. Flow Chart of saturation modelling.

Table 3.3. Highlighted B-H curve points of M530-65A iron

H(Amp/m)	0	138.1	302	2384	9134	49400	156900
B(T)	0	0.9897	1.336	1.581	1.783	1.957	2.114

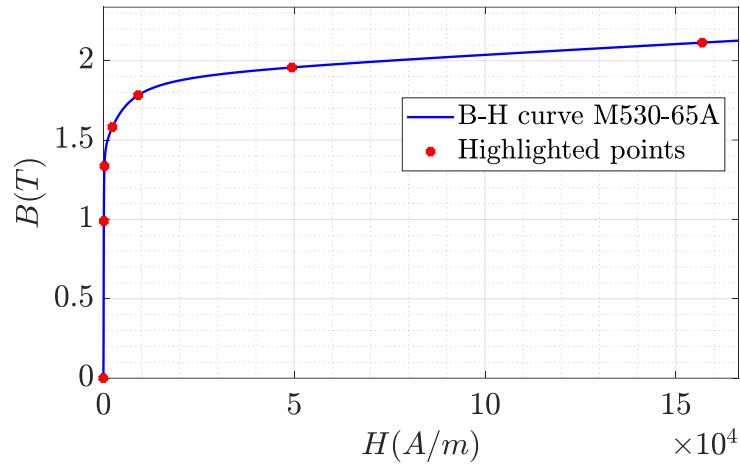


Figure 3.16. M530-65A iron B-H curve with highlighted points.

3.4.2 The principle of saturation modelling:

The saturation model is built, based on the air gap flux density as it is discussed in [48]. However, it has to be modified considering the magnetizing coefficients K_{dm} and K_{qm} (3.31), (3.32), which quantify the magnetic conductivity of d and q axis. Therefore, the air gap flux density for a given MMF will vary according to the current vector angle α^e as described in (3.42), where B_g is fundamental of the air gap flux density of a SynRel machine and based on B_1 which is the fundamental component of the air-gap flux density for a uniform air-gap machine (no saliency).

$$B_g = B_1(K_{dm} \cos(\alpha^e) + K_{qm} \sin(\alpha^e)) \quad (3.42)$$

In order to model the effect of saturation the B-H property of the iron material should be used - to determine required mmf for calculated flux density levels. Figure 3.15 presents a simple flow chart to determine the saturation levels for a designed machine.

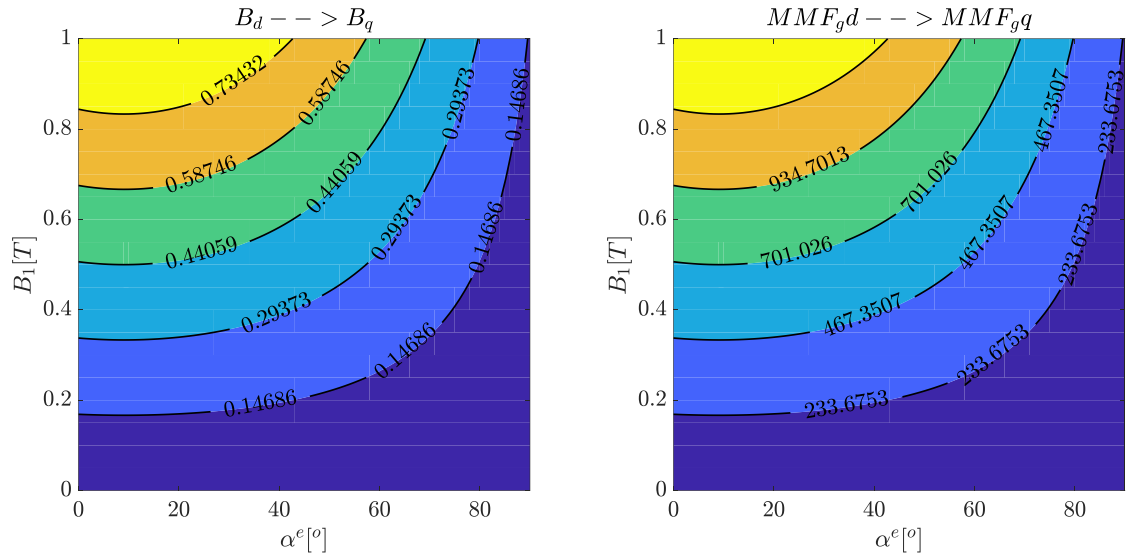


Figure 3.17. SynRel air gap flux density and MMF levels.

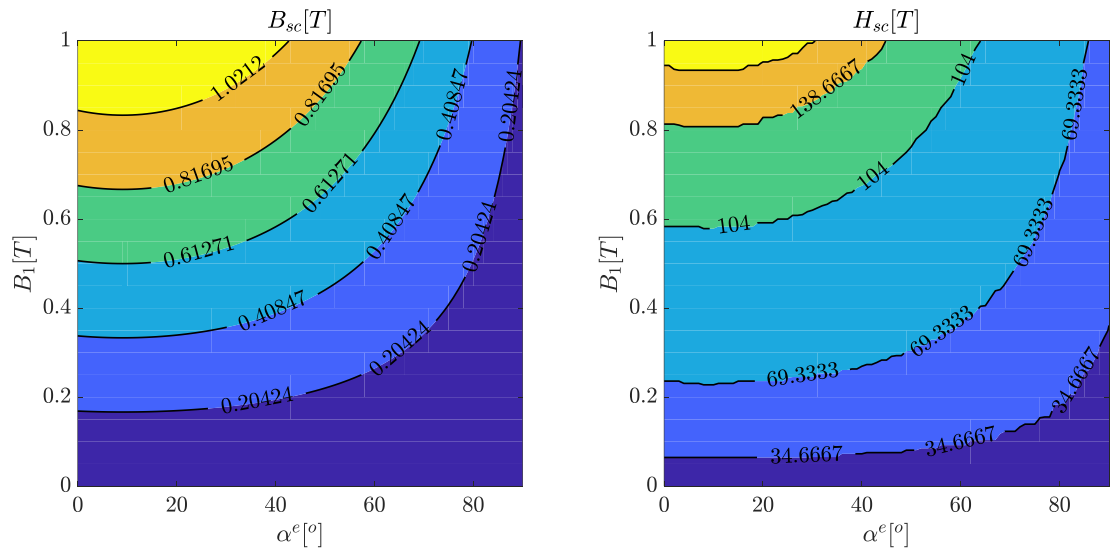


Figure 3.18. Stator back iron flux density and magnetic field strength levels.

Figure 3.17 presents air gap flux density and air gap mmf for a typical $K_{dm}=0.86$, $K_{qm}=0.14$. Using these flux density values for stator and rotor using approach described in Figure 3.15 can be derived. I.e. Figure 3.18, Figure 3.19 present a flux density and magnetic field strength levels for iron M530-65A (Figure 3.16), for $g=0.5mm$, $A_s = 0.00174m^2$, $A_r=0.00124m^2$, $A_c=0.005m^2$.

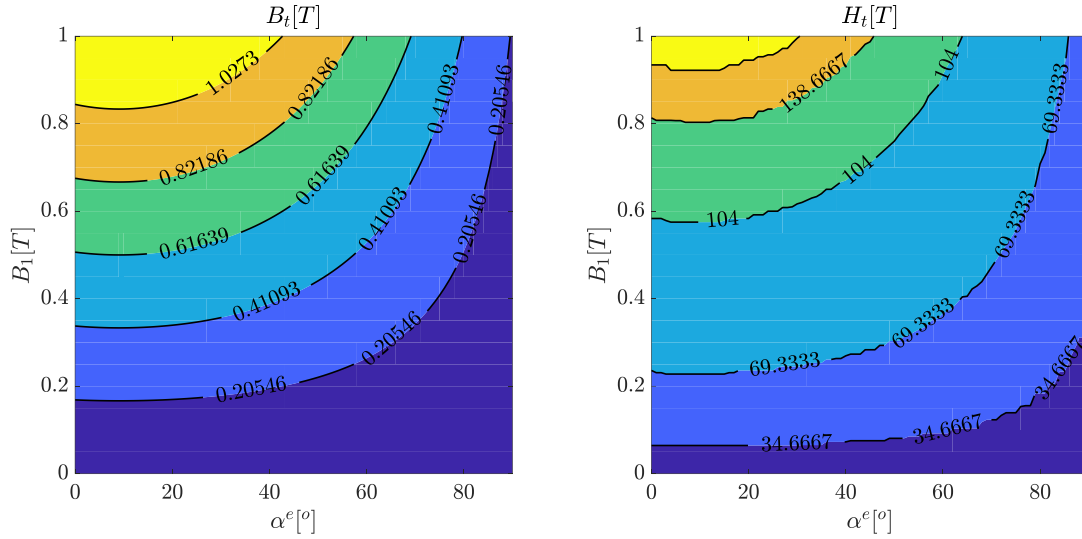


Figure 3.19. Stator tooth flux density and magnetic field strength levels.

In a similar way, the flux density and mmf can be derived for any region of a magnetic circuit Figure 3.14.

3.4.1 Saturation factors:

The saturation coefficient is defined as a ratio of the total mmf fundamental of the magnetic circuit and fundamental of the air gap mmf [48], [84].

Air gap mmfs can be derived using magnetizing coefficients (3.31) and (3.32) and the fundamental air gap flux density B_1 as (3.43) and (3.44):

$$2F_{gd} = \frac{2gB_1K_{dm}}{\mu_0} \quad (3.43)$$

$$2F_{gq} = \frac{2gB_1K_{qm}}{\mu_0} \quad (3.44)$$

Saturation coefficients K_{sd} and K_{sq} can be derived considering the magnetic circuits Figure 3.14, equations (3.9) and (3.41) for d and q axes as (3.45) – (3.46):

$$K_{sd} = \left(\frac{mmf_s}{2F_{gd}} \right) \quad (3.45)$$

$$\sim \frac{n_s I_s 3\sqrt{2}\mu_0 q K_{w1}}{\pi g 2B_1 K_{dm}} (1 - k_{air}) \cos(\alpha^e)$$

$$K_{sq} = \left(\frac{mmf_s}{2F_{gq}} \right) \quad (3.46)$$

$$\sim \frac{n_s I_s 3\sqrt{2}\mu_0 q K_{w1}}{\pi g 2B_1 K_{qm}} (1 - k_{air}) \sin(\alpha^e)$$

The magnetic circuits of d - q circuits will saturate based on the current vector angle α^e and insulation ratio k_{air} . As it is described in Figure 3.15 the B-H curve of iron material can be used to determine the magnetic field strength based on the estimated flux densities at each considered segment Figure 3.14. The mmf of each iron segment can be identified using magnetic field strength and the path length, Figure 3.15. Hence using (3.41) – (3.46), the saturated circuit can be modelled.

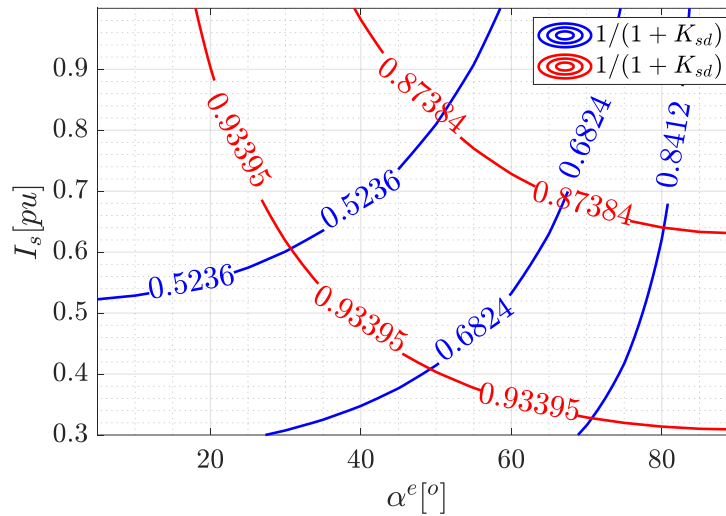
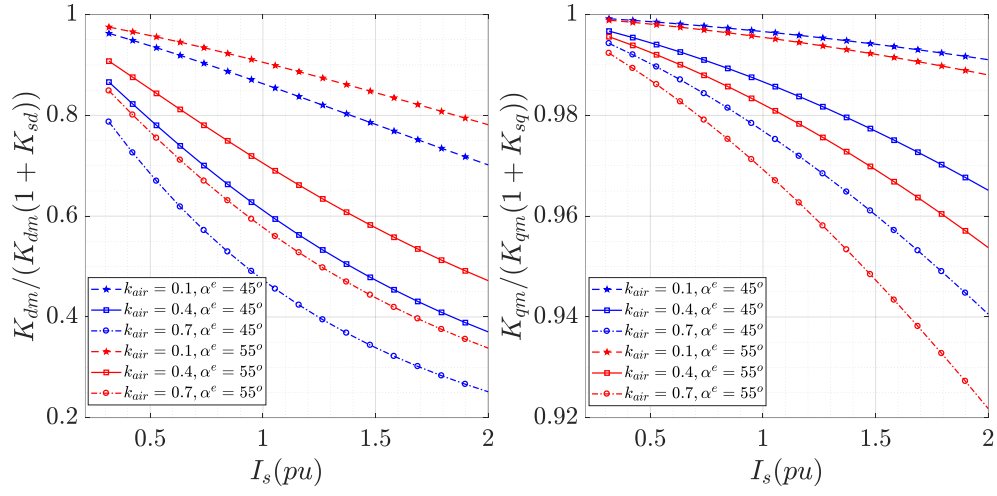
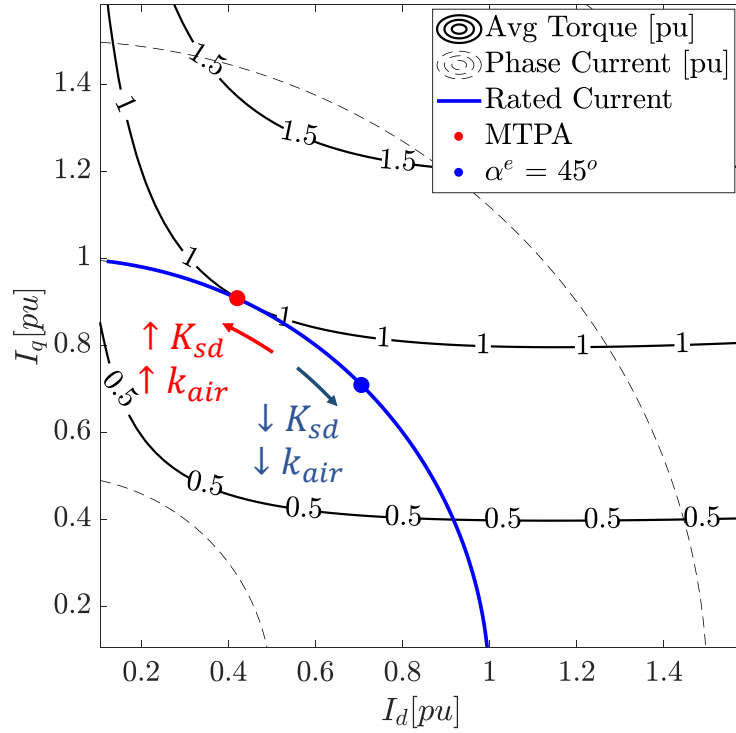


Figure 3.20. Inverse saturation coefficients as functions of I_s and α^e . $K_{dm}=0.8$, $K_{qm}=0.03$.

The accuracy of the approximation of saturation factors will depend on the number of magnetic circuit segments considered Figure 3.14 [17, 18, 19].


 Figure 3.21. d - q inductances as functions of I_s and α^e , and k_{air} .

 Figure 3.22. SynRel pu Torque profiles on I_d - I_q plane.

Using equations (3.7), (3.11), (3.32), (3.33), (3.45), (3.46) the saliency ratio considering saturation coefficients can be derived as (3.47):

$$\xi = \frac{K_{dm}(1 + K_{sd}) + K_{qm}(1 + K_{sq})}{2K_{qm}(1 + K_{sq})} \quad (3.47)$$

While d - q axis inductances can be derived using (3.6), (3.7), (3.11), (3.45), (3.46) as:

$$L_d = \frac{L_m K_{dm}}{(1 + K_{sd})} + \frac{L_m K_{qm}}{(1 + K_{sq})} \quad (3.48)$$

$$L_q = \frac{2L_m K_{qm}}{(1 + K_{sq})} \quad (3.49)$$

Figure 3.20 presents an inverse of the saturation coefficients as a functions of peak phase current I_s and current vector angle. Referring to equations (3.47) and (3.48) it can be stated that the inverse function of saturation coefficients K_{sd} and K_{sq} represent per unit values of L_d and L_q .

Figure 3.21 presents a per unit values of inductances for $k_{air}=0.1; 0.4; 0.7$, $R_{ro}=84.5\text{mm}$, $g = 0.5\text{mm}$ based on equations (3.47) – (3.48). It can be observed that higher insulation ratio k_{air} results in lower value of L_q due to reduction of K_{qm} . However, higher k_{air} will increase the d -axis saturation coefficient K_{sd} due to reduction of the iron magnetic paths. Therefore, according to equations (3.44) - (3.48) d -axis inductance tend to decrease at lower current compared to q -axis inductance due to the rotor iron saturation. As can be observed on Figure 3.21, for a typical SynRel machine when $k_{air} \sim 0.4$ the d -axis inductance is about three times the decrease of q -axis [12]. When the iron saturation occurs, the operating current vectors is achieved at higher angle α^e . Figure 3.22 presents a typical SynRel Torque profiles on I_d - I_q plane that can be derived based on (3.46), (3.47) and (3.1). As can be observed, when the machine's d -axis is saturated i.e at high k_{air} , the operating current vector (MTPA– maximum torque per ampere) is achieved at higher angle α^e , ($I_q > I_d$). And if the d -axis is unsaturated the operating current vector is at $\alpha^e = 45^\circ$.

In summary, the saturation level can be evaluated by checking if the MTPA for a rated torque value will match the typical rated current vector angle $\alpha^e \sim 60^\circ$, using the torque equation (3.1) and the updated values of L_d , L_q (3.47) - (3.48). If the value of $\alpha^e > 60^\circ$, k_{air} can be reduced. If the value of $\alpha^e \sim 45^\circ$ k_{air} can be increased as it is presented in Figure 3.22.

3.5 Preliminary model validation by means of FE:

To validate all the above, FE models are built and then used to evaluate geometries resulting from the analytical equations (3.6), (3.12), (3.13), (3.32), (3.33).

The initial parameters considered for the designs evaluation are summarized in Table 3.4 with stator and rotor dimensions based on Table 3.1 and Table 3.2 to

evaluate the model's range (relative to machine dimensions) the approach was tested for a wide range of SynRel machines. To ensure fair comparisons, all the machines were set with the same current density. This was achieved by modifying the stator slot geometry [2]. The results of this analysis are illustrated in Figure 3.23.

Table 3.4. Details of FEA validation

Symbol	Parameter	Quantity
p	Number of poles pairs	2
N	Number of slots	48
ξ	Saliency ratio initial guess	10
J	Current Density	12 A/mm ²
FEA Nodes	Average number of nodes per simulation	12000
α^e	Average current angle	~60°
g	Air gap	0.5 mm
γ	Stack aspect ratio	1
k	Number of barriers	4, 10

The black continuous line in Figure 3.23 represents an initial torque T_{init} estimation according to the size of the machine. This is achieved using equation (3.16) and a predefined saliency. Considering the air gap function, a better approximation of torque, can then be obtained T_{re} . The air gap function (3.32), (3.33) is thus used to fine-tune and update K_{dm} , K_{qm} and ξ , as according to (3.13). This is highlighted with blue and green lines for k equal to 4 and 10, respectively.

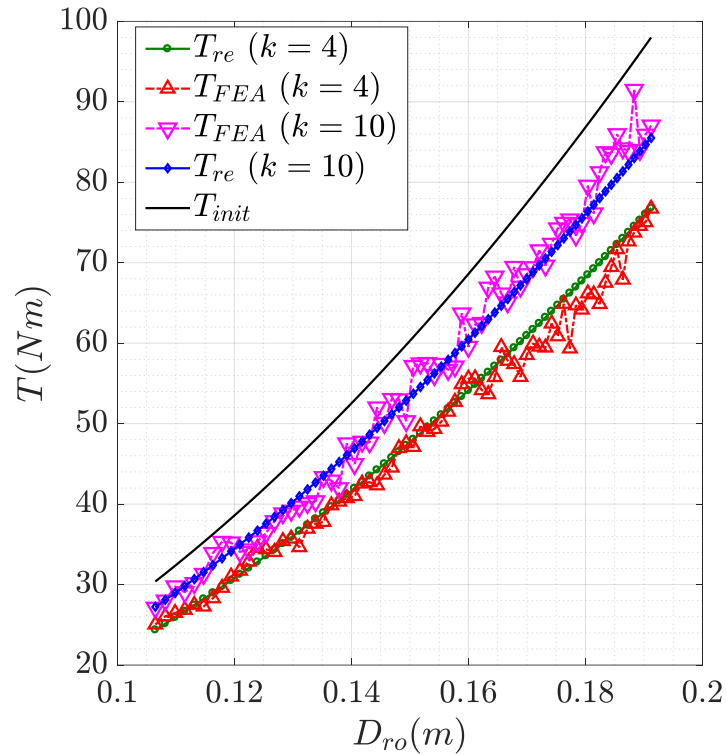


Figure 3.23. Average torque comparison, for a range of different rotor diameter: T_{re} – refined torque values using air gap function.

3.6 Conclusion:

To achieve the results shown in Figure 3.23, 140 FE simulations for two different rotor topologies were required. Figure 3.23 presents a very good correlation of a refined data with respect to the FEA simulated values T_{FEA} for a range of $0.1065m$ to $0.1912m$ rotor diameters. The average errors for T_{re} compared with T_{FEA} are $\delta_{k=4}=1.51\%$ and $\delta_{k=10}=1.92\%$. The total time for 140 FE simulations $t\sim 169$ minutes and Analytical simulations $t\sim 1.08$ minutes.

It can be concluded, that a 10-barrier geometry has higher torque capability for the same rotor size, when compared to 4-barrier geometry.

This was successfully reflected using refined values for K_{dm} , K_{qm} and ξ . All the above proves that the analytical sizing approach, based on (3.13), (3.32) and (3.33) is actually very accurate and matches significantly well with the FE results.

Chapter 4: SynRel Sizing Method

*Utilizing the analytical model presented in **Chapter 3**, a generalized sizing approach is presented in detail in **Chapter 4**. The method is flexible and can be adapted for any SynRel machine. The accuracy of the proposed model is validated, for a range of operating conditions, comparing the results with both finite element simulations and experimental measurement carried out from an existing four poles SynRel 15kW prototype.*

4.1 SynRel sizing approach:

Having confirmed the adequateness of the proposed in previous chapter analytical models, these can be used to develop a design tool for SynRel machines. A visualization of this method, presented here as a flow chart is given in Figure 4.1. The sizing process begins with a set of initial data and assignment of the key parameters. These are used in calculations of geometric, magnetic, and electric parameters in conjunction with the analytical model of the machine. In this step, the predesign output parameters are the desired rated output power, the current density as well as number of poles and slots.

- 1) The assigned parameters are the parameters that can be varied and fine-tuned. Few assumptions can be made as discussed in **Section 3.2**, referring to equation for saliency ratio estimation (3.12), which later on can be adjusted according to (3.32) – (3.33).
- 2) The main sizing step is the rotor diameter D_{ro} estimation (3.13).
- 3) Using equations (3.6) – (3.11) and the predefined saliency ratio (3.12), the main $d-q$ parameters can be estimated. At this point the number of turns for (3.7) – (3.10) and (3.12) – (3.13) is not considered. Equation (3.1) can be used for the initial torque estimation T_{init} , using predefined value of saliency.

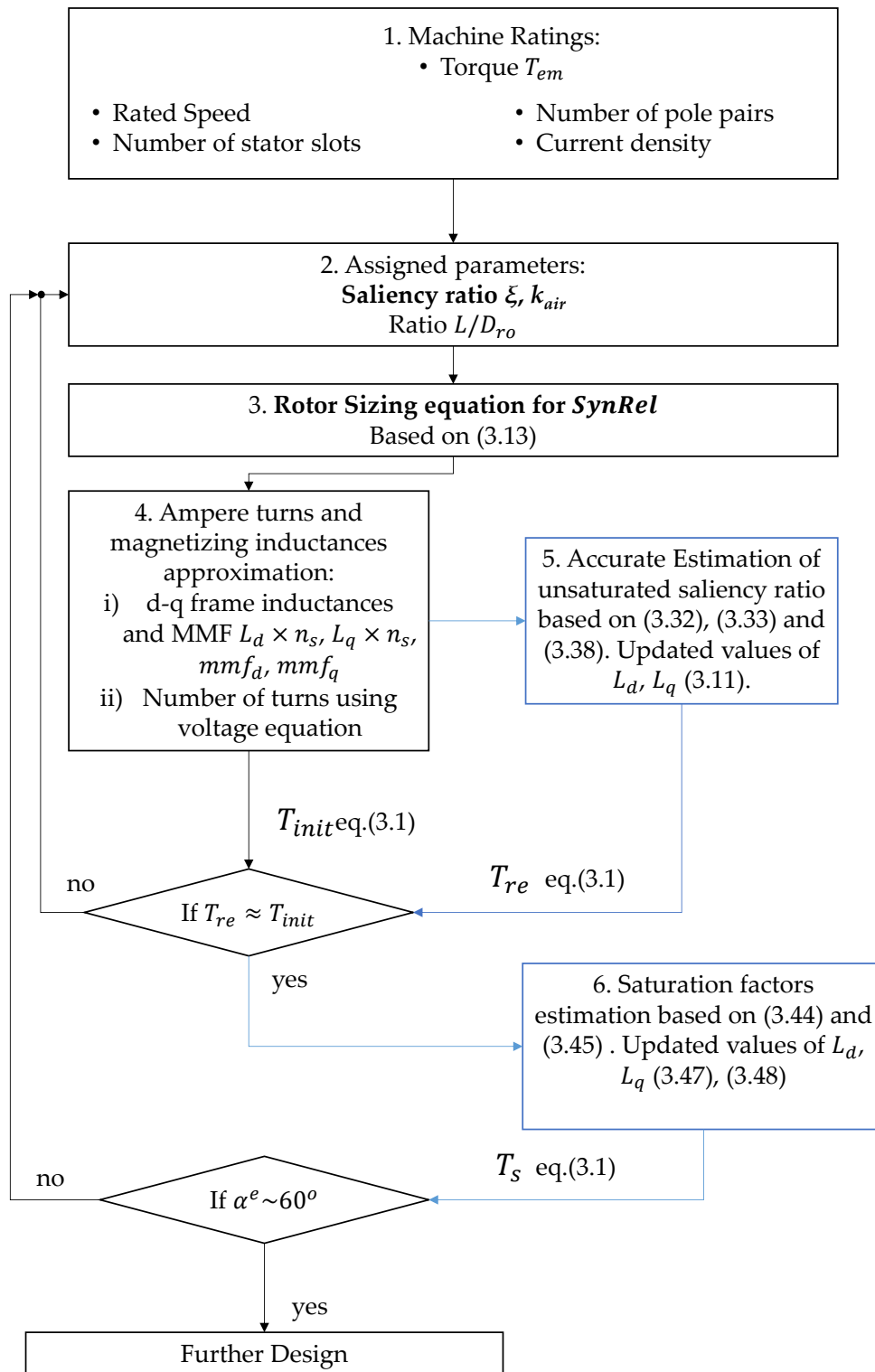


Figure 4.1 Flow chart of the analytical sizing method

- 4) The geometry of the rotor's barriers can be estimated using any preferable method [12], however the main input parameters to estimate the machine saliency should be according to Table 3.2. Considering the rotor geometry, using the method described in **Section 3.3**, (3.32) and (3.33) can be used for the estimation of the main rotor parameters K_{dm} , K_{qm} and ξ . The refined saliency ratio ξ is used to estimate an accurate torque value (3.1) T_{re} . Later, T_{re} can be compared with T_{init} . Hence, geometry should be adjusted so that $T_{re} \approx T_{init}$.
- 5) Saturation coefficients K_{sd} and K_{sq} can be derived as it is described in **Section 3.4**. Hence updated values ξ and L_d and L_q can be used to draw the Torque current profiles as it is shown on Figure 3.22. To check the saturation level a quick MTPA study can be done using the method described in **Section 3.4**.

4.2 FE Case Study:

In order to validate the proposed methodology, an existing four poles 48 slots SynRel prototype is considered as a case study. Details of the final design are presented in , with a summary of the key motor parameters. Magnetizing coefficients K_{dm} and K_{qm} were derived using (3.32), (3.33).

Table 4.1 Final parameters of tested 15kW SynRel

Symbol	Parameter	Quantity
p	Number of poles pairs	2
N	Number of slots	48
k	Number of barriers	4
k_{air}	Insulation ratio	0.43
K_{dm}	Magnetizing coefficient	0.83
K_{qm}	Magnetizing coefficient	0.032
T_{rated}	Rated Torque	95 Nm
n	Rated Speed	1500
D_{ro}	Rotor Diameter	169 mm
L_{stk}	Stack Length	205 mm

4.2.1 Inductance validation with respect to FEA results:

As a first step to validate the proposed models, the inductances of the machine are considered.

The first test was carried out at fixed $I_q=15A$, for various values of I_d . The results of this test are shown in Figure 4.2. This test is also very important as for SynRel machines, the d-axis excitation effects heavily the saturation in the machine.

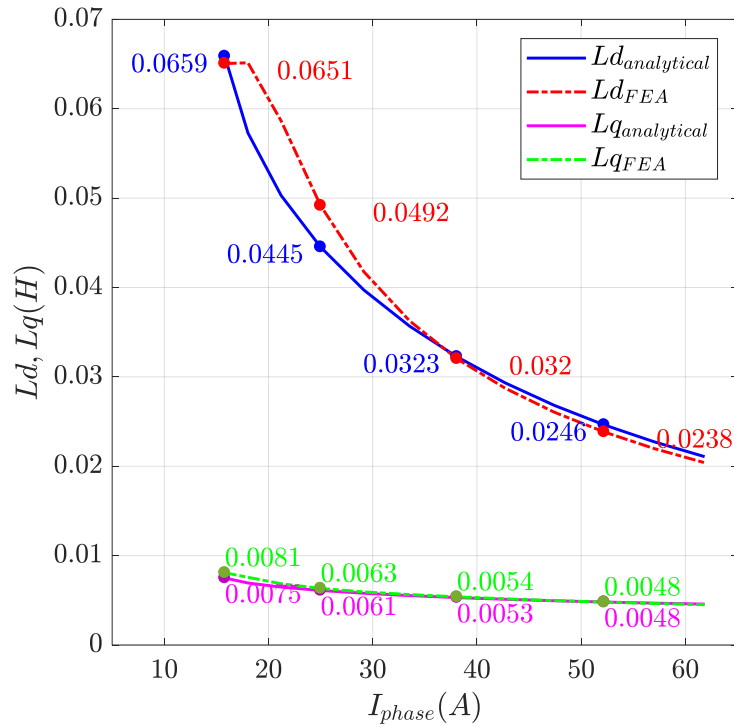


Figure 4.2. Variation of inductance with the change of I_d . With 4 highlighted data points.

As can be observed at low current values, there is a significant difference between the FEA and Analytical results. As mentioned above, this is due to dependence on saturation coefficients (44), (45); however, at higher values of current the error is reduced. At $I_m=38.08A$ the error in L_d is $\delta_{L_d}=4.35\%$, and in L_q is $\delta_{L_q}=2.23\%$.

The next step was a validation exercise for the machine having a fixed value of $I_d=15A$, for various values of I_q . In this case, it can be said that the saturation coefficient is constant due to low Permeance of the q -axis and thus the inductance values will have a small change, therefore the torque is proportionally to the current. This can all be observed in Figure 4.3 where the, analytical values of

inductances do change with the change of I_q , the excellence of the proposed model can also be observed in Figure 4.3, where the prediction error is very small for the rated I_m of 47.4A. In fact, at this rating, the L_d error is $\delta_{L_d}=1.33\%$, while the L_q error is $\delta_{L_q}=1.31\%$.

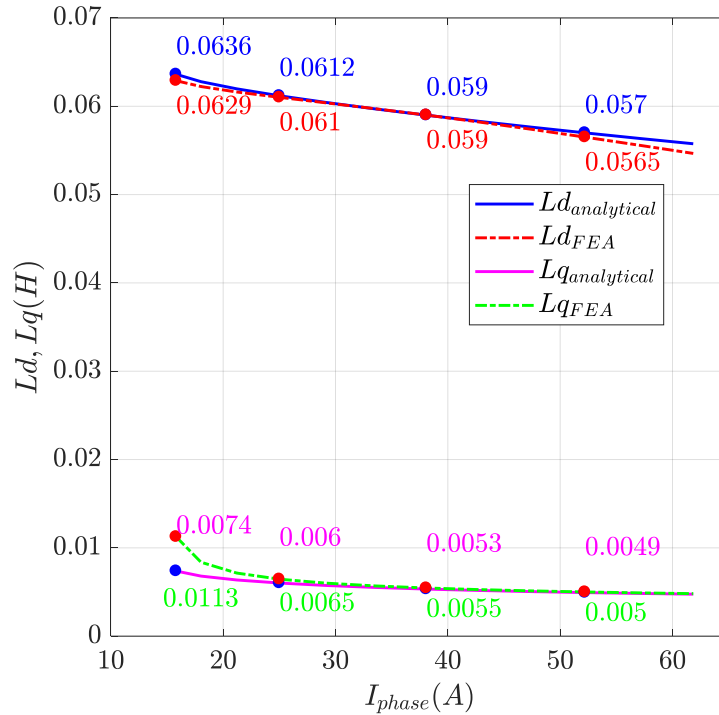


Figure 4.3. Variation of inductance with the change of I_q . With 4 highlighted data points.

4.2.2 Torque validation with respect to FEA results:

Using the equations (3.1), (3.7), (3.48), (3.49), torque can be calculated for different I_d and I_q values for a given geometry Table 4.1.

The calculation speed comparison of the modelling based on the equations (3.1), (3.7), (3.32), (3.33), (3.48), (3.49) and FEA simulations is shown in Table 4.2.

Figure 4.4 presents FEA simulated and analytically estimated torque vs current profiles. The average error of the Torque is $\delta_T \sim 6.53\%$. As mentioned previously, the accuracy of saturation factors approximation will depend on the number of magnetic circuit segments considered. In order to keep the simplicity of the approach only 4 segments of the one pole magnetic circuit were considered as it was discussed in Section 3.4. However, the methodology of the approach presented can be modified and an accurate modelling tool of SynRel machines can be derived.

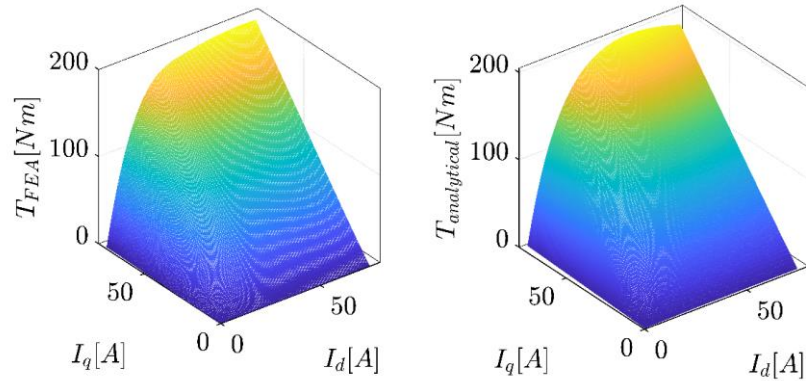


Figure 4.4. FEA vs analytical torque current profiles.

Table 4.2. Summary of FEA vs Analytical modelling.

	Number of simulations	Time	Error
FEA	25	720 sec	-
Analytical Tool	5625	2.1 sec	6.53%

4.2.3 Sizing method validation with respect to FEA results:

According to the sizing tool that was derived previously as presented on Figure 4.1, the rated saliency ratio should be accurately estimated in order to properly tune the machine geometry to satisfy the required torque.

Using equations saliency ratio can be calculated for a rated current, and torque at rated conditions can be calculated using (3.1), (3.48), (3.49) presents analytical and FEA values of saliency ratio and Torque at rated current conditions.

Analytical saliency ratio was estimated according to the magnetizing coefficients that were derived, as presented in Table 4.3. The error in saliency ratio with respect to FEA is 0.6%, while the error in torque is 1.71%. Therefore, it can be concluded that the method can accurately estimate the saliency ratio at rated conditions for the given machine size and geometry. Hence, the algorithm presented in Figure 4.1 is able to accurately size SynRel machine according to the torque requirements.

Table 4.3. Rated Saliency ratio

Symbol	Parameter	Quantity
I_d	d-axis current	24.9 A
I_q	q-axis current	40.2 A
$\xi_{analytical}$	Analytical value of saliency ratio	9.08
ξ_{FEA}	Saliency ratio (FEA simulations)	9.03
$T_{analytical}$	Torque analytical	99.1 Nm
T_{FEA}	Torque FEA	97.4 Nm

4.3 Experimental validation of the Sizing approach:

The experimental platform used to validate the proposed analytical sizing method presented is shown in Figure 4.5. On the left hand side, the SynRel prototype under test is mounted on the test rig movable base. The motor is self-ventilated through a fan mounted on the rotor shaft. A resolver is also mounted on the non-drive end of the SynRel motor, to provide the speed feedback to the drive.

Under the protection guard a torque meter is installed. The load machine on the left hand side is a 40kW induction motor, with a forced ventilation cooling system. The main results in terms of the torque performance are illustrated in Figure 4.6, which plots the produced torque on I_d - I_q plane.

As can be observed in Figure 4.6, the model results match very well with the experimental results. The errors over the low to rated current range are very small. Above the rated current value, the error increases. This error can be attributed to the uncertainty of the analytical model when it comes to saturation, as a simple 4 segment magnetic circuit was used in calculation of the saturation factors (35) - (49).



Figure 4.5. Test rig: 15kW SynRel motor (left hand side) and 40kW induction machine used as a load (right hand side).

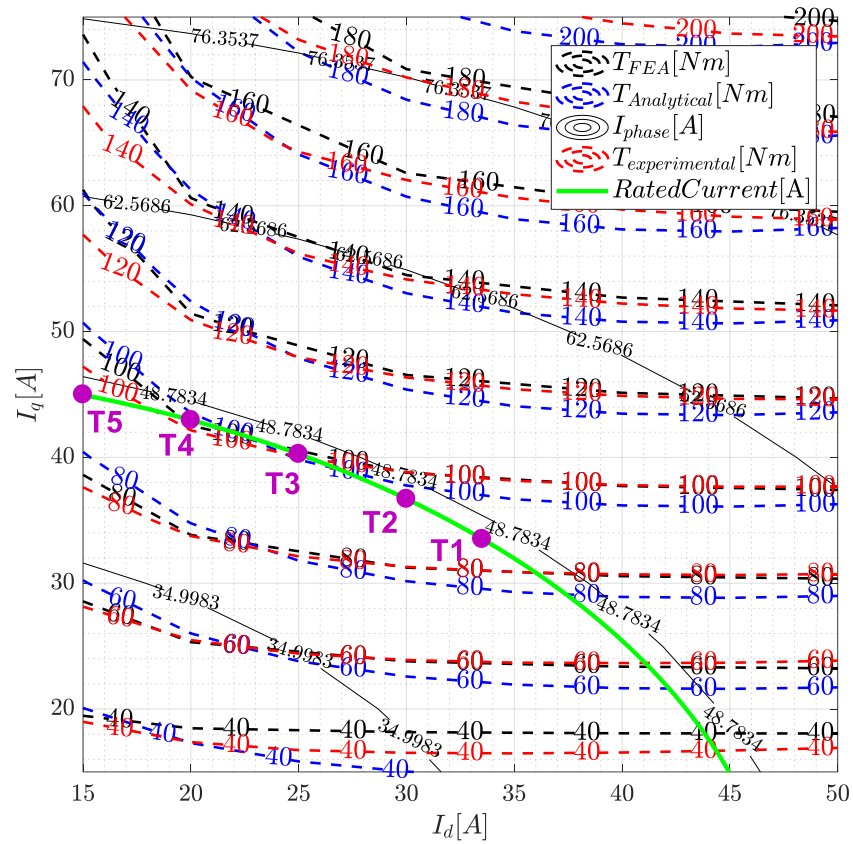
Figure 4.6. Comparison of Torque values on I_d - I_q plane.

Table 4.4. Highlighted data points, for different rated current angles.

Data points	T1	T2	T3	T4	T5
Current angle	45°	50.7°	58.2°	65°	71°
Torque analytical (Nm)	88.91	92.2	99.1	93.1	89.6
Torque Experimental (Nm)	87	89.9	98.2	96.4	95.8
Torque FEA (Nm)	86.9	90.1	97.4	95.3	94.6

Table 4.4 presents a comparison of highlighted torque points on I_d - I_q plane from Figure 4.6. As can be observed the MTPA current vector angle for the rated current is $\alpha^e=58.2^\circ$. Analytical approach is able to predict the MTPA current vector angle for the rated current. Hence it can be concluded that the approach derived in Sec. V is able to accurately estimate α^e for a rated torque.

4.4 Conclusion:

This chapter has proposed an advanced methodology for the sizing and design of SynRel machines, based on an accurate but fast analytical model. The work demonstrates the accuracy of the sizing method proposed. This has been achieved by considering saliency in preliminary sizing, which later on is fine-tuned using an air gap function approach.

The method algorithm is presented for SynRel machine sizing, suitable for both Axially Laminated and Transverse Laminated rotor topology. It is however perceived that the proposed methodology can also be adopted for simple salient pole rotor structures.

The model was validated using sets of FEA simulations as well as experimental results on a 15kW SynRel motor designed and tested. The experimental results are in line with the theoretical prediction: the analytical estimation of the average torque throughout over a wide current range is fast and accurate. At rated current, the error of analytical value is about 2.75%.

It can be concluded that this chapter is defining a fast and accurate method for the preliminary sizing of Reluctance Machines that can be adopted by the research and industrial community.

Chapter 5: A Homothetic Scaling Criteria for Synchronous Reluctance Machines Design

This chapter focuses on the detailed analytical evaluation of the magnetic behaviour of the scaled SynRel machines. The analytical model defined previously has been applied to a wide range of machines and validated through finite element analysis. Three reference machine geometries are defined, labelled as M1, M2 and M3, based on the existing designs. These have different combinations of stator and rotor geometrical parameters. Using the analytical tool, presented in previous chapter a wide range of the scaled machines of each reference geometries has been analyzed and their electromagnetic performance calculated. Finite Element (FE) simulations are used to validate the analytically calculated data and proposed theory for 9 scaled geometries, in Section IV.

5.1 Introduction:

In mathematics the homothety is a transformation of an affine space determined by a point 'O', which usually is its centre, and a nonzero coefficient of scaling [98], [99].

The concept can be simply represented as shown in Figure 5.1, where two similar figures are related by a homothetic transformation with respect to their centre O.

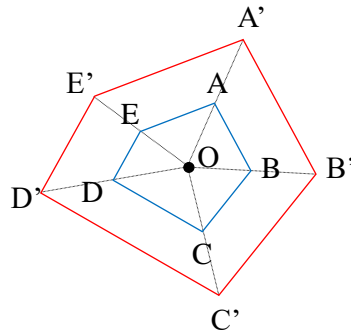


Figure 5.1. Homothety example

As discussed in [100] and [101], the main idea of homothetic scaling in machine design is to derive a scaling factor s_n for some key machine parameters. For example, the torque T_n that characterize the motor M_n in the form shown in (5.1), where T_n is a torque of an n -scaled machine, s_n is the scaling coefficient that can be derived using a regression method or using other appropriate statistical technique, R_{nro} is the rotor radius of the n -scaled machine and γ_n is the aspect ratio of M_n .

$$T_n(R_{nro}, \gamma_n) = s_n T_{ref}(R_{roref}, \gamma_{ref}) \quad (5.1)$$

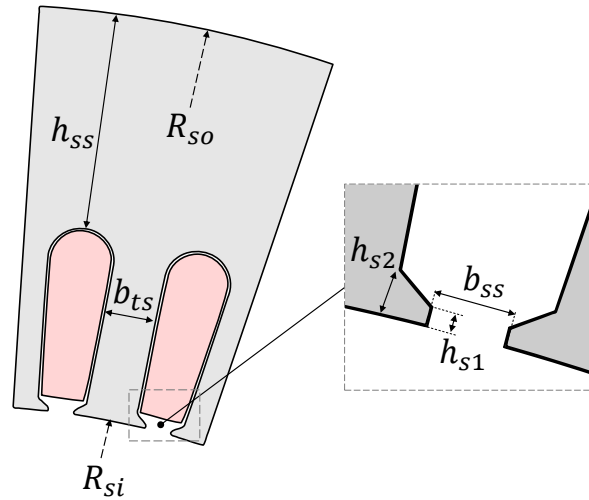


Figure 5.2. Sketch of stator geometrical parameters.

In order to derive the scaling coefficients in (25), a reference machine M_{ref} has to be radially or axially scaled, therefore varying R_{roref} and γ_{ref} , and resulting scaled geometries can be evaluated using analytical model presented previously.

5.2 Reference machines:

In this section, the three reference SynRel geometries, namely M1, M2 and M3, are defined in detail for both stator and rotor with dimensions reported in Table 5.1 and Table 5.2. These have been selected to cover different machine frames, typically in the low to medium power range. The general stator geometry for the reference motors is shown in Figure 5.3.

Table 5.1. Reference machines' main dimensions

Symbol	Parameter	Quantity		
		M1	M2	M3
N_s	Number of slots	48	48	72
R_{so}	Stator outer radius	200 mm	130 mm	260 mm
R_{si}	Stator inner radius	130 mm	85 mm	175 mm
g	Air gap thickness	1 mm	0.5 mm	1.1 mm
R_{ro}	Rotor outer radius	129 mm	84.5 mm	173.9 mm
h_{ss}	Stator Back iron	37.9 mm	22.8 mm	42.6 mm

b_{ts}	Stator Tooth width	9.3 mm	5.16 mm	7.1 mm
b_{ss}	Stator Slot opening	4 mm	3.5 mm	4.2 mm
h_{s1}	Stator Slot opening height	1 mm	0.8 mm	1.5 mm
h_{s2}	Wedge height	1.4 mm	1.6 mm	2.65 mm
L_{stk}	Stack Length	205 mm	240 mm	390 mm

Table 5.2. Reference rotors dimensions

Symbol	Parameter	Quantity		
		M1	M2	M3
k	Number of barriers	3	4	3
$\Delta\alpha_1$	Angular bar 1 span	14.59°	10.91°	12.39°
$\Delta\alpha_2$	Angular bar 2 span	14.28°	9.24°	14.77°
$\Delta\alpha_3$	Angular bar 3 span	11.52°	9.68°	12.28°
$\Delta\alpha_4$	Angular bar 4 span	-	10.09°	-
k_{air}	Insulation ratio	0.37	0.473	0.465

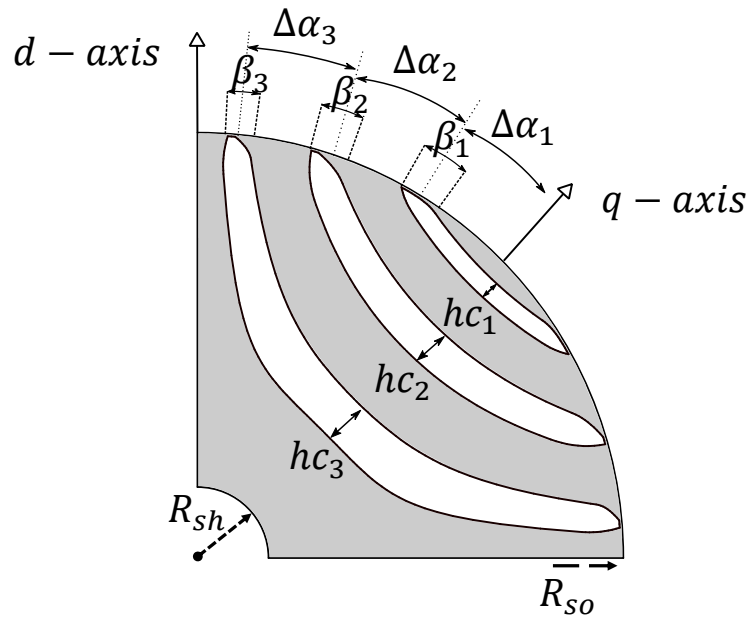


Figure 5.3. Quarter of geometry for anisotropic type rotor with 3 – barriers and 4-pole configuration. Based on $\Delta\alpha_k$ (per unit value of α) and hc_k (per unit value of barrier thickness).

Through the geometrical parameters shown in Figure 5.3 a comprehensive parametrization of the flux barriers can be achieved [102], [19].

These are drawn using the Joukowski air-flow potential equation [103], . All the rotor parameters of interest are highlighted in Figure 5.3. The total insulation ratio k_{air} can be derived as an average value of hc_k as described in [103]. The rotor barriers geometrical parameters, for the reference machines, are reported in Table 5.2.

5.3 Radial scaling assumptions:

Using the reference geometries presented in Figure 5.2 and Figure 5.3 the appropriate geometrical scaling procedure should be defined. For the further performance evaluation, the air gap will be kept constant, i.e. for M1 $g=1mm$, therefore for any M1 scaled geometry the air gap will be the same. The geometry scaling coefficients are defined as shown in equations (5.2) and (5.3), where R_{si-ref} and R_{si-n} are the stator inner diameters of the reference machines and the scaled machines, respectively. Also, S_{si} and S_{ro} are the scaling coefficients for any stator and any rotor geometrical parameter, respectively.:

$$S_{si} = \frac{R_{si-n}}{R_{si-ref}} \quad (5.2)$$

$$S_{ro} = \frac{R_{si-n} - g}{R_{si-ref} - g} \quad (5.3)$$

The angular parameters, such as angular barriers span are kept constant for any derived geometry, therefore they are not subject of scaling.

5.4 Effect of scaling on magnetizing coefficients:

To study the effect of scaling on K_{dm} , K_{qm} , consider the reference geometries M1, M2 and M3. Starting from these a range of geometries has been scaled according to the rules described by (5.2) and (5.3).

As can be observed from Figure 5.4, both K_{dm} and K_{qm} decrease with the stator inner radius. However, the behavior of K_{qm} differs from K_{dm} significantly with the decrease R_{si} , i.e as shown on Figure 5.4 for M2 K_{dm} and K_{qm} drop by ~24% and ~71% respectively. As presented in Table 5.2, k_{air} for M1 is significantly lower compared to M2, which results in higher magnetizing coefficient as the air paths length are decreased (3.22) - (3.23).

In summary the magnetizing coefficients tend to decrease with the stator inner diameter at fixed air gap. As the K_{dm} and K_{qm} change at different rate with respect to R_{si} , it can be said that smaller R_{si} will have lower saliency and hence lower torque

capability. Using the magnetizing coefficients calculated above, the saturation model can be derived, which will be discussed in the following subsection.

Considering (3.32) - (3.33), the magnetizing coefficients do not depend on the radial scaling. However, the inductances (3.7) will proportionally change with respect to axial scaling, therefore the torque is changed as well (3.1).

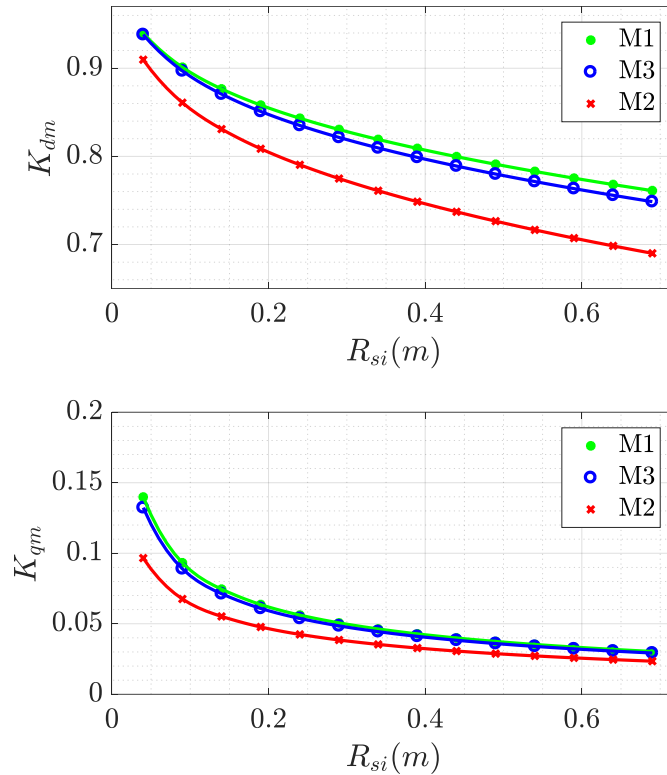


Figure 5.4. Magnetizing coefficient K_{dm} and K_{qm} as a function of stator inner radius for M1, M2 and M3 geometries.

5.5 Effect of scaling on saturation:

To evaluate the effect of scaling on saturation levels the reference geometries M1, M2 and M3 will be considered in the following analysis. For the modelling example the BH property of the silicon iron M270-50A was used. Figure 5.5 presents the modelled air gap flux densities B_{dq} and corresponding mmf_{s1} of the magnetic circuit (Figure 3.14) of M1, M2 and M3 on the fundamental air gap flux density of a nonsalient rotor B_1 and stator inner radius R_{si} plane. The air gap flux density was modelled for a wide range of scaled geometries using equation (3.42). The flux densities levels were calculated based on the previously derived magnetizing coefficients Figure 5.4.

Figure 5.5 a) is showing the lower air gap flux density B_{dq} levels for M1, M2 and M3, while Figure 5.5 b) is the corresponding fundamental mmf_{s1} levels of the magnetic circuit at $\alpha^e=45^\circ$. In c) and d) the higher air gap flux densities and fundamental mmf_{s1} levels at $\alpha^e=45^\circ$ are highlighted, while and e) and f) are the higher air gap flux densities and mmf_{s1} levels at $\alpha^e=60^\circ$.

As can be observed, the smaller geometries have a higher magnetic conductivity due to greater values of K_{dm} and K_{qm} . Therefore, the corresponding air gap flux densities and magneto motive forces levels are higher. However, the values do not vary significantly with respect to R_{si} . In addition, it can be noted that M1 has higher values of mmf_{s1} for the corresponding flux levels, which is reflected by higher values of magnetizing coefficients (Figure 5.4) and lower value of k_{air} . This leads to a much higher magnetic conductivity for both d and q axes as the rotor reluctance is reduced (3.35) - (3.37).

At higher B_1 levels the corresponding B_{dq} flux densities and fundamental mmf_{s1} will drop if the current angle is increased as shown Figure 5.5 e) and f). As can be noted the mmf_{s1} levels do not vary significantly with the increase of R_{si} , hence, it can be concluded that the saturation levels do not vary as well.

Considering the axial scaling, the saturation patterns will not change. As the geometry of the rotor and stator will change in axial direction, therefore the conductor length and main reluctances, (3.35) - (3.37) will vary proportionally, whereas the flux density levels will remain unchanged.

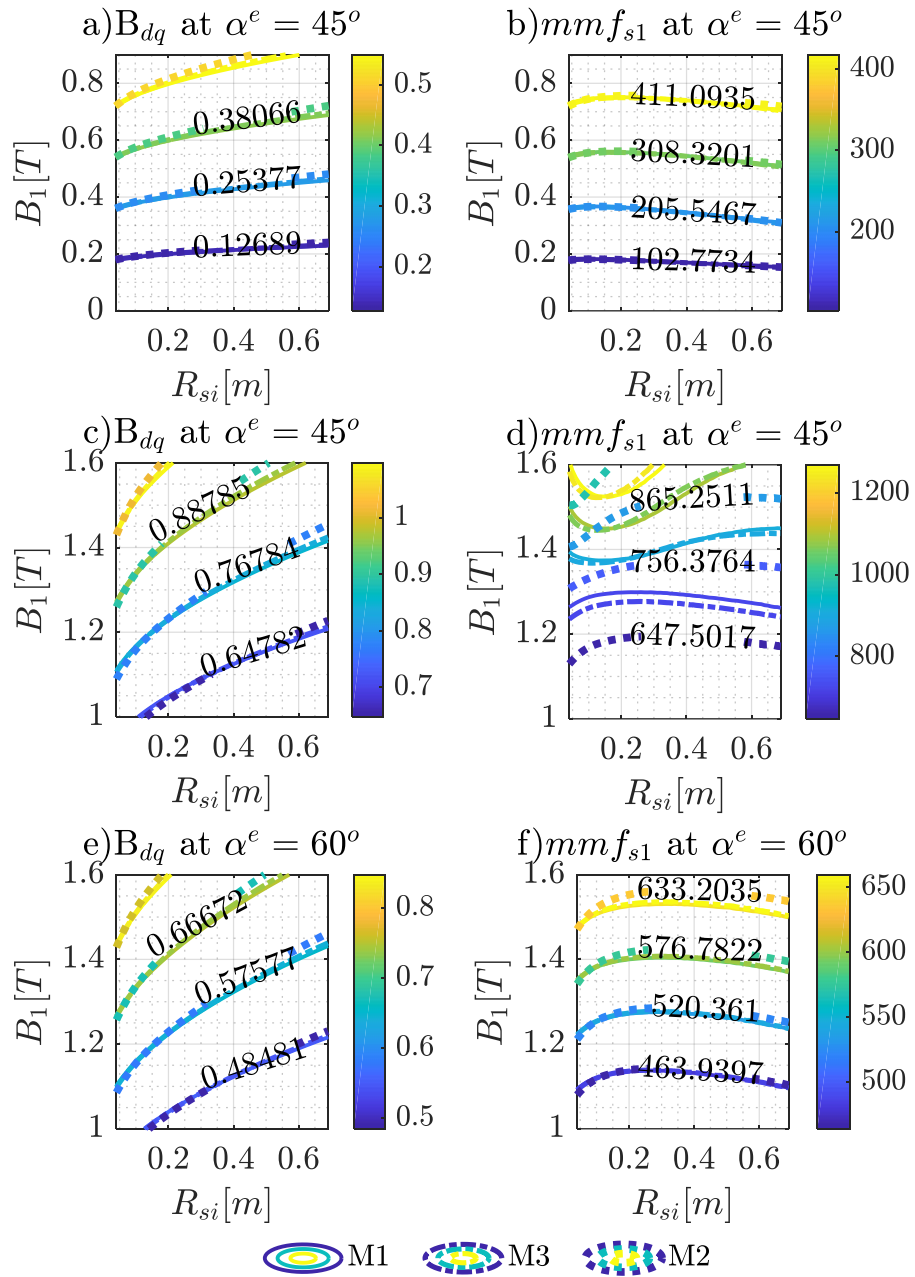


Figure 5.5. Analytical model outputs: air gap flux densities and fundamental magneto motive forces for M1, M2 and M3 based on the scaled magnetizing coefficients.

5.6 Effect of MTPA for the M2 scaled geometries:

The MTPA behavior of the scaled SynRel will be evaluated on the M2 geometry as a case study in both axial and radial scaling. Using the modelling technique described above and the BH property of the iron material, the effect of scaling on MTPA can be evaluated.

Equation (3.1) can be used, however since at this point the number of turns is unknown the following updated equation (5.4) can be used. As can be observed in (5.4) the number of turns can be simplified, hence:

$$\begin{aligned} T_{em} &\sim 1.5p [L_{d1} \cdot (n_s)^2 - L_{q1} \cdot (n_s)^2] \cdot \frac{mmf_d}{(n_s)} \cdot \frac{mmf_q}{(n_s)} \\ &= 1.5p [L_{d1} - L_{q1}] \cdot mmf_d \cdot mmf_q \end{aligned} \quad (5.4)$$

Where mmf_d and mmf_q are the d -axis and q -axis mmfs, respectively. The main inductances values with neglected number of turns can be derived from (5.5) and (5.6) as:

$$L_{d1} = \left[\frac{K_{dm}}{(1 + K_{sd})} + \frac{K_{qm}}{(1 + K_{sq})} \right] \cdot 6\mu_0 R_{ro} L_{stk} \frac{(qK_{w1})^2}{g} \quad (5.5)$$

$$L_{q1} = \left[\frac{2K_{qm}}{(1 + K_{sq})} \right] \cdot 6\mu_0 R_{ro} L_{stk} \frac{(qK_{w1})^2}{g} \quad (5.6)$$

In equations (5.5) and (5.6), saturation factors are calculated using (3.43) - (3.46), to model the saturation, as described in Figure 3.15. The calculated values of T_{em} (5.4) can be graphed on the $mmf_d - mmf_q$ plane, as shown in Figure 5.6 a) where the per unit torque variation, for different values of mmf_{s1} , is presented for the M2 geometry. In the following parts the torque is expressed in per unit values with reference to the rated torque. This occurs at the rated current for an MTPA angle $\alpha^e=60^\circ$. For example, considering M2, for stator scaling factor $S_{si} = 1$ the MTPA $\alpha^e=60^\circ$ occurs at $mmf_{s1}=2300$. Therefore p.u. torque is for M2 can be expressed as (31):

$$T_{pu} = \frac{T(mm f_{s1}, \alpha^e)}{T(2300, 60^\circ)} \quad (5.7)$$

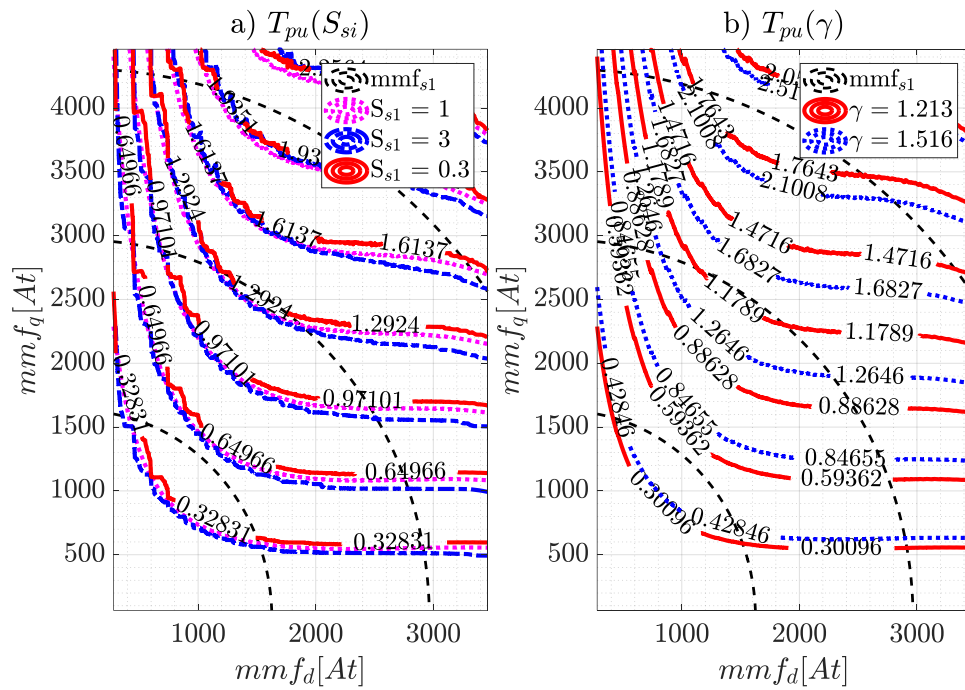


Figure 5.6. M2 geometries p.u. values of torque on mmf_d - mmf_q plane. a) radially scaled, b) axially scaled.

Figure 5.6 b) presents the comparison for axially scaled geometries. As can be observed the torque increases proportionally to the aspect ratio as the $d - q$ axes inductances (5.5) and (5.6) increase. However, the torque curves follow the same patterns.

Table 5.3. Details of FE evaluation

Symbol	Parameter	Quantity		
		M1	M2	M3
mmf_{s1}	Rated fundamental MMFs	$\sim 3200 \text{ At}$	$\sim 2350 \text{ At}$	$\sim 2900 \text{ At}$
α_i^e	Rated current vector angle		$\sim 60^\circ$	
R_{si}	Range of scaled inner stator radiuses	$40 \text{ mm} \leq R_{si} \leq 600 \text{ mm}$		
FEA Nodes	Average number of nodes per simulation	12000		

5.7 FE evaluation:

To validate the theory proposed above, a campaign of FE simulations have been carried out for a wide range of scaled geometries of M1, M2 and M3. The simulation details are summarized in Table 5.3. 9 different radially scaled machines for each reference geometry were evaluated.

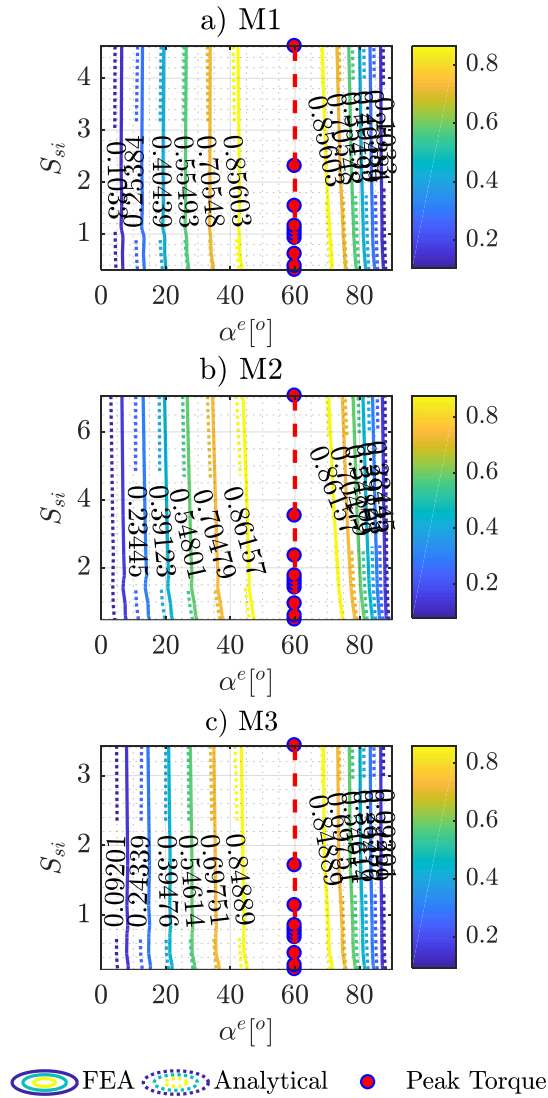


Figure 5.7 Reference geometries FE simulated and analytically calculated p.u. torque on current excitation angle α^e and scaling factor S_{si} plane, a) M1 b) M2 c) M3.

In order to carry out a fair evaluation, all geometries were scaled within a same range of stator inner diameter R_{si} , and the scaling coefficients were derived according to (5.2) and (5.3).

The FE and analytical results have been expressed in p.u. torque maps according to equation (5.4) on the $S_{si}-\alpha^e$ plane for scaled geometries M1, M2 and M3, as presented in Figure 5.7 a) b) and c), respectively.

For each reference geometry, 9 points are highlighted on each figure, which represents the peak torque of each scaled geometry simulated using FE.

As discussed previously, the MTPA angle vectors is a function of k_{air} . Therefore, the derived mmf_{s1} have different values for each considered geometry. This is due to the different k_{air} of the base machines (Table 5.2). i.e M1 will saturate at higher mmf_{s1} values than M2 as k_{air} is significantly lower.

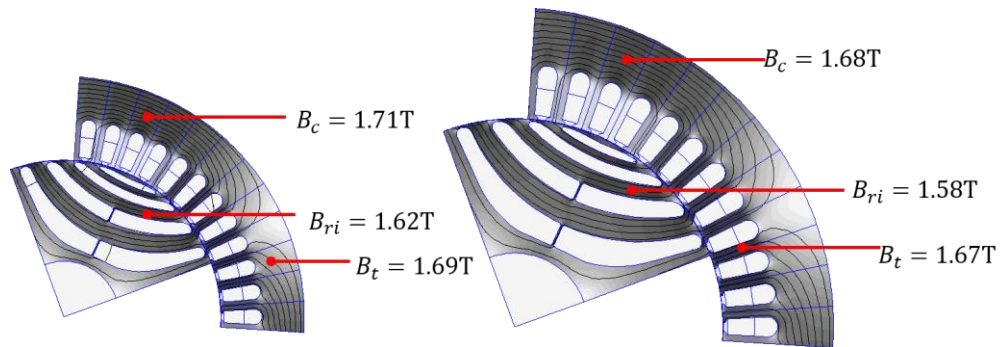


Figure 5.8. FE simulated M2 geometries. On the left $S_{si}=1.765$, and $S_{si}=2.36$ on the right with highlighted flux densities.

It can be observed that the peak p.u. torque location does not vary significantly. The scaled machines with $S_{si} < 0.5$ saturate faster but the peak torque occurs at a current vector in the range of $60^\circ < \alpha^e < 65^\circ$. This can be explained by higher values of magnetizing coefficients K_{dm} and K_{qm} , as discussed previously. Figure 5.8 shows the FE flux density plots for M2 geometries with different S_{si} , at rated ampere-turns as reported in Table 5.3 and $\alpha^e = 60^\circ$. The iron flux density values are slightly different due to the higher magnetic conductivity of a smaller geometry.

5.8 Conclusion:

Based on all the above it can be said that any scaled geometry will approximately saturate at the same values of mmf_{s1} , which will result in the same MTPA current vector for the given values of Ampere-turns, $n_s I_s$. However, the radially scaled geometries will slightly deviate with respect to magnetizing coefficient (Figure 5.4).

Chapter 6: A Generalized scaling derivation

Using the analytically calculated data, the rated torque as function of size and volume can be derived using the regression analysis, which is a set of statistical processes for estimating the relationship between variables [104]. The following derivations will be a useful tool for evaluating size and weight of the machine that can deliver the required specifications, and quickly approximate the performance of the machine.

6.1 Introduction:

The first step for a machine design is to roughly estimate the size of the main components. Usually standard text-books approach for machine sizing is used, based on the generalized torque relation for common cylindrical machines. The torque relation is derived as a function of the machine's volume and magnetic field energy in the machine's air gap [86]. Various adaptations of this sizing technique have been discussed in literature [2], [4], [85]. The most common approach is traditionally based around the relationship between the volume and the two main constraints of any machine, namely the magnetic limit and the thermal limit [88], [105], [50]. In [100], [101], the generalized scaling method based on the homothety concept was described for Induction Machines (IM). This scaling approach is another way of considering the sizing of an electrical machine. In [9], this approach was implemented for a wide range of IMs and has defined a set of generalized equations for the machine's power as a function of weight and size, using a heuristic-based statistical method. In this chapter, the homothety principle is applied to SynRel machines based on the data gathered from previous chapter.

6.2 Radial scaling function:

The power regression (PWR) technique [104], [106] was used to derive the general torque dependencies for radial scaling based on analytically calculated data. The general expression can be written as:

$$y(x) = ax^b \quad (6.1)$$

Table 6.1 presents the PWR coefficients for general sizing equation (6.1). The functions considered are the torque as a function of the stator inner radius $T(R_{si})$,

the torque as a function of the machine volume $T(V)$ and their inverse functions $R_{si}(T)$ and $V(T)$.

Table 6.1. PWR coefficients for radial scaling

PWR coeff.	M1	M2	M3
$T(R_{si})$			
<i>a</i>	21884	15554	16823
<i>b</i>	2.05532	1.9635	2.0013
$R_{si}(T)$			
<i>a</i>	0.0076	0.0071	0.007299
<i>b</i>	0.4895	0.515	0.5114
$T(V)$			
<i>a</i>	3415	2331	2631
<i>b</i>	0.6808	0.6486	0.6579
$V(T)$			
<i>a</i>	$6.092 \cdot 10^{-6}$	$6.5 \cdot 10^{-6}$	$6.311 \cdot 10^{-6}$
<i>b</i>	1.526	1.54	1.472

Figure 6.1 presents sizing curves for SynRel machines for M1, M2 and M3 geometries. The plotted lines in Figure 6.1 a) b) and c) d) represent the PWR functions, whereas the dots represent the 9 FE simulated data points. M1, M2 and M3 have different dimensions such as aspect ratios $\gamma = L/D$, and different air gap g , thus the volume and the torque varies.

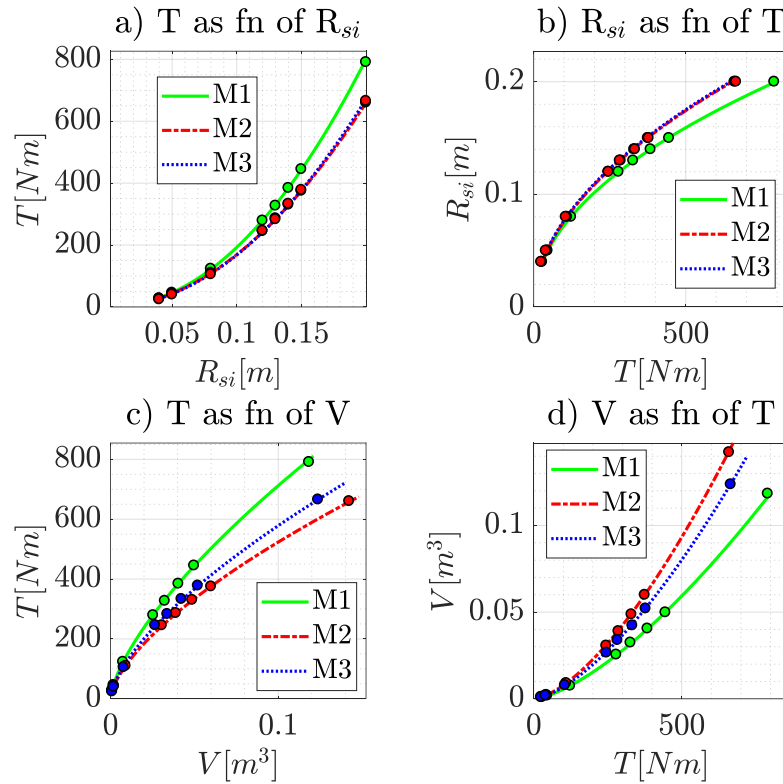


Figure 6.1. M1, M2 and M3 sizing curves.

6.3 Main sizing function:

The polynomial regression (PLR) [104], [106] can be a suitable form for a general sizing function for both radial and axial scaling, which can be described as:

$$T(R_{si}, \gamma) = p_0 + \sum_{k,j} a_k R_{si}^k + b_j \gamma^j + c_{k,j} R_{si}^k \gamma^j \quad (6.2)$$

Figure 6.2 presents a general sizing equation where the torque is shown as function of R_{si} and γ (taking M2 geometry as an example). The derived coefficients of (6.2) are provided in the Table 6.2. The equations (6.1) and (6.2), based on the data from Table 6.1 and Table 6.2, show a good fit. (6.1) and can be used for quick SynRel sizing at fixed aspect ratio γ based on Equation (6.2) can thus be used as a general sizing equation.

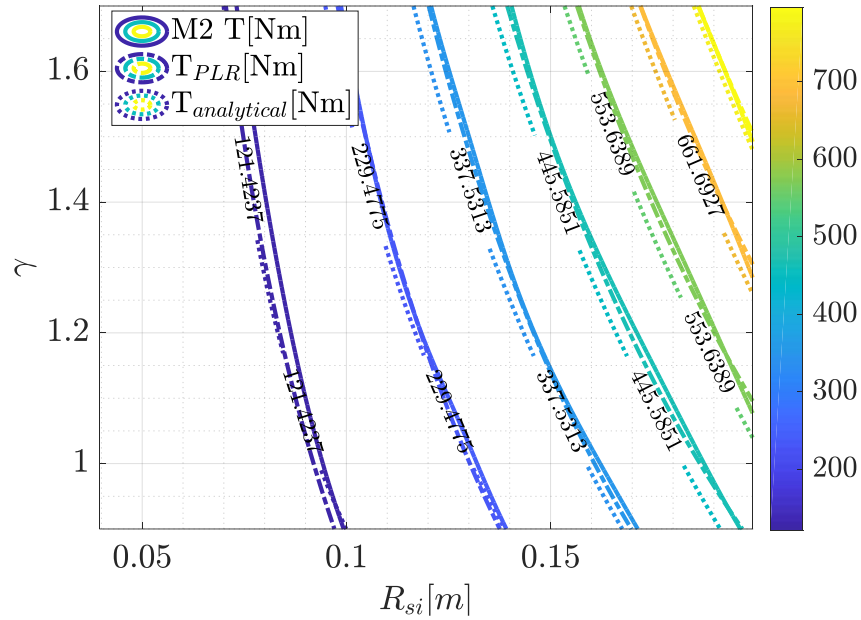


Figure 6.2. $T(R_{si}, \gamma)$ M2 example.

Table 6.2. PLR coefficients for $T(R_{si}, \gamma)$

0 th order			
p_0	-90.07		
	1st order	2 nd order	3 rd order
a_k	1518	-5986	10780
b_j	94.04	-39.23	-
$c_{k,j}$	c_{11}	c_{21}	c_{22}
	$c_{1,1} = -935.3$	$c_{2,1} = 12640$	455

6.4 General Torque as function of α^e :

Using the data generated above the general expressions of p.u. torque as function of current vector α^e can be derived. As can be observed in Figure 5.7 the torque, as function of current angle, have a sinusoidal nature, hence the best way to describe this function is using the line fitting technique “sum of sines”.

Figure 6.3 shows the p.u. torque as function of α^e at five different saturation levels with average p.u. torque values, based on the FE evaluation of M1, M2 and M3. The curves were plotted based on the average of functions of $T_{pu}(mmf_{pu}, \alpha^e)$. The curve fitting presented is derived using the “sum of sines” in the form where α^e is expressed in radians:

$$T_{pu}(mmf_{pu}, \alpha^e) = \sum_{k=1,2,3} a_k \sin(b_k \alpha^e + c_k) \quad (6.3)$$

The coefficients shown in (6.3) presented in the Table 6.3 for five torque profiles.

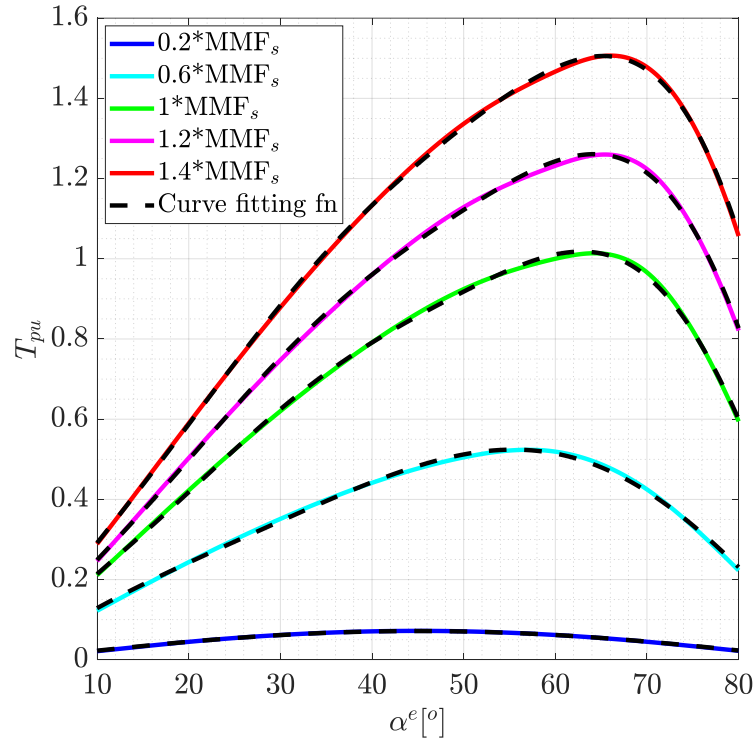


Figure 6.3. p.u Torque as a function of α^e at three different saturation levels.

Table 6.3. Curve fitting coefficients for general function of $T_{pu}(mmf_{pu}, \alpha^e)$

	0.2MMF _s	0.6MMF _s	1MMF _s	1.2MMF _s	1.4MMF _s
a_1	0.07173	0.5147	0.9634	1.25	1.956
b_1	2.036	2.083	1.997	2.149	2.568
c_1	0.03178	-0.1502	-0.1955	-0.2405	-0.3849
a_2	0.07078	0.07078	0.888	1.123	4.302
b_2	-	4.902	6.554	5.69	4.859
c_2	-	2.002	0.8435	1.341	1.743
a_3	-	-	0.7808	0.8917	3.508
b_3	-	-	6.86	6.119	5.113
c_3	-	-	-2.464	-2.027	-1.528

6.5 ISO torque curves:

Based the homothetic identity that was shown on Figure 5.6 a general function of *iso* p.u. torque can be expressed. Using analytically derived data p.u. torque can be derived as function of mmf_d and mmf_q . Since there are two input variables, the PLR can be used. Therefore, the general p.u. torque expression $T_{pu}(mmf_d, mmf_q)$ can be rewritten as (6.4):

$$T_{pu}(mmf_d, mmf_q) \sim \sum_{k,j} a_k mmf_d^k + b_j mmf_q^j + c_{k,j} mmf_d^k mmf_q^j \quad (6.4)$$

Where a_k, b_j are the PLR coefficients. The derived function (6.4) can be used for any SynRel geometry using the reference *MMF* value i.e. from Table 5.3 for M1, M2 and M3, as the p.u. torque have a similar pattern for any scaled machine.

6.6 Case studies and experimental validation:

In order to validate the proposed scaling functions, two existing 4 poles 48 slots SynRel prototypes are considered as case studies, namely M21 and M22. A summary of their key parameters are presented in Table 6.4. The experimental platforms to validate the proposed analytical sizing method is shown in Figure 6.4 and Figure 6.5.

Table 6.4. Summary of two machines scaled from M2 geometry

Symbol	Parameter	M21	M22
S_{si}	Stator scaling factor	1	1.2353
S_{ri}	Rotor scaling factor	1	1.2366
R_{si}	Stator inner diameter	85 mm	105 mm
g	Air gap thickness	0.5 mm	0.5 mm
L_{stk}	Stack length	205 mm	235 mm
γ	Aspect ratio	1.213	1.119
N_s	Number of turns per phase	64 turns	64 turns
I_s	Current at MTPA $\alpha^e=60^\circ$	56.2 A	56.2 A
T	Torque at MTPA $\alpha^e=60^\circ$	123 Nm	174 Nm



Figure 6.4. Test rig: M21 SynRel motor (left hand side) and 40kW induction machine used as a load (right hand side).



Figure 6.5. Test rig: M22 SynRel motor (left hand side) and 160kW induction machine used as a load (right hand side).

On the left hand side, M21 and M22 SynRel prototypes under test are mounted on two test rig coupled with 40kW and 160kW induction machines on the right hand side, respectively. The motors are self-ventilated through a fan mounted on the rotor shaft. A torque meter is installed between two machines. A resolver is also mounted on the non-drive end of the SynRel motors, to provide the speed and position feedback to the drive.

Using equations (6.2), which is a general torque sizing equation, the rated torque for M21 and M22, can be estimated on the $T(R_{si}, \gamma)$ plane. Figure 6.6 shows the torque curves against the stator inner radius R_{si} and the aspect ratio γ . These are derived through the general torque-size relation.

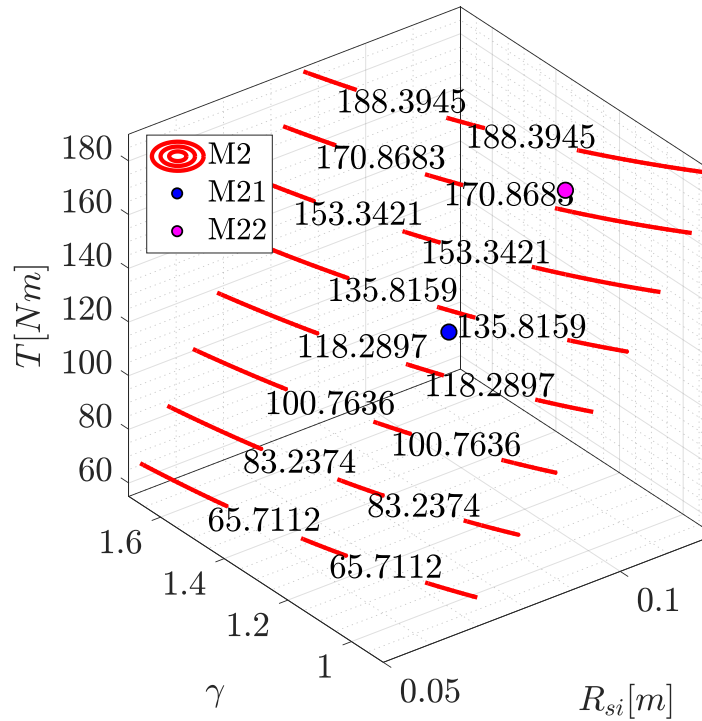


Figure 6.6. General sizing at given rated current (MTPA $\alpha^e=60^\circ$).

As can be observed the experimental results for M21 and M22 at rated current $I_s=56.2A$ and current angle $\alpha^e=60^\circ$ are lying on the same plane showing a very good match. The experimental operating points ($T_{M21} \sim 127.1Nm$, $T_{M22} \sim 176.2Nm$) are highlighted with dots for both machines in Figure 6.6. Compared to the experimental torque values reported in Table 6.4, the torque errors are 3.2% and 1.3%, for M21 and M22, respectively.

The function (6.4) is also useful to estimate the torque behavior on i_d-i_q plane as well as to identify the MTPA at different saturation levels. In Figure 6.7 this is derived for both M21 and M22 where the comparison of experimental and statistically calculated data is presented. This is showing the validity of equation (6.4) which results are in very good match with the experimental measurements.

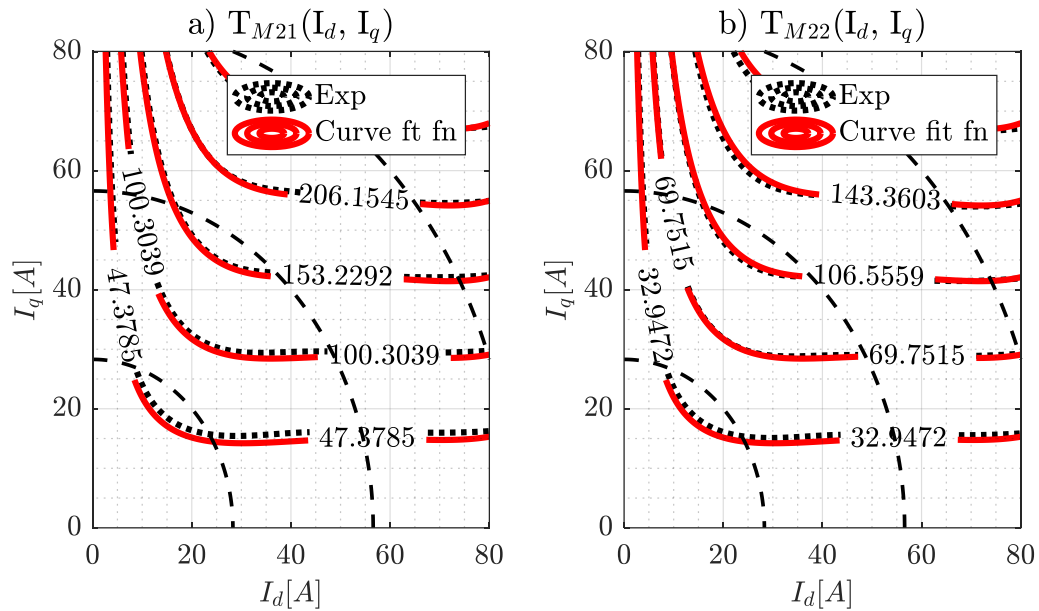


Figure 6.7. Comparison of iso-torque values.

6.7 Conclusion:

This chapter is proposing a novel generalized homothetic approach for a quick and accurate sizing of SynRel machines. Through this concept, the preliminary sizing process which usually comprises heavy FE iterations can be drastically reduced through the use of the proposed sizing equations. These equations were derived using statistical techniques based on a wide range of analytically calculated data, for both radial and axial scaling. The MTPA of the SynRel machines have been analyzed and generalized for any size of the machine with the aid of the proposed analytical tool. Therefore, a consistent behavioral pattern between scaled geometries was defined, in order to derive the general sizing functions. These were validated by means of FE analysis as well as experimentally on 2 SynRel motors (M21 and M22), which are two scaled machines from the same reference geometry M2.

The experimental results obtained show a good match with respect to the statistically derived predictions. At rated current and rated MTPA angle the error is about $\sim 4\%$.

It can be concluded that the proposed method is defining a fast and accurate tool for the preliminary sizing and scaling of SynRel machines. This can be adopted by the industrial community, in particular when the performance assessment of a range of machine is required, starting from a reference design.

Chapter 7: Homothetic Design in Synchronous Reluctance Machines and Effects on Torque Ripple

Following up on the homothety principle for SynRel that was introduced in previous chapters. This chapter presents a novel design concept for Synchronous Reluctance (SynRel) machines aimed at reducing the torque ripple. Two general sizing approaches based on the homothetic scaling principle are defined and compared. An in depth analysis on the torque ripple, for a wide range of scaled geometries, evaluated by finite element, has been carried out at different operating conditions. A further analysis is performed on 4 scaled geometries that have been optimized starting from a 4 random rotor geometries. It is shown that the main rotor geometrical variables converge to similar values for all scaled machines.

7.1 Introduction:

One of the main pitfall of the SynRel machine topology is the conspicuous torque oscillation, which is an undesired torque component causing acoustic noise, vibration and may degrade the drive controllability. Several techniques for the torque ripple reduction have been investigated over the last two decades and they can be classified into two major categories. The first one acts on the control scheme [107], [108], [109], while the second consists of specifically tailored motor-design techniques [19], [20]. The first approach is more broadly applicable but it complicates the control algorithm structure and so its computational cost. While, the second approach obviously requires the development of new machine designs and this is not always possible. Several design techniques have been proved effective in minimizing torque oscillations, such as suitable choice of the flux barriers with respect to the number of stator slots [110], suitable flux barrier angular displacement [111], [112], rotor skewing [113], etc. The proposed design guidelines originate from considerations based on analytical models, which often rely on a set of hypotheses introduced to simplify the analysis, and to make it feasible. Such analytical models most of the time neglect the effect of the non-linearities and geometrical complexities, on the predicted performance. Therefore, they are useful only during the preliminary design stage. The next refining stage

is then carried out by means of finite element (FE) analysis, which is able to evaluate the design aspects disregarded in the first stage (e.g. non-linearities heavily affect the torque profile). During the detailed design phase, several iterations are required and the computational cost depends also on the accuracy of the analytical model used in the preliminary design. Clearly, the more the analytical model is able to predict the machine performance faithfully, the less FE iterations are needed in the second design stage. Indeed, a more accurate analytical model is able to better identify the design space area to further explore via FE analysis. The second design stage is commonly implemented as a FE-based design optimization. Several works have addressed the problem of further reducing the computational burden required to carry out the optimization, which depends on two factors: the computational time required to evaluate the performance of a single machine candidate and the geometrical complexity of the machine structure to be optimized.

The purpose of this chapter is to show how the FE design stage can be greatly simplified and so computationally relieved by considering a novel dimensioning homothetic approach during the first analytical design step. The homothetic scaling design principle was initially introduced for the induction motors in [101], and here is extended to SynRel machines based on the analytical model presented in [103].

7.2 Scaling principle and reference machine design:

In the following two subsections, the preliminary sizing method of the reference machine is outlined along with the scaling principle. The sizing approach has been extensively described in previous chapters, where the anisotropy of the rotor is considered as an input of the design procedure.

Figure 7.1 reports a simplified flow chart of the adopted sizing approach from **Chapter 4**, which includes 5 steps. Starting from the performance requirements and the design constraints, the second step defines the initial guess values of the machine's saliency ratio ξ , the rotor's magnetic insulation ratio k_{air} [103] and the number of barriers k . Using all predefined parameters above, the machine is sized using equation (3.13) during the third step. The saliency ratio is then estimated with an analytical model based on the equations (3.47) [50] and then the electromagnetic torque is calculated with equation (3.1). The machines' torque can

be tuned in an iterative fashion by either varying k , k_{air} or the main rotor diameter D_{ro} , depending on the performance specifications.

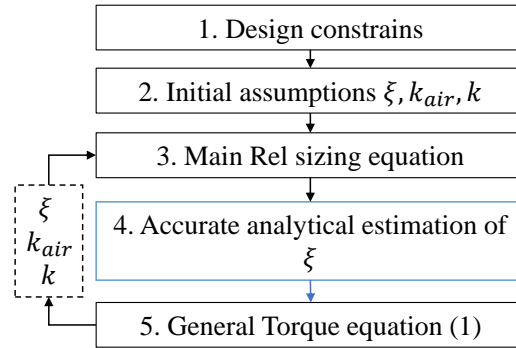


Figure 7.1. A simplified sizing algorithm.

The SynRel machine used in the following as reference design has been initially sized for a household appliance application whose design specification and constraints are listed in Table 7.1. The winding layout was designed based on voltage-speed limit and the current density requirements [84]. Table 7.1 also reports the main dimensions and the winding details of the reference machine.

Table 7.1. Design specifications, constrains and machine parameters.

Symbol	Parameter	Quantity
J_{max}	Peak current density	4 A _{rms} /mm ²
k_{fill}	Slot fill factor	0.4
Q_s	Number of slots	24
$2p$	Pole numbers	4
m	Number phases	3
g	Air gap	0.3 mm
γ	Aspect ratio	0.84
k	Number of barriers	3
T_{em}	Rated Torque	0.9 Nm
n_b	Base speed	5000 rpm
I_{rms}	Phase Current	3.5A
V_{rms}	Phase Voltage	120V
D_{ro}	Rotor outer diameter	59 mm
L_{stk}	Stack length	48 mm
D_{so}	Stator outer diameter	100 mm
N_s	Number of turns per phase	128

7.3 Rotor design of the reference machine:

The rotor geometry of the reference machine has been optimized to be suitable for both reluctance and permanent magnet assistant reluctance variants. For this reason, the rotor barriers are presenting a central rectangular slot, to host permanent magnets if needed, as shown in Figure 7.2. The optimisation has been carried out considering the rotor parameters shown in Figure 7.2 (i.e. barrier angles and thicknesses) and the optimization procedure is fully described in [114].

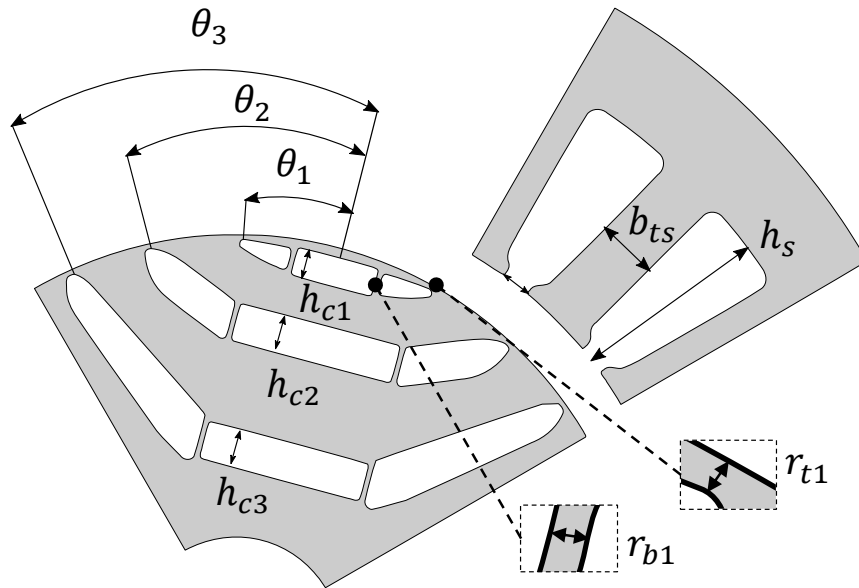


Figure 7.2. Sketch of optimized benchmark machine M1.

7.4 Scaling principle:

Based on the homothetic scaling principle discussed in **Chapter 5**, the reference machine can be scaled both radially and axially.

In the following, the aspect ratio of the scaled machines will be kept constant, therefore the stack length L_{stk} will be scaled proportionally to outer rotor diameter D_{ro} . The radial scaling can be carried out pursuing two approaches, i.e. keeping fixed the airgap length (AGF) and scaling the airgap length (AGS) with the same factor of the cross-sectional parameters. Equations (5.2) and (5.3) describe the scaling factors for the fixed airgap approach:

Clearly, such approach utilizes two different scaling factors, S_{si} for the stator and S_{ro} for the rotor, while when scaling the airgap length as well, the scaling coefficients is the same for both stator and rotor (7.1):

$$S_{si} = S_{ro} = \frac{D_{si-n}}{D_{si-ref}} \quad (7.1)$$

Table 7.2. Scaled geometries

Symbol	Parameter	Quantity		
		M1	M2 (AGS)	M3 (AGF)
S_{si}	Stator scaling coefficient	1	1.5	1.5
S_{ro}	Rotor scaling coefficient	1	1.5	1.505
D_{si}	Stator inner diameter	59.6 mm	90 mm	90 mm
g	Air gap	0.3 mm	0.45 mm	0.3 mm
D_{ro}	Rotor outer diameter	59 mm	89.1 mm	89.4 mm
L_{stk}	Stack length	48 mm	75 mm	75.096 mm
D_{so}	Stator outer diameter	100 mm	153 mm	153 mm
D_{sh}	Shaft diameter	14 mm	22.5 mm	22.75 mm

7.5 Evaluation of the Scaled machines torque performance:

In the following two subsections, the torque ripple of several scaled machines is FE evaluated for different operating points in the d-q axis current plane. In particular, in the first subsection two scaled machines are considered, one obtained keeping fixed the airgap length (M3) while the second (M2) also scaling the latter. Figure 7.2 summarises the geometrical parameters featured by the scaled (M2 and M3) and reference machines (M1). In subsection III-B, the same analysis is extended to a wider range of scaling factors for both AGS and AGF cases, respectively.

7.5.1 FE evaluation of M1, M2 and M3 geometries:

Figure 7.3 presents the average and peak-to-peak torques of the three considered geometries in the d - q current plane. The first row of Figure 7.3 (a and b) reports the torque performance of the reference geometry M1. The central row of Figure 7.3 (c and d) shows the performance of the AGS geometry M2 while the bottom row (Figure 7.3 e and f) represents the AGF geometry M3.

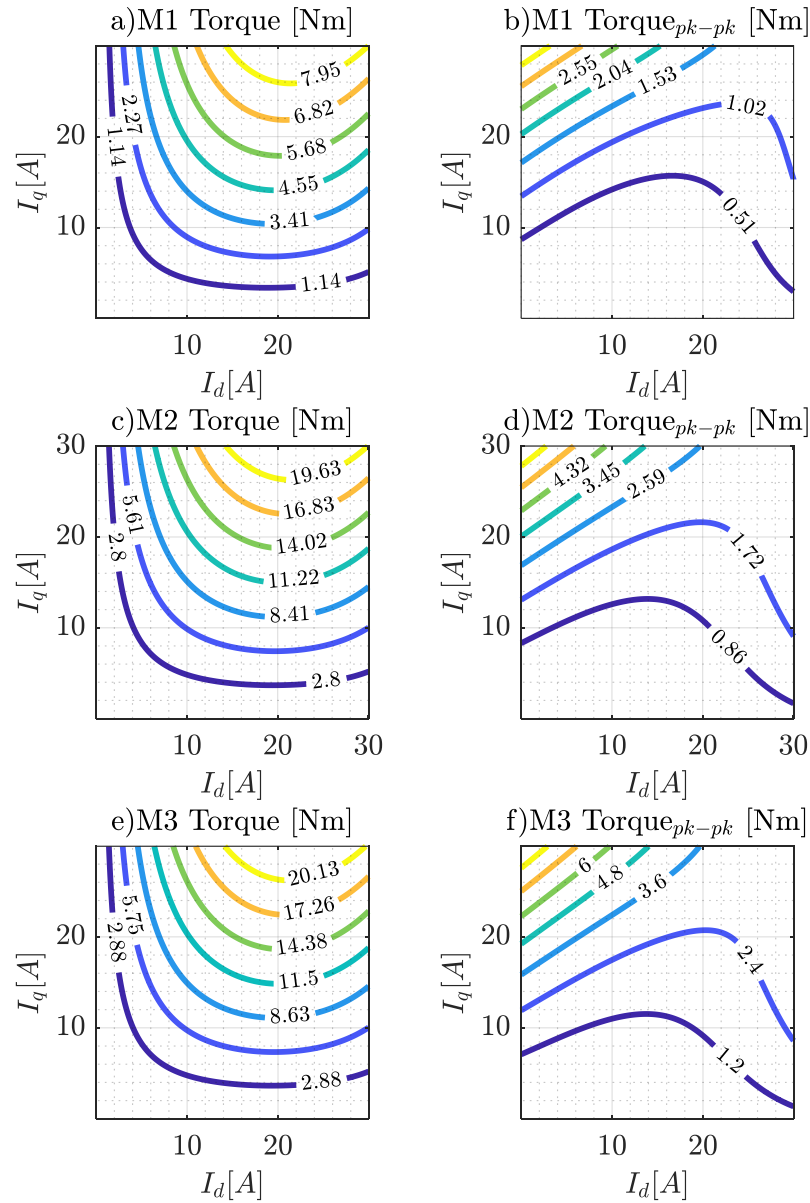


Figure 7.3. Average torque and peak to peak torque on I_d and I_q planes for M1, M2 and M3 machines.

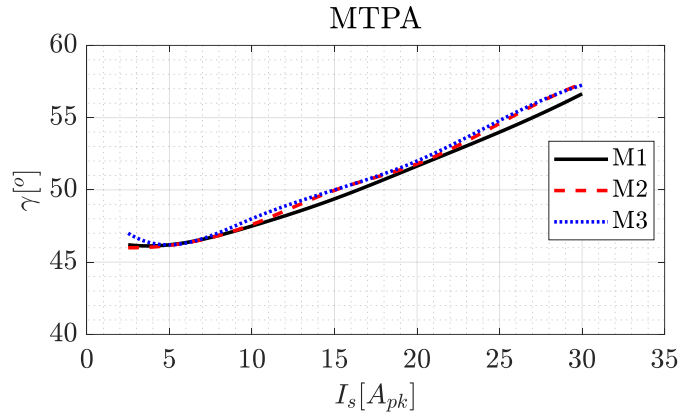


Figure 7.4. M1, M2 and M3 MTPA.

It can be observed that the iso-curve of average torque does not vary significantly, which implies that the maximum torque per ampere (MTPA) locus is almost the same for the three machines as shown in Figure 7.4. The latter reports the current phase angle corresponding to the MTPA condition as function of the current module for the reference and scaled machines. The average torque produced by the M2 geometry is lower compared to one obtained with the M3, i.e. at rated current density of $5\text{A}/\text{mm}^2$ the average torque achieved by M3 $T_{M3}= 5.6\text{Nm}$ whereas $T_{M2}= 6.1\text{Nm}$; this is clearly due to the bigger airgap of the M2 geometries respect to the M3 one.

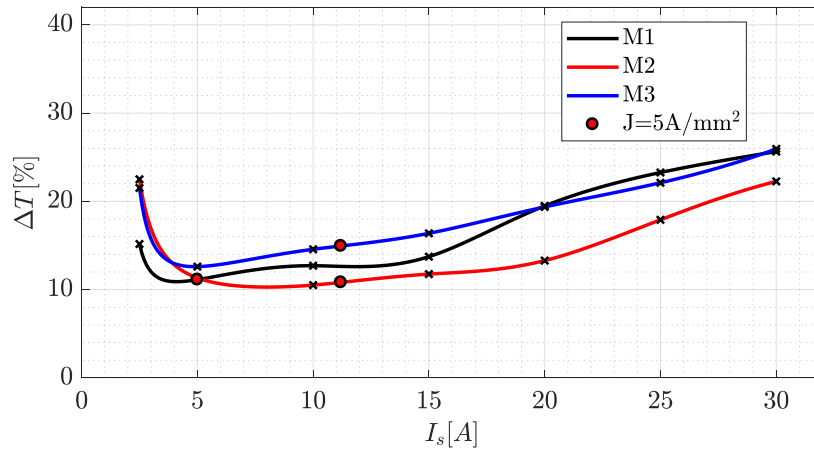


Figure 7.5. Torque ripple vs peak phase current at MTPA.

The torque ripple contours of the scaled geometries M2 and M3 follow the same pattern featured by the reference geometry (M1) as shown in Figure 7.3 b, d and f. Figure 7.5 reports the percentage torque ripple of the three considered machines

at the MTPA condition as function of the current amplitude. The torque ripple of the scaled M2 geometry follows almost the same pattern of the reference geometry M1 except for the really low and high current modules. This is due to bigger air gap; hence it requires higher current to properly saturate the ribs, as the machine was geometrically scaled. The scaled machine M3 shows a higher torque ripple respect to the reference geometry M1 due to different scaling of rotor and stator.

Based on all the above it can be concluded that both scaled machine, M2 and M3, feature a torque ripple comparable with the base geometry. In particular, the torque ripple variations lie within a 15% range over a wide range of currents. As can be observed at rated current density of $5A/mm^2$, the M2 has $T_{\Delta M2} \sim 10.9\%$ whereas M1 shows $T_{\Delta M1} \sim 11\%$; M3 shows relatively higher torque ripple $T_{\Delta M3} \sim 15\%$.

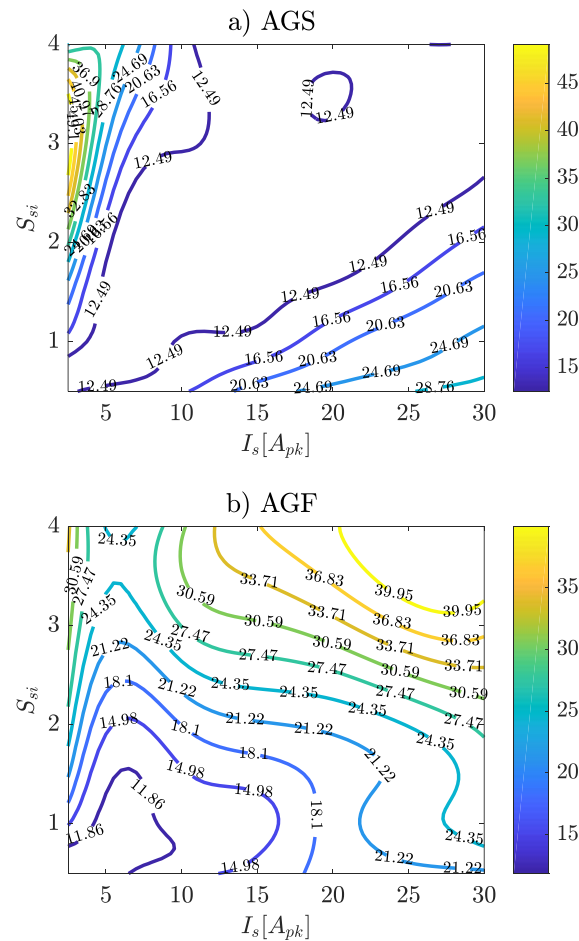


Figure 7.6. $T_{\Delta}(I_s, S_{si})$. Torque ripple vs Peak phase current at MTPA.

7.5.1 FE evaluation of wide range of scaled geometries:

A total of 9 machines have been obtained within the range of $0.5 \leq S_s \leq 4$ by scaling the reference geometry M1 adopting both AGS and AGF approach. Figure 7.6 a) and b) report the percentage torque ripple at MTPA condition in terms of contour in the plane stator inner radius - phase current.

Analysing the torque ripple of the machines uniformly scaled (AGS), it can be noticed that in for low current values (i.e. $5A \leq I_s \leq 20A$), the torque oscillation remains within the range $10\% \leq T_{\Delta} \leq 17\%$ for all the considered radial dimensions and current loading. On the contrary, the torque ripple shown in Figure 7.6 b), related with the AGF geometries, show a significant increment compared to the reference machine M1.

A torque ripple within the range $10\% \leq T_{\Delta} \leq 17\%$ is obtained only for machine having $0.5 \leq S_s \leq 2$. It can be concluded that the AGS scaling approach leads to a moderate torque ripple variation over a wider range of scaling factor, whereas adopting the AGF scaling approach, the torque ripple variation is more pronounced.

7.6 Torque ripple optimization:

The following exercise aims at demonstrating that starting from a random set of rotor parameters, the optimization algorithm converges to an optimal rotor with a geometry similar to the reference one. In order to demonstrate the above statement and the differences between AGS and AGF scaling approach, 4 different scaled machines have been considered and optimized.

Table 7.3. Optimization input variables' boundaries.

Parameter	Symbol	Boundaries		Unit
Flux barrier angle 1	θ_1	13	16	°
Flux barrier angle 2	θ_2	25	28	°
Flux barrier angle 3	θ_3	38	40	°

The first two (M2* and M3*) are the machines considered in **Chapter 7.5** and whose parameters are detailed in Table 7.2. The other two scaled machines (labelled as M4* and M5*) are obtained from the reference one adopting a scaling

coefficient lower than one ($S_{si}=0.75$). The geometries M2* and M4* are obtained via the AGS approach while the M3* and M5* using the AGF method.

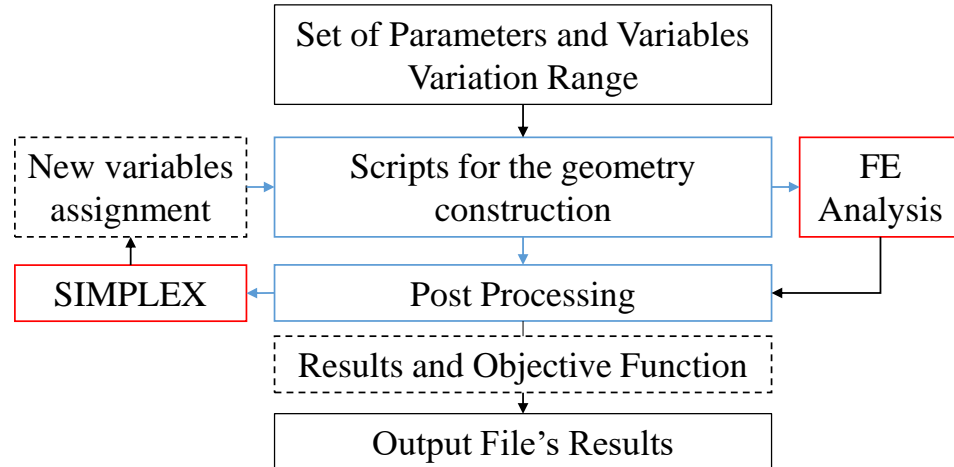


Figure 7.7. Optimization workflow.

The geometrical variables to be optimized are the angles defining the barrier position at the airgap. Table 7.3 reports the lower and upper limits that those variables can assume during the optimization while the stator geometry remain fixed. The insulation ratio, defined as the per unit air portion of flux barriers along the q -axis (3.20).

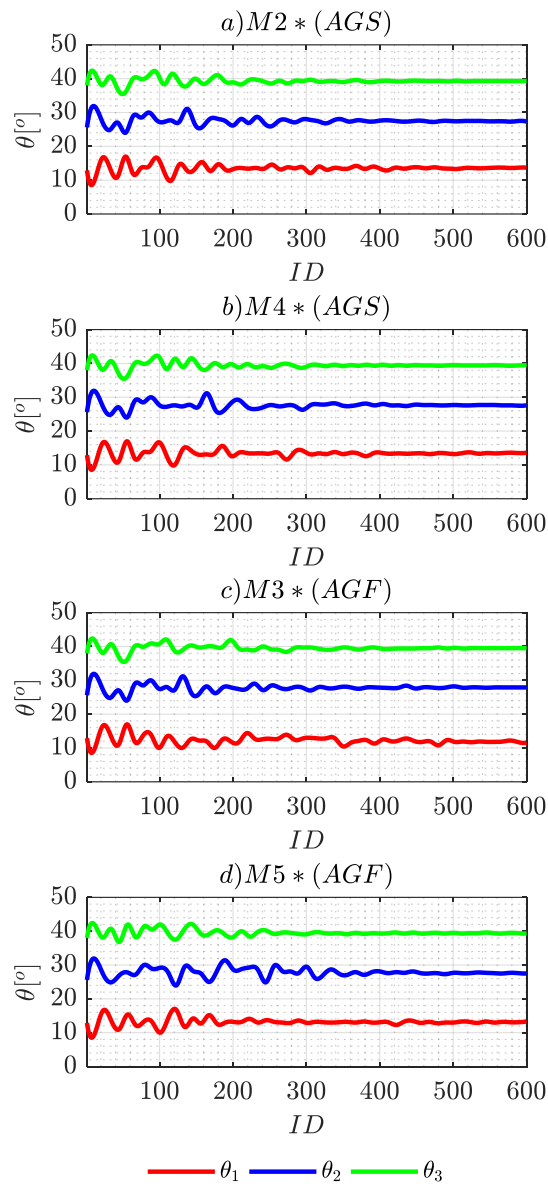


Figure 7.8. Optimization variables trend of M2*, M3*, M4*, M5*.

The choice of keeping the insulation ratio (k_{air}) invariant during the optimization is related with the need of obtaining machine producing approximately the same average torque. Indeed, it has been demonstrated that the insulation ratio has a bigger impact on the average than the flux barrier angles as it has been shown in [115].

With the choices motivated above, the optimisation problem presents a single objective function, the torque ripple. An heuristic optimiser (simplex algorithm) has been adopted to carry out the FE-based design optimization whose workflow

is shown in Figure 7.7. The initial Design of Experiments table used to start the search has been defined by a random sequence. The number of individuals for each generation has been set to 60 and a maximum of 10 generations has been considered leading to a total of 600 functional evaluations. An automatic drawing and solving procedure has been implemented via Matlab and the finite element software FEMM 4.2. The torque ripple (at MTPA condition with a current density of 5 A/mm^2) of each machine candidate is determined by a series of static simulation performed uniformly over one torque ripple period.

Figure 7.8 shows how the geometrical variables converge to the optimal values leading to the minimum torque ripple for the scaled machines M2*, M3*, M4*, M5*. It can be clearly observed that the trends of the barrier angles converge approximately to the same angles. The summary of optimal angles is reported in . Based on the convergence of the angles value, it can be noticed that the variations of the θ_2 and θ_3 are not significant, all within a range of 0.4° , whereas the difference in θ_1 is significant only for M3* geometry. This can be explained by its disproportional scaling compared to other geometries, as it discussed in the previous section.

It can be concluded that the homothetic scaling, starting from a well designed and optimized reference geometry, lead to a scaled design which is a solution that can be considered optimal, or for sure a good starting point for further torque ripple optimization refinements. Consequently, the design variable boundaries can be greatly restricted relieving the computational burden of the FE refinement design stage.

Table 7.4. Summary of the optimal flux barrier angles

	M1	M2*	M3*	M4*	M5*	Unit
θ_1	13.3	13.6	11.6	13.5	13.3	°
θ_2	27.6	27.3	27.9	27.6	27.5	°
θ_3	39.4	39.3	39.5	39.4	39.3	°

7.7 Mechanical considerations:

In this section other mechanical aspects not previously considered are discussed. The thermal behaviour of the electrical machine is mainly a function of the current density, as well as the cooling type that is adopted by the system [116]. The current density was kept constant for all 5 machines including M1, therefore current was

proportionally scaled, as the area of the slot is increased or decreased. As shown in Table 7.5, the area of the slot is scaled by S_{si}^2 . Electric loading A_s is highlighted in Table 7.5 to illustrate the difference among the analysed motor variants.

Table 7.5. Details of validation

Label	S_{si}	Slot Area	I_s at $J=4A/m$ m ²	I_s at $J=5A/m$ m ²	A_s $J=4A/$ mm ²	A_s $J=4A/$ mm ²	Scaling principle
M1	1	68.2 mm ²	4A	5A	16.57 kA/m	20.72 kA/m	-
M2	1.5	153.4 mm ²	9A	11.25 A	10.97 kA/m	13.72 kA/m	AGS
M3	1.5	153.4 mm ²	9A	11.25 A	10.8 kA/m	13.6 kA/m	AGF
M4	0.75	38.4 mm ²	2.25 A	2.81 A	22.1 kA/m	27.62 kA/m	AGS
M5	0.75	38.4 mm ²	2.25 A	2.81 A	22.2 kA/m	27.7 kA/m	AGF

Table 7.6. Details of FE mechanical simulations.

Symbol	Parameter	Quantity
$r_{b1}=r_{b2}=r_{b3}$	Radial ribs	0.7 mm
$r_{t1}=r_{t2}=r_{t3}$	Tangential ribs	0.6 mm
ρ_d	Density	7650 kg/m ³
ϵ_p	Poisson's ratio	0.3
γ_{coef}	Young's coefficient	200 GPa
σ_{stress}	Yield Stress	440 MPa

In a SynRel motor, the design of both radial and tangential ribs has been investigated extensively [116], [117], [118]. The function of the iron ribs is to mechanically retain the rotor parts together and to withstand the centrifugal force depending on the speed of the machine. Hence the ribs thickness is mainly affected by the maximum speed and the rotor geometry. For example, if the scaling leads to thinner ribs the maximum allowable speed of the machine could be affected and a mechanical refinement is required to guarantee the structural integrity of the rotor. In the presented homothetic method, the ribs have been scaled proportionally. This is valid within certain scaling range.

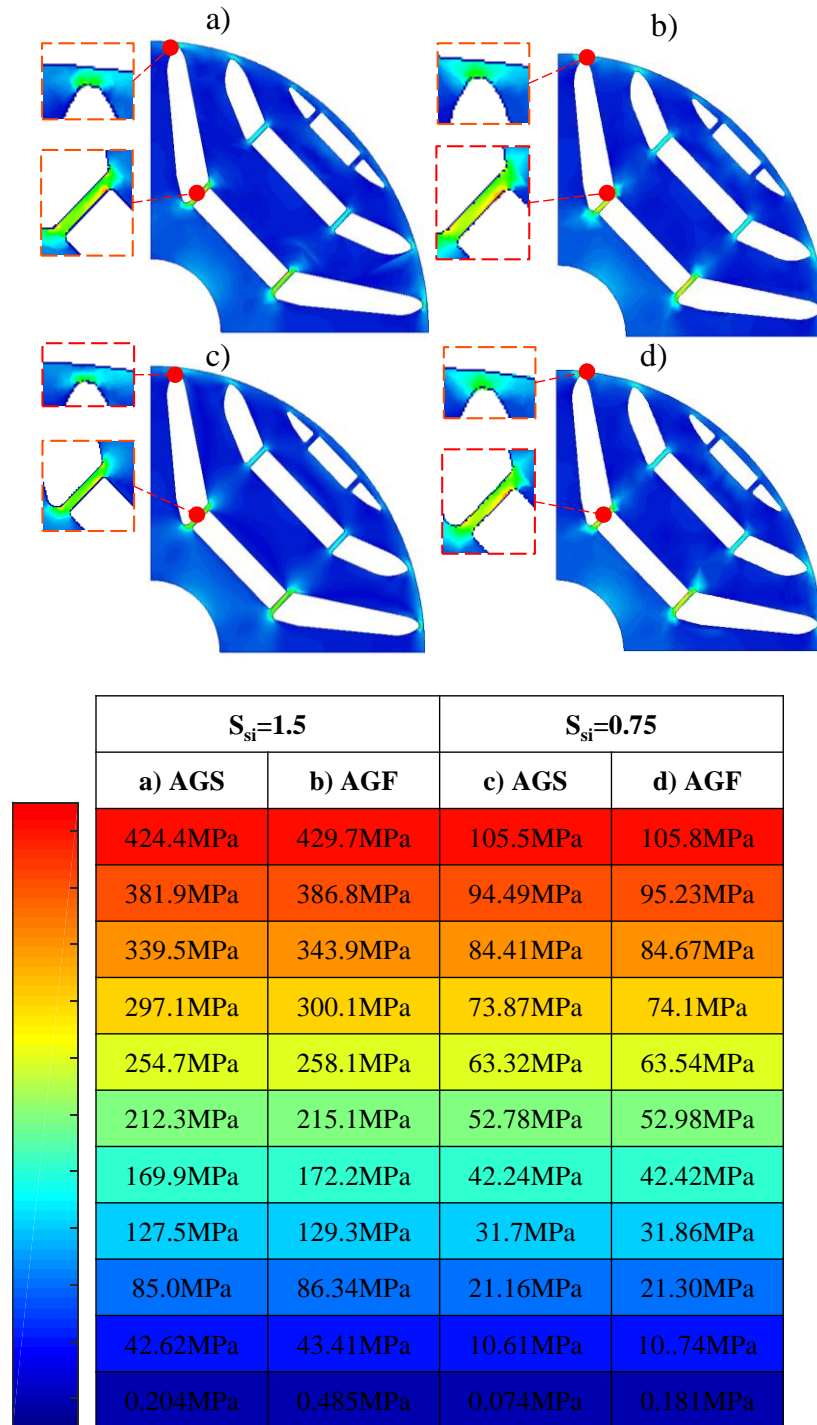


Figure 7.9. FE stress maps of scaled rotor geometries at $n=18000$ rpm.

Figure 7.9 presents the FE simulated mechanical stress maps for 4 scaled geometries $S_{si} = 0.75, 1.5$ at $n=18000$ rpm. Mechanical FE simulations were carried

out considering the parameters of the original geometry M1 as shown in Figure 7.9, with highlighted ribs thicknesses according to Figure 7.2 and physical properties of the silicon steel used. As can be observed the smaller scaled geometries $S_{si} = 0.75$ have the peak stress at the ribs which is within the allowable value of the σ_{stress} , whereas the $S_{si} = 1.5$ scaled geometries are close to the yield stress σ_{stress} .

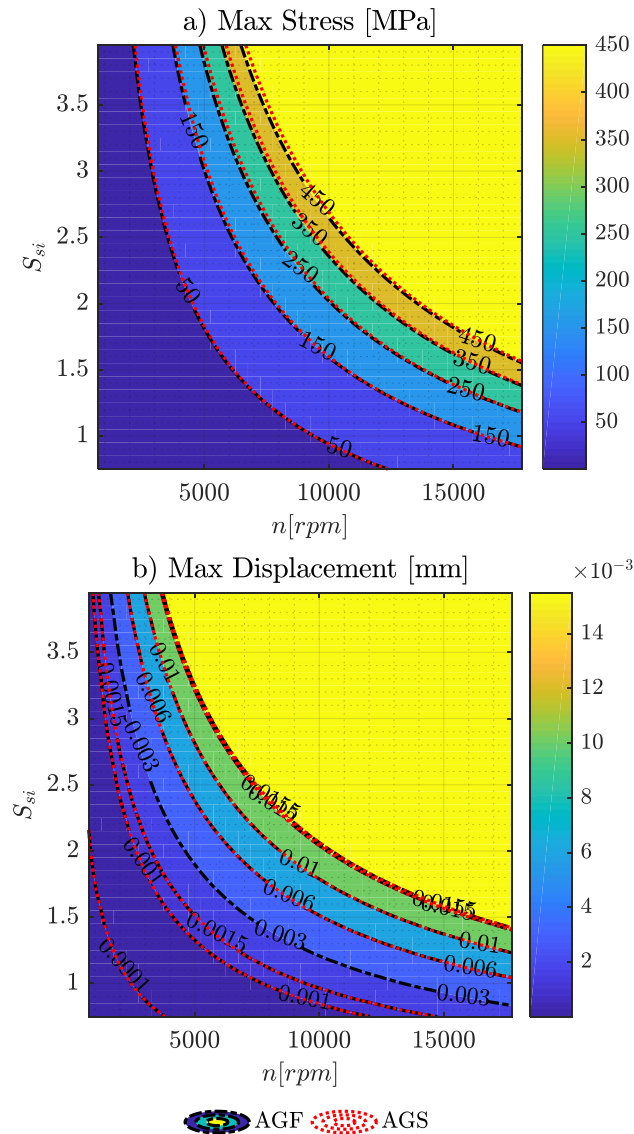


Figure 7.10. Mechanical analysis of scaled geometries for AGS and AGF scaled geometries a) Maximum stress b) Maximum displacement c) Safety factor as functions of scaling factor S_{si} and rotational speed n in rpm

Figure 7.10 presents the results for a wider speed range based on FE simulated mechanical stress test of 7 different geometries: 3 geometries were scaled based on (8) and (9) (AGF) and 3 geometries were scaled using (10) (AGS) and original geometry M1. Figure 7.10 a) presents the maximum stress as function of scaling factor and speed where the maximum stress can be identified for different combination of the two parameters. The region depicted in yellow clearly shows mechanical unfeasible solutions which requires a further structural refinement stage. Figure 7.10 b) presents the maximum displacement as function of scaling factor and speed.

Another mechanical consideration is related to the manufacturability of the rotor laminations. The thinnest part of the rotor lamination, i.e. the iron bridge, cannot be below a certain limit depending on the manufacturing method and selected material. In this case, it is not recommended to scale the original geometry M1 lower than $S_{si} < 0.75$, as the ribs thickness will be lower than 0.45mm.

Chapter 8: Experimental validation of the torque ripple:

The theory proposed in previous chapter was validated experimentally. The torque ripple of the scaled machines, computed by means of FE simulations is compared against the experimental measurements on the reference machine prototype for different operating conditions.

8.1 Introduction:

Following up with theory proposed in previous chapter. In this section, four geometries are evaluated and compared to the prototype M1 (geometry presented in Table 7.1). These were designed according to different scaling methods, two geometries using AGF (5.2) - (5.3) and two geometries using AGS (7.1), respectively. The current density was kept constant for all 5 machines including M1, therefore current was proportionally scaled, as the area of the slot is increased or decreased. As shown in Table 7.5, the area of the slot is scaled by S_s^2 .

In the following subsections the evaluation of the torque ripple will be carried out for two current densities, 4 and 5 A/mm², respectively, using the data from Table 7.5. The winding configuration, is kept constant, whereas the number of turns per phase $N_s=128$ for all machines.

8.2 FE torque ripple analysis for scaled machines:

In Figure 8.1 a) and b) the results of the torque ripple analysis, conducted for reduced-scaled machines M4 and M5 ($S_s=0.75$), considering different current angles and loading, are shown. In Figure 8.1 a) the ripple oscillations, evaluated for a current angle of 45 electrical degrees ($\alpha^e=45^\circ$), are presented. At $J = 4 \text{ A/mm}^2$ their values are $T_{\Delta M4}=15.1\%$ and $T_{\Delta M5}=13.23\%$, and at $J = 5 \text{ A/mm}^2$ are $T_{\Delta M4}=11.72\%$ and $T_{\Delta M5}=10.79\%$, for M4 and M5, respectively. It can be observed that M4 achieves higher torque for both current profiles compared to M5, this is mainly due to the increased air gap with respect to rotor size, when the AGF scaling is applied.

According to the waveforms shown in Figure 8.1 b), evaluated for a current angle of 50 electrical degrees ($\alpha^e=50^\circ$), the torque ripples at $J = 4 \text{ A/mm}^2$ are

$T_{\Delta M5}=13.18\%$ and $T_{\Delta M4}=12.7\%$, while at $J = 5 \text{ A/mm}^2$ are $T_{\Delta M5}=11.78\%$ and $T_{\Delta M4}=10.1\%$, for M4 and M5, respectively.

The same analysis has been carried out in a similar fashion for the scaled machines M2 and M3 ($S_s=1.5$). The FE simulation results are shown in Figure 8.1 c) and d). For a current density $J = 4 \text{ A/mm}^2$ their values are $T_{\Delta M3}=15.71\%$ and $T_{\Delta M2}=11.15\%$, while at $J = 5 \text{ A/mm}^2$ are $T_{\Delta M3}=16.7\%$ and $T_{\Delta M2}=11.69\%$, for M2 and M3, respectively. It can be observed that the torque ripple is increased for AGF scaled machine (M3), compared to AGS scaled (M2).

This confirms the behaviour shown in Figure 7.3 and Figure 7.6, where the machines that are scaled by AGF method have a significant ripple increase for machines with larger diameter. On the contrary, the average torque of the M3 is higher with respect to M2. For the sake of clarity, a summary of the above results is reported in Table 8.1, that will be described in the following section.

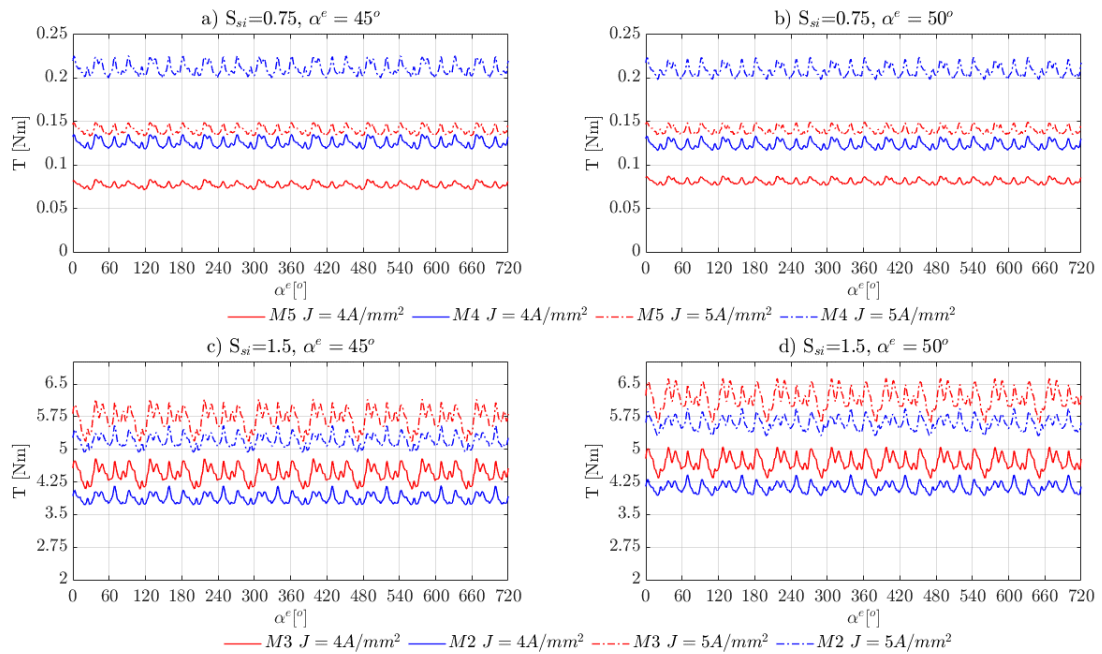


Figure 8.1. FE evaluation of the torque ripple at different current angles and different current loading: a) and b) scaled machines $S_s = 0.75$, (M4 vs M5); c) and d) scaled machines $S_s = 1.5$, (M2 vs M3).

8.3 Experimental results and validation:

In order to validate the proposed theory, the SynRel machine M1 (reference machine), with 24 slots 4 poles, has been tested on an instrumented test rig. The stator and rotor laminations of the prototype are shown in Figure 8.2.

The machine torque ripple has been characterised on a custom test rig presented in Figure 8.3, described in detail in [119], [120]. The tests are carried out at low speed in order to capture the high frequency nature of the torque oscillations. The motor M1 under test is connected through a torque meter to a master motor (dyno). Between the latter and the machine under test, a non-reversible gearbox is reducing the speed by a 1:59 ratio, as sketched in Figure 8.3. The torque is measured for different current amplitudes and different current angles. The control algorithm is implemented on a dSpace 1104 platform.

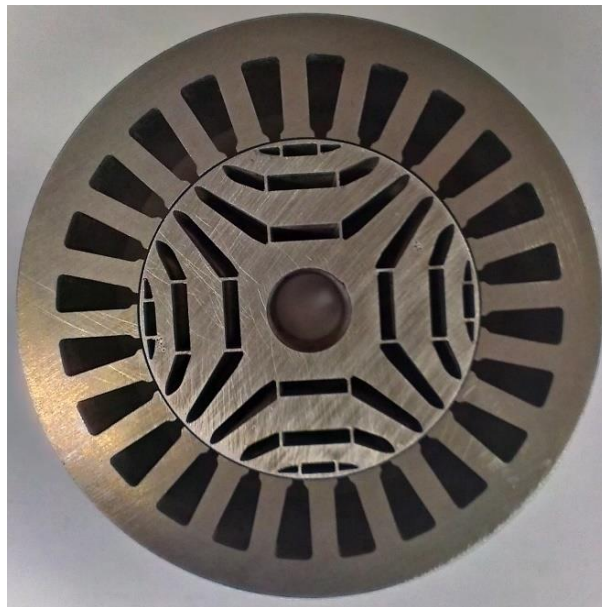


Figure 8.2. M1 SynRel prototype front view.

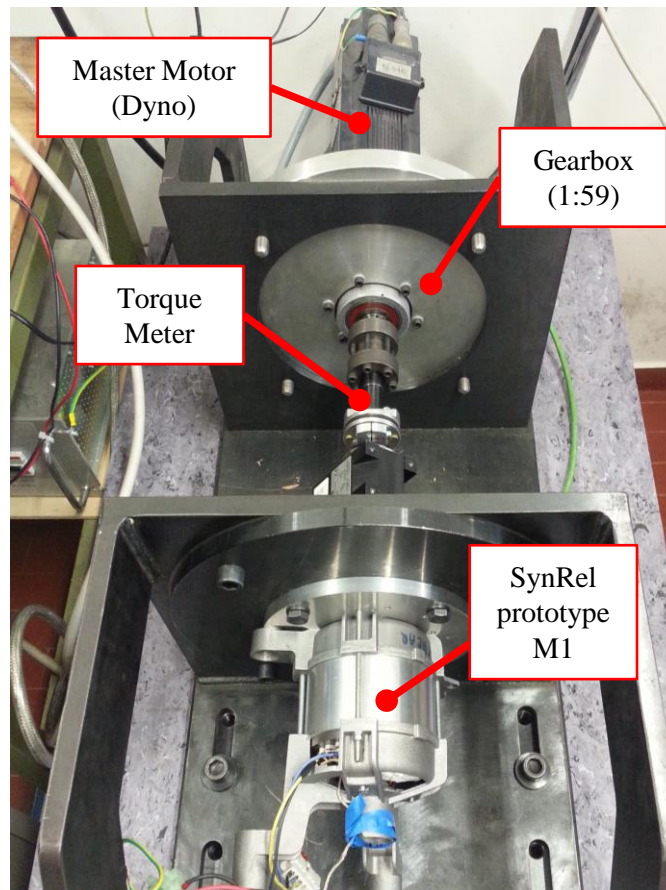


Figure 8.3. Experimental test setup.

At first the test was carried out at current angle $\alpha^e=45^\circ$. Figure 8.4 a) presents experimental and FE evaluation of the torque ripple waveforms at $J = 4 \text{ A/mm}^2$ and $J = 5 \text{ A/mm}^2$, at $\alpha^e=45^\circ$, respectively. As can be observed the torque ripple waveform determined via FE matches very well the experimental data. The measured torque ripple at $J = 4 \text{ A/mm}^2$ is $T_{\Delta MI}=13.4\%$ with an average torque $T=0.56\text{Nm}$, whereas the FE evaluation gives $T_{\Delta MI}=12.6\%$ with average torque $T=0.576\text{Nm}$. For further validation, the same has been carried out for a higher current density value $J = 5 \text{ A/mm}^2$, where the measured torque ripple is $T_{\Delta MI}=11.21\%$ with average torque $T=0.89\text{Nm}$, whereas the FE evaluation gives a value of $T_{\Delta MI}=11.13\%$ with an average torque $T=0.89\text{Nm}$.

Based on these results, it can be said that the FE simulations predict the torque ripple accurately, with a slight under estimation. In fact, the average error with respect to experimental data is about $\delta_{FEA}\sim 2.4\%$.

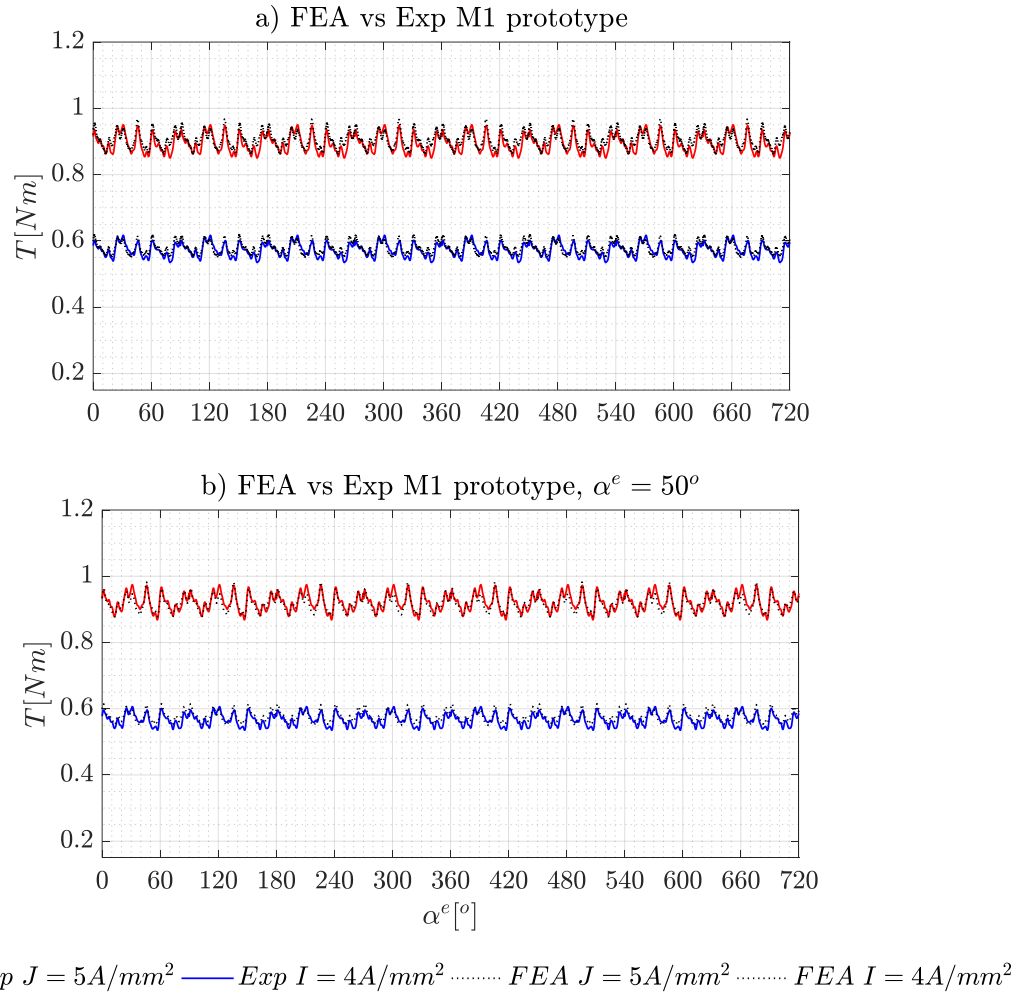


Figure 8.4. Experimental and FE evaluation of the torque ripple on the reference machine M1: a) at 45° current angle for different current loading; b) at 50° current angle for different current loading.

Additional experimental tests have been carried out at a different current angle, $\alpha^e=50^\circ$. Figure 8.4 b) shown the experimental and FE evaluation of the torque ripple waveforms at $J = 4 A/mm^2$ and $J = 5 A/mm^2$, at $\alpha^e=50^\circ$, respectively.

Similarly, to Figure 8.4 a), these results are confirming again that the FE simulated torque ripple waveforms are in line with the measured data. The experimentally obtained torque ripples for a current angle $\alpha^e=50^\circ$, at $J = 4 A/mm^2$, are $T_{\Delta MI}=12.6\%$ with average torque $T=0.567Nm$, whereas the FE ones $T_{\Delta MI}=11.16\%$ with average torque $T=0.577Nm$. For higher current density, $J = 5 A/mm^2$, the experimental torque ripple is $T_{\Delta MI}=11.21\%$ with average torque $T=0.921Nm$, whereas FE $T_{\Delta MI}=11.16\%$ with average torque $T=0.926Nm$.

In order to summarise all the results from both experimental measurements and FE simulations, for the different operating conditions considered, Table 8.1 is reporting the data for all machines analysed.

Table 8.1. Summary of the torque ripple evaluation

Label	T(Nm) at $J=4A/mm^2$		T(Nm) at $J=5A/mm^2$		T_{Δ} (%) at $J=4A/mm^2$		T_{Δ} (%) $J=5A/mm^2$	
	45°	50°	45°	50°	45°	50°	45°	50°
M1 (EXP)	0.56	0.56	0.89	0.92	13.4	11.6	11.2	11.2
M1 (FE)	0.57	0.57	0.89	0.93	13.6	11.2	11.1	11.1
M2	3.87	4.12	5.2	5.6	11.2	11.5	11.7	11.1
M3	4.4	4.7	5.7	6.17	15.7	15.2	16.7	16.3
M4	0.125	0.12	0.21	0.21	15.1	12.7	11.7	12.7
M5	0.077	0.081	0.14	0.14	13.2	13.2	10.8	11.8

8.4 Conclusion:

This chapter aims at defining a novel approach for the design of SynRel machines with minimum torque ripple, based on a homothetic scaling principle. Two main scaling principles have been defined, which are the fixed air gap for the scaled machines AGF and scaled air gap for the scaled machines AGS. The correlations between the torque ripple of a reference machine with respect to a scaled machine is analysed in depth.

It has been demonstrated that the homothetic scaling method proposed leads to a design that can be considered optimal, or to a solution that is a good starting point for a further torque ripple optimization refinement. This approach is significantly reducing the computational time to obtain a machine with a minimum torque oscillation. In fact, all scaled machine has shown less than 5% increase in torque ripple with respect to reference machine. The torque ripple waveforms have been experimentally validated on manufactured prototype of the

reference machine M1. The measured torque profiles are showing a very good match with respect to the FE evaluations. It can be concluded that the proposed method is defining a fast and accurate scaling technique for the preliminary design of the SynRel machines. This can be adopted by the industrial community, in particular when the performance assessment of a range of machine is required, starting from a reference design.

Chapter 9: Conclusion and Future Works

This thesis has proposed advanced methodologies for dimensioning and design of SynRel machines, based on accurate but fast analytical model.

A novel sizing approach for SynRel machine was presented in *Chapter 3* and *Chapter 4*. It can be said that the derived set of equations that are used during the sizing process are important especially for reluctance machines since they reflect the anisotropic nature of the rotor. The approach relies on accurate estimations of the direct and quadrature inductance values, also known as the saliency ratio. The sizing approach presented can be extended on other machine topologies such as PMSynRel and IPM machines. Both of these topologies do have reluctance torque component. Therefore, developing a unified dimensioning method that is able to consider both reluctance and excitation torque components can be the next step in this matter.

A homothetic scaling criteria that was applied on SynRel machines was presented in *Chapter 5* and *Chapter 6*. A generalized modeling approach, based on the saliency ratio, was used to analytically evaluate the magnetic behavior of the scaled SynRel machines. The analytical model has been applied to a wide range of machines. General scaling functions were derived to size and evaluate the performance of the scaled machines using the data resulting from the analytical model. The effect of the homothetic design on torque ripple of SynRel was evaluated in *Chapter 7* and *Chapter 8*. An in depth analysis of the torque ripple, for a wide range of scaled geometries, evaluated by finite element, has been carried out at different operating conditions. The problem with the homothetic scaling of SynRel comes from the mechanical point of view as it was shown in Figure 7.10. Further mechanical and electromagnetic analysis of radially scaled machines can be performed. In example the rotor geometrical parameters can be scaled disproportionately. The ribs can be scaled at higher rate or sometimes fixed for a set of scaled machines in order to find the optimum mechanical and electromagnetic design.

References

- [1] N. Bianchi, M. Degano, and E. Fornasiero, "Sensitivity analysis of torque ripple reduction of synchronous reluctance and interior PM motors," *IEEE Trans. Ind. Appl.*, vol. 51, no. 1, pp. 187–195, 2015, doi: 10.1109/TIA.2014.2327143.
- [2] A. T. De Almeida, F. J. T. E. Ferreira, and G. Baoming, "Beyond induction motors—Technology trends to move up efficiency," *IEEE Trans. Ind. Appl.*, vol. 50, no. 3, pp. 2103–2114, 2013.
- [3] T. Matsuo and T. A. Lipo, "Rotor design optimization of synchronous reluctance machine," *IEEE Trans. Energy Convers.*, vol. 9, no. 2, pp. 359–365, 1994.
- [4] T. Matsuo and T. A. Lipo, "Field oriented control of synchronous reluctance machine," in *Proceedings of IEEE Power Electronics Specialist Conference-PESC'93*, 1993, pp. 425–431.
- [5] H. Hofmann and S. R. Sanders, "High-speed synchronous reluctance machine with minimized rotor losses," *IEEE Trans. Ind. Appl.*, vol. 36, no. 2, pp. 531–539, 2000.
- [6] B. K. Bose, "A high-performance inverter-fed drive system of an interior permanent magnet synchronous machine," *IEEE Trans. Ind. Appl.*, vol. 24, no. 6, pp. 987–997, 1988.
- [7] R. D. King, "Combined electric starter and alternator system using a permanent magnet synchronous machine." Google Patents, 1989.
- [8] G. Friedrich, "Experimental comparison between wound rotor and permanent magnet synchronous machine for integrated starter generator applications," in *2010 IEEE Energy Conversion Congress and Exposition*, 2010, pp. 1731–1736.
- [9] K. Miyashita, S. Yamashita, S. Tanabe, T. Shimozu, and H. Sento, "Development of a high speed 2-pole permanent magnet synchronous motor," *IEEE Trans. Power Appar. Syst.*, no. 6, pp. 2175–2183, 1980.
- [10] C. M. Donaghy Spargo, "Synchronous Reluctance Motor Technology: Industrial Opportunities, Challenges and Future Direction," *Eng. Technol. Ref.*, vol. 44, no. May, pp. 1–15, 2016, doi: <http://dx.doi.org/10.1049/etr.2015.0044>.

- [11] T. Vaimann, A. Kallaste, A. Kilk, and A. Belahcen, "Magnetic properties of reduced Dy NdFeB permanent magnets and their usage in electrical machines," in *2013 Africon*, 2013, pp. 1–5.
- [12] G. Pellegrino, T. M. Jahns, N. Bianchi, W. L. Soong, and F. Cupertino, *The rediscovery of synchronous reluctance and ferrite permanent magnet motors: tutorial course notes*. Springer, 2016.
- [13] M. J. Kramer, R. W. McCallum, I. A. Anderson, and S. Constantinides, "Prospects for non-rare earth permanent magnets for traction motors and generators," *Jom*, vol. 64, no. 7, pp. 752–763, 2012.
- [14] J. H. Rademaker, R. Kleijn, and Y. Yang, "Recycling as a strategy against rare earth element criticality: a systemic evaluation of the potential yield of NdFeB magnet recycling," *Environ. Sci. & Technol.*, vol. 47, no. 18, pp. 10129–10136, 2013.
- [15] A. T. De Almeida, F. J. T. E. Ferreira, and A. Quintino, "Technical and economical considerations on super high-efficiency three-phase motors," in *48th IEEE Industrial & Commercial Power Systems Conference*, 2012, pp. 1–13.
- [16] P. Waide and C. U. Brunner, "Energy-efficiency policy opportunities for electric motor-driven systems," 2011.
- [17] R. E. Machines—Part, "30-1: Efficiency classes of line operated AC motors (IE code)," *IEC Stand.*, pp. 60030–60034, 2014.
- [18] E. E. Directive, "Directive 2012/27/EU of the European Parliament and of the Council of 25 October 2012 on energy efficiency, amending Directives 2009/125/EC and 2010/30/EU and repealing Directives 2004/8/EC and 2006/32," *Off. Journal, L*, vol. 315, pp. 1–56, 2012.
- [19] M. Degano, M. Di Nardo, M. Galea, C. Gerada, and D. Gerada, "Global design optimization strategy of a synchronous reluctance machine for light electric vehicles," *IET*, 2016.
- [20] N. Bianchi and H. Mahmoud, "An Analytical Approach to Design the PM in PMAREL Motors Robust Toward the Demagnetization," *IEEE Trans. Energy Convers.*, vol. 31, no. 2, pp. 800–809, 2016, doi: 10.1109/TEC.2016.2523556.
- [21] P. Bertoldi, "Recent development in energy efficiency policy in the EU," 2015.
- [22] A. de Almeida, F. Ferreira, J. Fong, and P. Fonseca, "Ecodesign Assessment of Energy-Using Products-EuP Lot 11 Motors," *Final Rep. Eur. Comm.*, 2008.

- [23] A. T. de Almeida, F. J. T. E. Ferreira, J. A. C. Fong, and C. U. Brunner, "Electric motor standards, ecodesign and global market transformation," in *2008 IEEE/IAS Industrial and Commercial Power Systems Technical Conference*, 2008, pp. 1–9.
- [24] Z. Wang, Y. Enomoto, H. Tokoi, A. Komura, T. Obata, and K. Souma, "Development of IE5 high efficiency motor with iron-base amorphous magnetic cores," *Energy Effic. Mot. Driven Syst.*, vol. 15, 2015.
- [25] A. T. De Almeida, F. J. Ferreira, and J. A. C. Fong, "Standards for efficiency of electric motors," *IEEE Ind. Appl. Mag.*, vol. 17, no. 1, pp. 12–19, 2010.
- [26] H. Gavrilă, V. Manescu, G. Paltanea, G. Scutaru, and I. Peter, "New Trends in Energy Efficient Electrical Machines," *Procedia Eng.*, vol. 181, pp. 568–574, 2017.
- [27] P. Fanning, "IE5 and beyond," *Eureka*, 2020.
- [28] "ABB SynRM Motors Without Rare Earth Magnets Deliver Ultra-Premium Energy Efficiency," *Magnetics*, Aug. 2020. <https://magneticsmag.com/abb-synrm-motors-without-rare-earth-magnets-deliver-ultra-premium-energy-efficiency/>.
- [29] M. Božić, M. Rosić, B. Koprivica, M. Bjekić, and S. Antić, "Efficiency classes of three-phase, cage-induction motors (IE-code) software," in *INDEL2012, IX Symposium Industrial Electronics, INDEL*, 2012, pp. 87–91.
- [30] A. De Almeida, J. Fong, and H. Falkner, "New European ecodesign regulation proposal for electric motors and drives," in *Proceedings of the 9th International Conference on Energy Efficiency in Motor Driven Systems (EEMODS'15)*, 2015, pp. 15–17.
- [31] A. T. de Almeida, J. Fong, H. Falkner, and P. Bertoldi, "Policy options to promote energy efficient electric motors and drives in the EU," *Renew. Sustain. Energy Rev.*, vol. 74, pp. 1275–1286, 2017.
- [32] C. U. Brunner, R. Werle, and R. Tieben, "The Motor Systems Retirement Program," 2015.
- [33] A. Marfoli, M. Di Nardo, M. Degano, C. Gerada, and W. Chen, "Rotor Design Optimization of Squirrel Cage Induction Motor-Part I: Problem Statement," *IEEE Trans. Energy Convers.*, 2020.
- [34] M. Di Nardo, A. Marfoli, M. Degano, C. Gerada, and W. Chen, "Rotor Design Optimization of Squirrel Cage Induction Motor-Part II: Results Discussion," *IEEE Trans. Energy Convers.*, 2020.

- [35] J. Cui *et al.*, “Current progress and future challenges in rare-earth-free permanent magnets,” *Acta Mater.*, vol. 158, pp. 118–137, 2018.
- [36] D. Bauer, D. Diamond, J. Li, D. Sandalow, T. Paul, and B. Wanner, “US Department of Energy Critical Materials Strategy,” 2010.
- [37] “No Title,” *USGS Mineral Commodities Summaries*. .
- [38] “Magnetic Materials, a Global Strategic Business Report,” *Analysts*, 2010.
- [39] P. Nothnagel, K.-H. Müller, D. Eckert, and A. Handstein, “The influence of particle size on the coercivity of sintered NdFeB magnets,” *J. Magn. Magn. Mater.*, vol. 101, no. 1–3, pp. 379–381, 1991.
- [40] T. A. Lipo, “Synchronous reluctance machines—a viable alternative for ac drives?,” *Electr. Mach. Power Syst.*, vol. 19, no. 6, pp. 659–671, 1991.
- [41] A. Vagati, A. Canova, M. Chiampi, M. Pastorelli, and M. Repetto, “Design refinement of synchronous reluctance motors through finite-element analysis,” *IEEE Trans. Ind. Appl.*, vol. 36, no. 4, pp. 1094–1102, 2000, doi: 10.1109/28.855965.
- [42] D. A. Staton, T. J. E. Miller, and S. E. Wood, “Maximising the saliency ratio of the synchronous reluctance motor,” *IEE Proc. B Electr. Power Appl.*, vol. 140, no. 4, p. 249, 1993, doi: 10.1049/ip-b.1993.0031.
- [43] Y. Bao *et al.*, “A Novel Concept of Ribless Synchronous Reluctance Motor for Enhanced Torque Capability,” *IEEE Trans. Ind. Electron.*, vol. 67, no. 4, pp. 2553–2563, 2020, doi: 10.1109/TIE.2019.2914616.
- [44] ABB, “Synchronous reluctance motor-drive package for machine builders: High performance for ultimate machine design,” 2014.
- [45] M. J. Kamper, “Reluctance Synchronous Machine Drives – a Viable Alternative ?,” *IEEE Jt. IAS/PELS/IES Chapter Meet. Graz*, no. July, 2013.
- [46] H. Murakami, Y. Honda, H. Kiriya, S. Morimoto, and Y. Takeda, “The performance comparison of SPMSM, IPMSM and SynRM in use as air-conditioning compressor,” in *Conference Record of the 1999 IEEE Industry Applications Conference. Thirty-Forth IAS Annual Meeting (Cat. No.99CH36370)*, vol. 2, pp. 840–845, doi: 10.1109/IAS.1999.801607.
- [47] M. D. Nardo, G. L. Calzo, M. Galea, and C. Gerada, “Design Optimization of a High-Speed Synchronous Reluctance Machine,” *IEEE Trans. Ind. Appl.*, vol. 54, no. 1, pp. 233–243, 2018, doi: 10.1109/TIA.2017.2758759.
- [48] I. Boldea and S. Nasar, *The Induction machines design handbook*. 2009.
- [49] I. Boldea, *Reluctance synchronous machines and drives*. Clarendon Press, 1996.

- [50] I. Boldea, Z. X. Fu, and S. A. Nasar, "Performance evaluation of axially-laminated anisotropic (ALA) rotor reluctance synchronous motors," in *Conference Record of the 1992 IEEE Industry Applications Society Annual Meeting*, pp. 212–218, doi: 10.1109/IAS.1992.244292.
- [51] N. Bianchi, *Electrical Machine Analysis Using Finite Elements*. .
- [52] N. Bianchi, "Synchronous reluctance and interior permanent magnet motors," *Electr. Mach. Des. Control Diagnosis (WEMDCD)*, 2013 *IEEE Work.*, vol. 3, pp. 75–84, 2013, doi: 10.1109/WEMDCD.2013.6525167.
- [53] M. Degano, H. Mahmoud, N. Bianchi, and C. Gerada, "Synchronous reluctance machine analytical model optimization and validation through finite element analysis," *2016 XXII Int. Conf. Electr. Mach.*, pp. 585–591, 2016, doi: 10.1109/ICELMACH.2016.7732585.
- [54] J. K. Kostko, "Polyphase reaction synchronous motors," *J. Am. Inst. Electr. Eng.*, vol. 42, no. 11, pp. 1162–1168, 1923.
- [55] T. A. Lipo, T. J. E. Miller, A. Vagati, I. Boldea, L. Malesani, and T. Fukao, "Synchronous reluctance drives," in *Conf. Rec. IEEE IAS Annu. Meeting*, 1994, vol. 10.
- [56] E. Armando, P. Guglielmi, G. Pellegrino, M. Pastorelli, and A. Vagati, "Accurate modeling and performance analysis of IPM-PMASR motors," *IEEE Trans. Ind. Appl.*, vol. 45, no. 1, pp. 123–130, 2009.
- [57] M. Gamba, G. Pellegrino, and F. Cupertino, "Optimal number of rotor parameters for the automatic design of Synchronous Reluctance machines," *Proc. - 2014 Int. Conf. Electr. Mach. IECM 2014*, pp. 1334–1340, 2014, doi: 10.1109/ICELMACH.2014.6960355.
- [58] R. R. Moghaddam, F. Magnussen, and C. Sadarangani, "Theoretical and experimental reevaluation of synchronous reluctance machine," *IEEE Trans. Ind. Electron.*, vol. 57, no. 1, pp. 6–13, 2009.
- [59] G. Pellegrino, A. Vagati, P. Guglielmi, and B. Boazzo, "Performance comparison between surface-mounted and interior PM motor drives for electric vehicle application," *IEEE Trans. Ind. Electron.*, vol. 59, no. 2, pp. 803–811, 2011.
- [60] T. J. E. Miller, A. Hutton, C. Cossar, and D. A. Staton, "Design of a synchronous reluctance motor drive," *IEEE Trans. Ind. Appl.*, vol. 27, no. 4, pp. 741–749, 1991.
- [61] M. Degano, E. Carraro, and N. Bianchi, "Selection criteria and robust

- optimization of a traction PM-assisted synchronous reluctance motor," *IEEE Trans. Ind. Appl.*, vol. 51, no. 6, pp. 4383–4391, 2015.
- [62] P. Guglielmi, M. Pastorelli, and A. Vagati, "Impact of cross-saturation in sensorless control of transverse-laminated synchronous reluctance motors," *IEEE Trans. Ind. Electron.*, vol. 53, no. 2, pp. 429–439, 2006.
- [63] M. J. Kamper, F. S. der Merwe, and S. Williamson, "Direct finite element design optimisation of the cageless reluctance synchronous machine," *IEEE Trans. Energy Convers.*, vol. 11, no. 3, pp. 547–555, 1996.
- [64] E. C. F. Lovelace, "Optimization of a magnetically saturable interior permanent-magnet synchronous machine drive," Massachusetts Institute of Technology, 2000.
- [65] S. Talebi, P. Niazi, and H. A. Toliyat, "Design of permanent magnet-assisted synchronous reluctance motors made easy," in *2007 IEEE Industry Applications Annual Meeting*, 2007, pp. 2242–2248.
- [66] A. Vagati, G. Franceschini, I. Marongiu, and G. P. Troglia, "Design criteria of high performance synchronous reluctance motors," *Conf. Rec. 1992 IEEE Ind. Appl. Soc. Annu. Meet.*, pp. 66–73, 1992, doi: 10.1109/IAS.1992.244463.
- [67] R. R. Moghaddam and F. Gyllensten, "Novel high-performance SynRM design method: An easy approach for a complicated rotor topology," *IEEE Trans. Ind. Electron.*, vol. 61, no. 9, pp. 5058–5065, 2014, doi: 10.1109/TIE.2013.2271601.
- [68] M. J. Kamper and A. F. Volsdhenk, "Effect of rotor dimensions and cross magnetisation on L_d and L_q inductances of reluctance synchronous machine with cageless flux barrier rotor," *IEE Proceedings-Electric Power Appl.*, vol. 141, no. 4, pp. 213–220, 1994.
- [69] F. Cupertino, G. M. Pellegrino, E. Armando, and C. Gerada, "A SyR and IPM machine design methodology assisted by optimization algorithms," in *2012 IEEE Energy Conversion Congress and Exposition (ECCE)*, 2012, pp. 3686–3691.
- [70] H. Mahmoud, M. Degano, G. Bacco, N. Bianchi, and C. Gerada, "Synchronous Reluctance Motor Iron Losses: Analytical Model and Optimization," *2018 IEEE Energy Convers. Congr. Expo. ECCE 2018*, pp. 1640–1647, 2018, doi: 10.1109/ECCE.2018.8558292.
- [71] G. Pellegrino, F. Cupertino, and C. Gerada, "Automatic Design of Synchronous Reluctance Motors Focusing on Barrier Shape Optimization," *IEEE Trans. Ind. Appl.*, vol. 51, no. 2, pp. 1465–1474, 2015, doi: 10.1109/TIA.2014.2345953.

- [72] S. J. Chapman, *Electric machinery fundamentals*. McGraw-Hill, 2012.
- [73] Z. Zhong, S. Jiang, and G. Zhang, "Magnetic Equivalent Circuit Model of Interior Permanent-Magnet Synchronous Machine Considering Magnetic Saturation," *KINTEX Conf. Korea*, pp. 1–10, 2015.
- [74] J.-C. Urresty, J.-R. Riba, M. Delgado, and L. Romeral, "Detection of demagnetization faults in surface-mounted permanent magnet synchronous motors by means of the zero-sequence voltage component," *IEEE Trans. Energy Convers.*, vol. 27, no. 1, pp. 42–51, 2012.
- [75] B. Z. Q. Zhu and D. Howe, "Electrical Machines and Drives for Electric , Hybrid , and Fuel Cell Vehicles," vol. 95, no. 4, 2007.
- [76] T. M. Jahns, "Flux-weakening regime operation of an interior permanent-magnet synchronous motor drive," *IEEE Trans. Ind. Appl.*, no. 4, pp. 681–689, 1987.
- [77] T. M. Jahns, "Torque production in permanent-magnet synchronous motor drives with rectangular current excitation," *IEEE Trans. Ind. Appl.*, no. 4, pp. 803–813, 1984.
- [78] M. Barcaro, N. Bianchi, and F. Magnussen, "Permanent-magnet optimization in permanent-magnet-assisted synchronous reluctance motor for a wide constant-power speed range," *IEEE Trans. Ind. Electron.*, vol. 59, no. 6, pp. 2495–2502, 2011.
- [79] G. Pellegrino and F. Cupertino, "IPM motor rotor design by means of FEA-based multi-objective optimization," in *2010 IEEE International Symposium on Industrial Electronics*, 2010, pp. 1340–1346.
- [80] B. Stumberger, G. Stumberger, D. Dolinar, A. Hamler, and M. Trlep, "Evaluation of Saturation and Cross-Magnetization Effects in Interior Permanent-Magnet," *Ind. Appl. IEEE Trans.*, vol. 39, no. 5, pp. 1264–1271, 2003.
- [81] P. Niazi, H. A. Toliyat, and A. Goodarzi, "Robust maximum torque per ampere (MTPA) control of PM-assisted SynRM for traction applications," *IEEE Trans. Veh. Technol.*, vol. 56, no. 4, pp. 1538–1545, 2007.
- [82] S. Kim, Y.-D. Yoon, S.-K. Sul, and K. Ide, "Maximum torque per ampere (MTPA) control of an IPM machine based on signal injection considering inductance saturation," *IEEE Trans. Power Electron.*, vol. 28, no. 1, pp. 488–497, 2012.
- [83] M. Preindl and S. Bolognani, "Model predictive direct torque control with

- finite control set for PMSM drive systems, Part 1: Maximum torque per ampere operation," *IEEE Trans. Ind. Informatics*, vol. 9, no. 4, pp. 1912–1921, 2013.
- [84] J. Pyrhonen, T. Jokinen, V. Hrabovcova, and H. Niemela, *Design of Rotating Electrical Machines*. 2008.
- [85] S. Huang, J. Luo, F. Leonardi, and T. A. Lipo, "A general approach to sizing and power density equations for comparison of electrical machines," *IEEE Trans. Ind. Appl.*, vol. 34, no. 1, pp. 92–97, 1998.
- [86] G. R. Slemon, "On the Design of High-Performance Surface-Mounted PM Motors," *IEEE Trans. Ind. Appl.*, vol. 30, no. 1, pp. 134–140, 1993, doi: 10.1109/28.273631.
- [87] W. Soong, "Sizing of electrical machines," *Power Eng. Brief. Notes*, vol. 9, no. 2, pp. 17–18, 2008, [Online]. Available: http://www.eleceng.adelaide.edu.au/research/power/pebn/pebn009_sizing_of_electrical_machines.pdf.
- [88] M. Galea, C. Gerada, T. Raminosa, and P. Wheeler, "A Thermal Improvement Technique for the Phase Windings of Electrical Machines," vol. 48, no. 1, pp. 79–87, 2012.
- [89] C. Sciascera, P. Giangrande, L. Papini, C. Gerada, and M. Galea, "Analytical thermal model for fast stator winding temperature prediction," *IEEE Trans. Ind. Electron.*, vol. 64, no. 8, pp. 6116–6126, 2017.
- [90] L. X. A. Al-Timimy, P. Giangrande, M. Degano, Z. Xu, M. Galea, C. Gerada, G. Lo Calzo, H. Zhang, "Design and Losses Analysis of a High-Power Density Machine for Flooded Pump Applications," *Ind. Appl. IEEE Trans.*, vol. 54, pp. 3260–3270, 2018.
- [91] S. Nuzzo, M. Degano, M. Galea, C. Gerada, D. Gerada, and N. Brown, "Improved Damper Cage Design for Salient-Pole Synchronous Generators," *IEEE Trans. Ind. Electron.*, vol. 64, no. 3, pp. 1958–1970, 2017, doi: 10.1109/TIE.2016.2619321.
- [92] P. Ponomarev, Y. Alexandrova, I. Petrov, P. Lindh, E. Lomonova, and J. Pyrhonen, "Inductance calculation of tooth-coil permanent-magnet synchronous machines," *IEEE Trans. Ind. Electron.*, vol. 61, no. 11, pp. 5966–5973, 2014, doi: 10.1109/TIE.2014.2304933.
- [93] S. Taghavi, S. Member, and P. Pillay, "A Core Analysis of the Synchronous Reluctance Motor for Automotive Applications," vol. 2, no. 2, pp. 961–967, 2014.

- [94] G. De Recherche and U. H. Poincaré, "Comparison Between Finite-Element Analysis and Winding Function Theory for Inductances and Torque Calculation of a Synchronous Reluctance Machine," vol. 43, no. 8, pp. 3406–3410, 2007.
- [95] B. Gaussens, E. Hoang, O. De La Barrière, J. Saint-Michel, M. Lecrivain, and M. Gabsi, "Analytical approach for air-gap modeling of field-excited flux-switching machine: No-load operation," *IEEE Trans. Magn.*, vol. 48, no. 9, pp. 2505–2517, 2012, doi: 10.1109/TMAG.2012.2196706.
- [96] N. Bianchi, M. Degano, and E. Fornasiero, "Sensitivity analysis of torque ripple reduction of synchronous reluctance and interior PM motors," *IEEE Trans. Ind. Appl.*, vol. 51, no. 1, pp. 187–195, 2014.
- [97] K. Shima, K. Ide, M. Takahashi, and S. Member, "Steady-State Magnetic Circuit Analysis of Salient-Pole Synchronous Machines," *ENERGY CONVERSION*, vol. 18, no. 2, pp. 213–218, 2003.
- [98] G. S. Hall, "Homothetic transformations with fixed points in spacetime," *Gen. Relativ. Gravit.*, vol. 20, no. 7, pp. 671–681, 1988.
- [99] A. Tuller, *A modern introduction to geometries*. Van Nostrand, 1967.
- [100] A. Tessarolo *et al.*, "A heuristic homotetic approach to the dimensioning of induction motors from specification data," in *2014 AEIT Annual Conference-From Research to Industry: The Need for a More Effective Technology Transfer (AEIT)*, 2014, pp. 1–5.
- [101] A. Tessarolo, M. De Martin, D. Diffen, M. Branz, and M. Bailoni, "Practical assessment of homothetic dimensioning criteria for induction motors," *7th IET Int. Conf. Power Electron. Mach. Drives, PEMD 2014*, pp. 1–6, 2014, doi: 10.1049/cp.2014.0512.
- [102] R. R. Moghaddam and F. Gyllensten, "Novel High Performance SynRM Design Method an Easy Approach for a Complicated Rotor Topology.pdf," no. c, pp. 1–8, 2013.
- [103] M. Murataliyev, M. Degano, and M. Galea, "A Novel Sizing Approach for Synchronous Reluctance Machines," *IEEE Trans. Ind. Electron.*, vol. 0046, no. 2, 2020, doi: 10.1109/TIE.2020.2975461.
- [104] D. A. Freedman, *Statistical models: theory and practice*. cambridge university press, 2009.
- [105] C. Sciascera, P. Giangrande, L. Papini, C. Gerada, and M. Galea, "Analytical Thermal Model for Fast Stator Winding Temperature Prediction," vol. 0046,

- no. LCC, 2017, doi: 10.1109/TIE.2017.2682010.
- [106] R. J. Freund, W. J. Wilson, and P. Sa, *Regression analysis*. Elsevier, 2006.
- [107] P. Mattavelli, L. Tubiana, and M. Zigliotto, "Torque-ripple reduction in PM synchronous motor drives using repetitive current control," *IEEE Trans. Power Electron.*, vol. 20, no. 6, pp. 1423–1431, 2005, doi: 10.1109/TPEL.2005.857559.
- [108] B. N. Nakao and K. Akatsu, "Suppressing Pulsating Torques," no. September, pp. 33–44, 2014.
- [109] A. K. M. Arafat and S. Choi, "Active Current Harmonic Suppression for Torque Ripple Minimization at Open-Phase Faults in a Five-Phase PMA-SynRM," *IEEE Trans. Ind. Electron.*, vol. 66, no. 2, pp. 922–931, 2019, doi: 10.1109/TIE.2018.2829685.
- [110] S. Han, T. M. Jahns, W. L. Soong, and K. G. Mustafa, "Torque Ripple Reduction in Interior Permanent Magnet Synchronous Machines Using Stators With Odd Number of Slots Per Pole Pair," vol. 25, no. 1, pp. 118–127, 2010.
- [111] N. Bianchi, S. Bolognani, D. Bon, and M. D. Pré, "Rotor flux-barrier design for torque ripple reduction in synchronous reluctance and PM-assisted synchronous reluctance motors," *IEEE Trans. Ind. Appl.*, vol. 45, no. 3, pp. 921–928, 2009, doi: 10.1109/TIA.2009.2018960.
- [112] M. Sanada, K. Hiramoto, S. Morimoto, and Y. Takeda, "Torque Ripple Improvement for Synchronous Reluctance Motor using Asymmetric Flux Barrier Arrangement," pp. 250–255, 2003.
- [113] T. M. Jahns and W. L. Soong, "Pulsating Torque Minimization Techniques for Permanent Magnet AC Motor Drives-A Review," vol. 43, no. 2, 1996.
- [114] M. Degano, E. Carraro, and N. Bianchi, "Selection Criteria and Robust Optimization of a Traction PM Assisted Synchronous Reluctance Motor," vol. 9994, no. c, 2015, doi: 10.1109/TIA.2015.2443091.
- [115] N. Bianchi, M. Degano, and E. Fornasiero, "Sensitivity Analysis of Torque Ripple Reduction of Synchronous Reluctance and Interior PM Motors," no. x, pp. 1842–1849, 2013.
- [116] M. Murataliyev *et al.*, "A Homothetic Scaling Criteria for Synchronous Reluctance Machines Design," *IEEE Trans. Energy Convers.*, p. 1, 2020.
- [117] C. Babetto, G. Bacco, and N. Bianchi, "Synchronous Reluctance Machine Optimization for High Speed Applications," *IEEE Trans. Energy Convers.*,

- vol. 8969, no. c, pp. 1–8, 2018, doi: 10.1109/TEC.2018.2800536.
- [118] M. Di Nardo, M. Galea and C. Gerada, “Multi-physics Optimization Strategies for High Speed Synchronous Reluctance Machines,” no. Im, pp. 2813–2820, 2015.
- [119] N. Bianchi, E. Fornasiero, M. Ferrari, and M. Castiello, “Experimental Comparison of PM-Assisted Synchronous Reluctance Motors,” vol. 52, no. 1, pp. 163–171, 2016.
- [120] M. Barcaro, N. Bianchi, and F. Magnussen, “Remarks on torque estimation accuracy in fractional-slot permanent-magnet motors,” *IEEE Trans. Ind. Electron.*, vol. 59, no. 6, pp. 2565–2572, 2011.